



Review

Morphology engineering of photoelectrodes for efficient photoelectrochemical water splitting

Edmund Samuel^{a,1}, Bhavana Joshi^{b,1}, Min-Woo Kim^a, Mark T. Swihart^{c,*}, Sam S. Yoon^{a,*}^a School of Mechanical Engineering, Korea University, Seoul, 02841, Republic of Korea^b Department of Physics, NES Science College, Swami Ramanand Teerth Marathwada University, Latur Road, Nanded, Maharashtra, 431606, India^c Department of Chemical & Biological Engineering and RENEW Institute, University at Buffalo, The State University of New York, Buffalo, NY, 14260-4200, USA

ARTICLE INFO

Keywords

Water splitting
 Nanostructures
 Nanocomposites
 Z-scheme
 Co-catalyst
 Passivation layers

ABSTRACT

Photoelectrochemical solar water splitting is a promising method for harvesting clean and sustainable solar energy by the carbon emission-free production of energy-rich hydrogen. Various strategies such as nanostructuring, composite engineering, and multilayer formation have been adopted for energy-efficient photoelectrode preparation, with the ultimate goal of enhancing the efficiency of energy harvesting and storage via the photoelectrochemical water-splitting reaction. This review summarizes recent advances in the abovementioned strategies for fabricating water-splitting photoelectrodes and outlines relationships between the structure, composition, and electrochemical properties of such photoelectrodes. Our aim is to help readers become cognizant of recent developments in the field, providing them with a distinct perspective for carrying innovative work on photoelectrode preparation.

1. Introduction

Hydrogen is one of the cleanest and most sustainable energy carriers, producing zero carbon emissions upon combustion or oxidation in a fuel cell. Such a source of chemically-stored energy can play a central role in meeting massive power requirements in the future. Hydrogen can be obtained cleanly via photoelectrochemical (PEC) water splitting, but the overall efficiency of this process remains relatively low. Engineering metal-oxide heterostructures and composites thereof as photoelectrodes is essential to achieve water-splitting using abundantly available solar energy. Research performed in the last two decades has focused on innovative photoelectrode design for PEC devices to generate hydrogen [1–4]. A key advantage of hydrogen as an energy carrier is its high calorific value of 150 kJ/g [5,6]. The U.S. Department of Energy has projected the cost of producing hydrogen gas through PEC water splitting must reach approximately \$2.10 per kg (in 2007 dollars) to become economically competitive, and has laid out multiple scenarios and pathways to reach this target [7].

Solar water splitting, the dissociation of water molecules into O₂ and H₂ using energy from sunlight, is analogous to the natural photosynthesis process in plants. In PEC water splitting, light incident on photoelectrodes submerged in an electrolyte drives the oxygen evolution reaction (OER) at the photoanode and the hydrogen evolution reaction (HER) at photocathode. Both academic and industrial re-

search has focused on the development of efficient PEC water-splitting devices to generate hydrogen. Thermochemical and electrochemical approaches are also used for obtaining hydrogen via water splitting; however, PEC solar water splitting is regarded by many as an ideal low-cost, environmentally friendly, and renewable method. The PEC water splitting process, hydrogen fuel generation, use in a fuel cell, and regeneration of water are schematically presented in Fig. 1. The PEC water-splitting concept was proposed by Fujishima and Honda in 1972, using a TiO₂ photoanode. Since then, numerous semiconductors have been employed for the direct harvesting of solar energy for producing clean and storable hydrogen by PEC water splitting [8–15].

To date, several reviews have explained the mechanisms [17], materials [18], and heterostructures [19] of photoelectrodes. Hence, in this review, we focus on research from 2016 onwards that has provided insights into how nanostructures, multilayers, and nanocomposites of various photoelectrode materials can be used for water-splitting applications.

2. Water-splitting working principle

Water splitting is an energetically uphill (thermodynamically unfavorable) reaction. Converting liquid water to hydrogen and oxygen gases at 298 K and 1 bar increases the Gibbs energy (ΔG°) by 237 kJ/mol. The electrochemical water splitting reaction requires a minimum applied voltage of ~ 1.23 V at 298 K and neutral pH. Solar energy

* Corresponding author.

** Corresponding author.

E-mail addresses: swihart@buffalo.edu (M.T. Swihart); skyoona@korea.ac.kr (S.S. Yoon)¹ These authors have equally contributed.

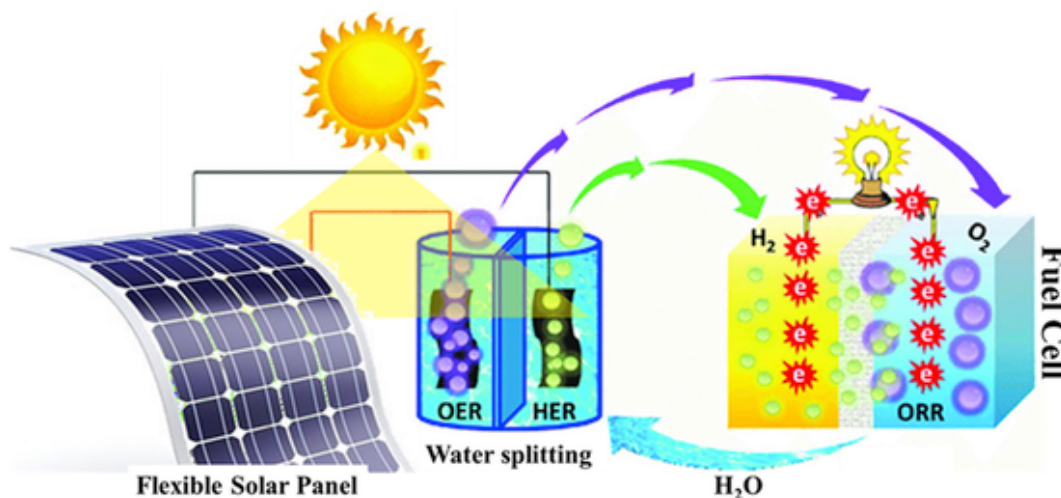


Fig. 1. Solar light harvesting for PEC energy harvesting, hydrogen generation, and hydrogen utilization in fuel cells. Adapted with permission from Ref. [16].

with a wavelength of 1000 nm is equivalent to this minimum required applied voltage [20–22]. Of course, driving the reaction at a finite rate requires a higher voltage, which depends on the catalytic properties of the photoelectrode. In simple words, the working principle of water-splitting involves absorbing solar energy illumination to drive water electrolysis, as shown in Fig. 1. A semiconducting electrode with the appropriate bandgap matching the solar spectrum generates electron-hole pairs under photon illumination. With an *n*-type semiconductor as the working electrode, holes at the semiconductor surface react with water molecules (or OH⁻) to generate O₂, while electrons are transported to the counter electrode where they reduce water (or H⁺) to produce H₂. Conversely, a *p*-type semiconductor as the working electrode produces H₂, with O₂ generated at the counter electrode. Hence, a *p*-type semiconductor yields a cathodic photocurrent by the transfer of electrons to the electrolyte; an *n*-type semiconductor produces an anodic photocurrent by transfer of holes to the electrolyte [19]. In typical experiments, a setup similar to that shown in Fig. 1 is used along with a reference electrode to study the half-reactions in the PEC cell. These half-reactions are the HER and OER, can be described as follows, for acidic electrolyte:

- 1) Light absorption by photoelectrode (PE):
 $PE + h\nu (> \text{bandgap of PE}) \rightarrow e_{CB}^- + h_{VB}^+$

- 2) Photoanode (OER): $H_2O + 2h_{VB}^+ \rightarrow \frac{1}{2}O_2 \uparrow + 2H^+$ $E_{oxidation}^o = 1.23 V$
- 3) Photocathode (HER): $2H^+ + 2e^- \rightarrow H_2 \uparrow$ $E_{reduction}^o = 0.0 V$
- 4) Overall: $H_2O + h\nu \rightarrow H_2 \uparrow + \frac{1}{2}O_2 \uparrow$

In real systems, the energy required for PEC water splitting can reach 2 V because of the overpotential required for each half reaction, resistance in the electrodes, losses by electron-hole recombination, potential drops at contacts, and other non-idealities. Thus, an external bias is often applied to overcome these losses and achieve the energy required for water splitting [20,23].

The overall efficiency of water splitting depends on the band structure of the photoelectrode, as seen in the schematic of an *n*-type electrode shown in Fig. 2. Before contact of the *n*-type working electrode (anode) and electrolyte, the conduction and valence bands in the electrode are flat, as shown in Fig. 2a. Under dark condition (Fig. 2b), with the electrode and electrolyte in contact, charge transfer occurs between the electrode and electrolyte until the Fermi energy of the electrode and the redox potential of the electrolyte are aligned across the interface. This charge transfer induces band bending in the electrode. Under illumination, electron-hole pairs are formed, yielding a photovoltage. The electron-hole pair formation continues until the bent bands are flattened. Once the bands are flat, no change in photovolt-

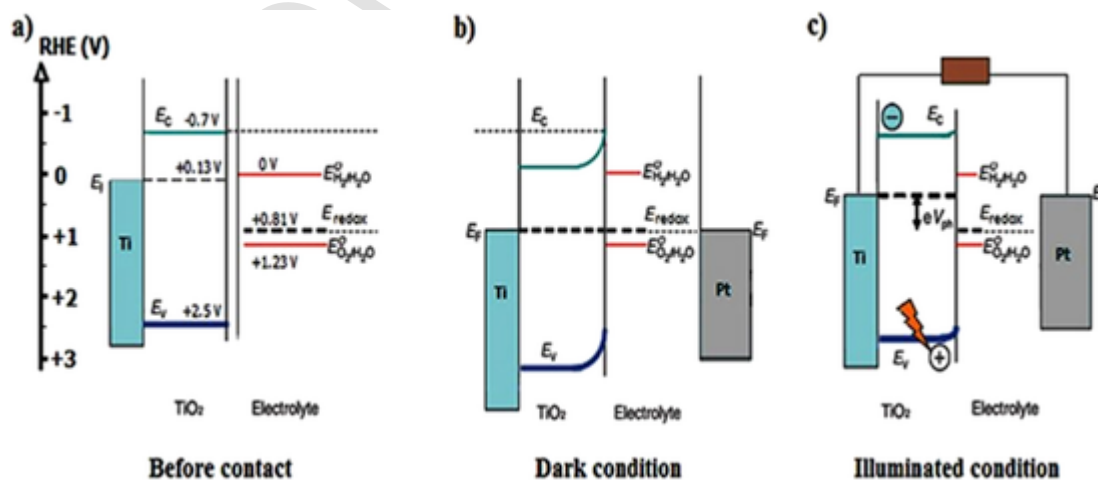


Fig. 2. Bandgap tailoring and band bending for Fermi-level (E_F) energy alignment. RHE: Reversible hydrogen electrode. E_C : Conduction band energy. E_V : Valence band energy. Reprinted with permission from Ref. [24].

age occurs even under intense light illumination. The photovoltage separates the Fermi level and redox potential, as presented in Fig. 2c. Further, when an external bias is applied, the Fermi energy level of the counter electrode (cathode) is elevated above the redox potential, which causes electron transfer to the cathode; these electrons react with H^+ ions in the electrolyte to generate hydrogen. In the PEC reaction, electrons are critical for the production of molecular hydrogen on either the counter electrode (Pt) with an *n*-type photoanode or at the working electrode with a *p*-type photocathode [19].

In short, a typical PEC process involves the following four essential steps: (i) photon absorption; (ii) creation and separation of electron-hole pairs under illumination; (iii) transport of charge carriers out of the photoelectrode; and (iv) surface chemical reactions. The created electron-hole pairs can recombine in the bulk or on the surface in steps (iii) and (iv). Thus, the rate of electron-hole pair generation and separation must be matched to the water oxidation kinetics to achieve an efficient water-splitting reaction.

Numerous tactics have been employed to enhance the performance of PEC electrodes, such as doping, nanostructuring [18], heterojunction formation [19], and nanocomposite preparation [25]. Despite various developments in PEC and photoelectrodes, no current materials achieve and sustain 10% efficiency for solar-to-hydrogen (STH) energy conversion, which is often regarded as the minimum viable efficiency. The high kinetic overpotentials associated with the OER, in particular, lead to losses in the overall efficiency of water splitting [26–28]. Thus, this paper summarizes and discusses recent advances on topics such as nanostructures, multilayered structures, and nanocomposites to pro-

vide understanding and allow effective use for enhancing the PEC performance.

3. Morphology-engineered nanostructures

The syntheses and morphology engineering of oxides, selenides, and other semiconductors are significant because they offer rich active sites for PEC reactions [29–33]. Various engineered morphologies and their growth mechanisms have been presented in numerous reports. However, the vast available research on nanostructures of varying complexities requires correlated analysis to reach generalized conclusions and provide insights that can advance research toward practical implementation. Key properties that can be tuned through morphology design and engineering include specific surface area, electrical conductivity, crystallinity, optical absorbance and scattering, and effective bandgap. These should be simultaneously optimized to achieve stable and enhanced photocurrent generation [31–33]. Furthermore, morphology engineering of photoelectrodes can enhance the PEC process by providing improved charge separation and shorter paths for charge transport, thus promoting the HER and OER. Nanostructures such as nanotrees, nanosheets, nanoflowers, nanopillars, nanorods (NR), and nanowires (NWs) have been widely reported as photoelectrode materials for water splitting [34–36]. Some scanning electron microscopy (SEM) images of these morphologies, as well as data on their photocurrent responses and mechanisms, are presented in Fig. 3 to illustrate the role of morphology engineering for enhanced solar water splitting [37–43].

Addressing the problems of quantum efficiency, slow kinetics of reactions of holes, slow charge transfer, and charge separation for en-

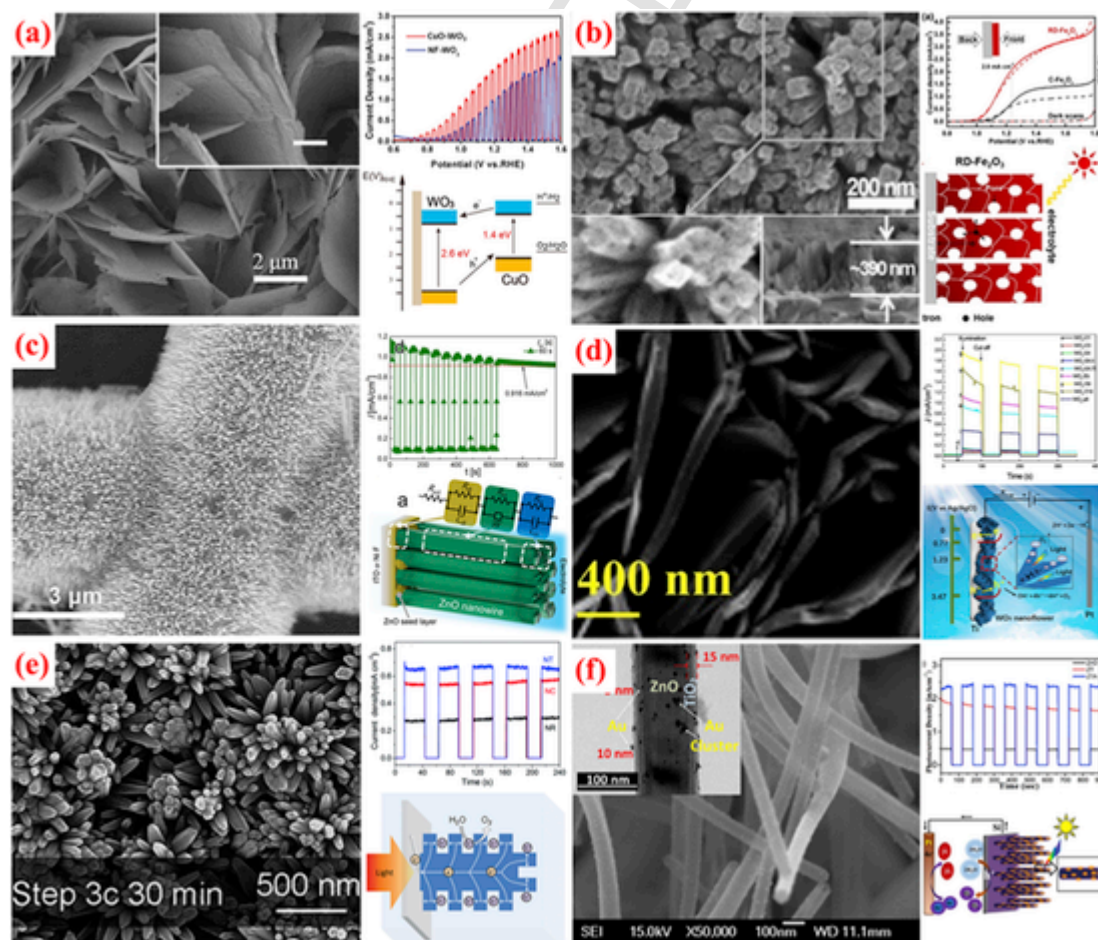


Fig. 3. SEM images, photocurrent responses, and mechanisms of morphology-engineered nanostructured semiconductor composites: (a) ZnO nanotree [44], (b) Fe_2O_3 porous nanopillars [45], (c) ZnO NWs [46], (d) WO_3 nanoflowers [47], (e) WO_3 nanoflakes [48], and (f) ZnO/ TiO_2 core-shell [49].

hancing photocurrent is challenging. Charge separation in nanostructures such as NWs, nanoflowers, and nanoflakes can be significantly improved because charge transport distances to the electrode-electrolyte interface can be reduced while maintaining a long optical pathlength for high absorption. Photoexcited electron-hole pair generation is also increased by internal scattering, the increases the effective optical pathlength, while reaction rates are enhanced by the larger interfacial area compared to a flat film. The larger open surface area (see Fig. 3a-f) significantly improves the OER in nanostructured materials such as nanotrees and ultrathin nanoflakes compared to that in their bulk or dense film counterparts. Further advantages of nanostructured materials such as nanoflakes can be introduced by manipulating oxygen vacancies to increase the number of active PEC sites, decrease the effective bandgap energy, and improve solar light absorption [34–36].

Nanoflakes of oxides such as WO_3 grown over transparent conducting oxides are advantageous because the PEC reaction mainly occurs at the electrolyte-semiconductor interface. However, researchers must address the degradation of these binary oxides by photocorrosion. As reported by Ye et al. [50], the introduction of a second metallic element can be a good strategy for improving stability. Bimetallic photoelec-

trodes can also suppress undesirable reactions. In addition, the photocurrent density (PCD) achieved using CuWO_3 was $\sim 0.4 \text{ mA cm}^{-2}$, exceeding the value of 0.3 mA cm^{-2} shown by WO_3 [50] through bandgap energy tuning. From studies like these, one can infer that the morphology of nanoflakes or nanostructures can be manipulated to improve hole generation and charge separation [41–43]. The formation of heterojunctions can also enhance charge separation [50,51]. This phenomenon is well established for the CoO_x/WO_3 photoanode, where CoO_x is loaded on WO_3 nanoflakes to form a heterostructure. The presence of CoO_x on the WO_3 improves the efficiency of WO_3 by approximately a factor of 1.6. The enhanced efficiency is caused by two synergistic effects: (1) heterojunction formation and (2) the catalytic ability of CoO_x [51]. Table 1 summarizes the materials, synthesis methods, and PEC performance of various photoelectrodes. The PEC performance of some nanostructures such as the thorny devil, pillars, and nanoplates are presented in Table 2 [9,52–56].

Recently reported synthesis approaches for NWs can provide uniform and perpendicular growth to achieve structures that offer a higher number of active PEC sites per substrate area. For example, ZnO NWs reported by Jo et al. [46] and CuO NWs reported by Li et al. [57]

Table 1
Summary of electrodes using NW and nanoflake morphology, photoelectrode synthesis approach, and PEC performance for water-splitting applications.

	Photoelectrode	Method	Photocurrent Density (mA cm^{-2})	V vs. RHE [V]	Efficiency (%)	Ref.
Nanowires	3D-Branched ZnO/CdS NW	Laser interference/spin coating/hydrothermal and SILAR	3.58 at 0 $V_{\text{Ag/AgCl}}$	0.2	3.1	[29]
	ZnO NW	Spin coating	0.5 at 0.6 $V_{\text{Ag/AgCl}}$	0.8	–	[30]
	ZnO branched NWs	Direct-current glow discharge plasma	1.7 at 0.8 $V_{\text{Ag/AgCl}}$	1	0.3	[31]
	Ag/Co-doped ZnO nanowire	Polyol and RF magnetron sputtering	0.07 at 0.4 $V_{\text{Ag/AgCl}}$	0.6	0.73	[32]
	ZnO nanowire	Hydrothermal	0.6 at 0.25 V_{SCE}	0.49	6.3	[33]
	ZnO nanowire	Hydrothermal	0.9 at 1.23 V_{RHE}	1.23	0.36	[37]
	Au@CdS core-shell NPs-modified ZnO NWs	Spin coating and CBD	0.273 at 0.6 $V_{\text{Ag/AgCl}}$	0.8	–	[38]
	PtO coated ZnO nanowire	Sol-gel spin coating and hydrothermal	2.3 at 1.23 V_{RHE}	1.23	–	[39]
	Au/ZnO NW hetero-arrays	Sol-gel spin coating and Photo-reduction	0.03 at 0.2 V_{SCE}	0.44	–	[40]
	Nanoflakes	Zr doped $\beta\text{-In}_2\text{S}_3$ NF	Solvothermal	1.1 at 1.3 V_{RHE}	1.3	0.5
$\text{PrBa}_{0.5}\text{Sr}_{0.5}\text{Co}_2\text{O}_{5+\delta}$ @FeOOH NF		Electrospinning and Immersion	5.37 at 1.6 V_{RHE}	1.6	–	[36]
WO_3 NF/CuO		Solvothermal and dip coating	1.8 at 1.23 V_{RHE}	1.23	65	[48]
CuWO_4 NF		Hydrothermal, impregnation	0.4 at 1.23 V_{RHE}	1.23	13	[50]
UNiMOF NF/g-C ₃ N ₄ NF		Chemical solution and Hydrothermal	0.011×10^{-3}	–	–	[59]
CuS NF/TiO ₂		Chemical solution and Hydrothermal	0.013 at 0.6 V_{SCE}	0.84	–	[41]
Sn ₃ O ₄ NF/graphene quantum dot		Hydrothermal	0.006 at 1.23 V_{RHE}	1.23	–	[42]
WO_3 NF		Hydrothermal	1.80 at 1.23 V_{RHE}	1.23	–	[43]
Mo-doped CuWO_4 NF		Hydrothermal and drop casting	0.62 at 1.23 V_{RHE}	1.23	19	[60]
a-CoO NF		Laser Ablation	0.0016	–	0.6	[61]
$\text{WO}_3/\text{BiVO}_4$ NF	Hydrothermal	0.109 at 1.23 $V_{\text{Hg/Hg}_2\text{Cl}_2}$	–	–	[62]	

Table 2
Overview of materials and nanostructures used as photoelectrodes.

Materials	Nanostructures	Reaction solution	PCD [mA cm ⁻²]	V vs. RHE [V]	Ref.
CuO	irregular	1 M KOH	-3.1 ^a @-0.6 V	-0.4	[52]
CuO	Thorny devil	1 M KOH	-4.1 ^a @-0.6 V	-0.4	[109]
BiVO ₄	pillars	0.5 M Na ₂ SO ₄	1.3 ^a @1.2 V	1.4	[66]
WO ₃	Nanoplates	0.5 M Na ₂ SO ₄	1.0 ^b @1.6 V	1.6	[54]
WO ₃	nanofibers	0.5 M H ₂ SO ₄	2.4 ^a @1.2 V	1.4	[55]
TiO ₂	Nanotubes	1 M KOH	0.06 ^a @0.6 V	0.8	[56]
CuWO ₄	nanoflowers	0.1 M Na ₂ SO ₄	0.58b@0.8 V	0.8	[9]

PCD value at: V_{Ag/AgCl}^a, V_{RHE}^b.

were synthesized via a facile thermal treatment. To enhance the photocurrent of ZnO and reduce its photocorrosion, Jo et al. [46] designed a ZnO NW photoelectrode with a Ni nanofiber as an underlayer for rapid electron transfer. The synergy between the underlying Ni nanofiber and the ZnO NWs grown over it provided an enhanced PCD of 1.14 mA cm⁻² at 0.4 V_{Ag/AgCl}. That report demonstrated a substrate-free flexible photoelectrode that maintained ~98% stability over 1000 bending cycles. Some recently reported ZnO NWs are summarized in Table 1. The short-circuit PCD of a three-dimensional (3D) branched ZnO/CdS NW [29] electrode was much higher, reaching 3.58 mA cm⁻² at 0 V_{Ag/AgCl}, indicating that pure ZnO NWs can be improved by introducing additional photoactive materials such as CdS. The presence of CdS over ZnO NWs provides a better photocurrent response because of its photocatalytic activity under visible light [29]. In addition, even though there are advantages to the NW morphology, the presence of crystal facets is also crucial, in that the photogenerated electrons accumulate at specific facets and support efficient electron-

hole separation. In the absence of such crystal facets in the NWs, rapid recombination of electron-hole pairs occurs [58].

3.1. Nanopillars, nanorods, and nanoferns

In the past few years, inorganic nanopillars, NRs, and nanoferns with diverse morphologies have attracted considerable interest [63–67]. Nanopillars provide a structure with a shortened diffusion distance to promote charge transport to the electrolyte interface and scattering that improves light absorption. Additionally, the large surface area and low density facilitate rapid reaction and suppress recombination when used with materials of appropriate physical and compositional properties. Some recent and exceptionally well-designed nanostructure morphologies of low-cost electronically suitable BiVO₄ are shown in Fig. 4 [63–66,68].

BiVO₄ dendritic hyperbranches and other morphologies in Fig. 4 are promising for solar light harvesting, photoexcited charge carrier separation, reusability, and enhanced photoelectrode-electrolyte interfacial reactions. The nanostructuring reduces the charge transportation distance compared to that in bulk photoactive materials. BiVO₄ has a conduction band (CB) near 0 V_{RHE}, while the valence band (VB) is near 1 V_{RHE}, which aligns favorably with the water oxidation potential of 1.23 V. Liu et al. have reported a PCD of 1.67 mA cm⁻² at 1.83 V_{RHE} from porous BiVO₄ NRs obtained by multistep ion exchange using solvothermal, hydrothermal, drop casting and annealing [63].

Si is an abundant material that can achieve power conversion efficiencies exceeding 25% for photovoltaic applications. Zhou et al. [69] suggested combining earth-abundant materials like Si with GaN, Chakthranont et al. [64] paired Si NWs with BiVO₄. Chakthranont et al. reported a STH efficiency of 0.45%. The synthesis approach they followed provided significant potential to tailor the PEC cell design of individual components such as the Si NW and metal oxide dimensions [64]. They also suggested that the synthesis approach was compatible with those already used for fabricating monolithic devices in practical applications.

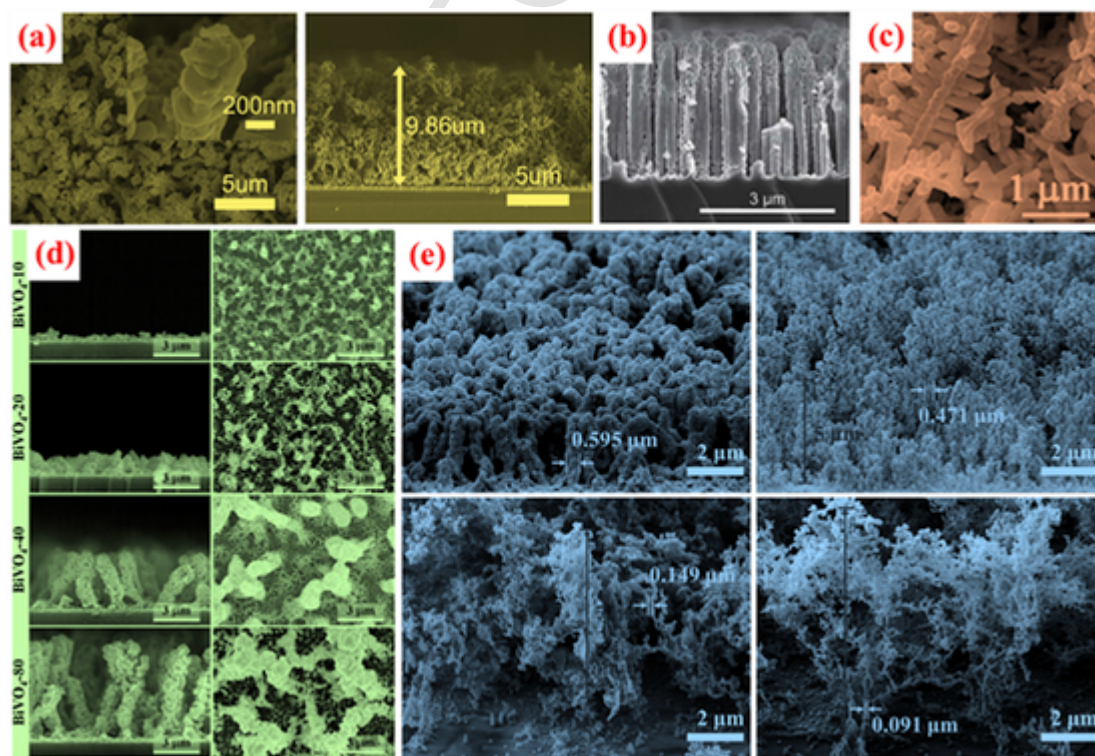


Fig. 4. SEM images of (a) top and side view of porous NR BiVO₄ [63], (b) core-shell Si/W-doped BiVO₄ [64], (c) dendritic hyperbranched BiVO₄ [65], (d) top and side view of BiVO₄ as a function of electro spray time [66], and (e) nanofern BiVO₄ [68].

Patil et al. [65] synthesized dendritic hyperbranched $\text{BiVO}_4/\text{Ag}/\text{reduced}$ graphene oxide (rGO), which delivered a PCD of 2.25 mA cm^{-2} at $1.5 V_{\text{RHE}}$ for water oxidation with the STH efficiency of 0.9%. Yoon et al. [66] optimized the electrostatic spraying time for BiVO_4 deposition and suggested nanopillars of $3 \mu\text{m}$ in height as optimal, delivering a PCD of 1.95 mA cm^{-2} at $0.7 V_{\text{Ag}/\text{AgCl}}$. The optimized BiVO_4 nanopillars were deposited for 40 min at a substrate temperature of 80°C . They concluded that the electro sprayed nanopillar structure formed by the electric drift of sub-micrometer particles from the nozzle in a direction parallel to the indium tin oxide (ITO) substrate.

SEM images of the nanofern BiVO_4 photoelectrodes show the significant impact of the precursor solution pH. In particular, with non-vacuum electrostatic spray deposition, increases in pH affect the thermodynamics and nucleation of precipitates, yielding taller and broader BiVO_4 nanoferns (see Fig. 4e). The larger fern has a larger surface area, permitting increased solar light harvesting. Furthermore, increasing the pH values of the precursor decreases the density and effective refractive index of the active photoanode material, but indicates no change in the crystallinity of the monoclinic scheelite BiVO_4 as reported by Kim et al. [68]. These nanoferns showed faster photoresponses than denser films because of the enhanced number of PEC sites per substrate area. The transformation of electro sprayed BiVO_4 nanopillars to a nanofern structure was demonstrated; the modification of morphology increased the PCD of BiVO_4 from 0.82 to 1.23 mA cm^{-2} at $1.2 V_{\text{Ag}/\text{AgCl}}$ [68]. This high nanofern PCD arose from the suppressed electron-hole recombination and provide shorter charge transfer pathway.

Thus, PCD enhancement can be achieved in many ways by controlling the synthesis conditions carefully: (i) multistep ion-exchange of porous BiVO_4 NRs produced a surface to volume ratio that favors PEC application; (ii) core-shell tandem PEC water-splitting cells using earth-abundant crystalline Si and BiVO_4 as photo-absorbers allow cost-effective

solar hydrogen production; (iii) introducing plasmonic metal nanoparticles (NPs) such as Ag and carbonaceous materials to semiconductors can induce localized surface plasmon resonance effects that enhance electron-hole pair generation; (iv) optimizing the process parameters can increase the PCD; and (v) modifying the pH of the precursor can increase the number of active sites and photoelectrode-electrolyte interfacial interactions. Such growth processes and architectures for solar water-splitting photoelectrodes are highly useful for attaining high optical-to-chemical energy conversion efficiency and photostability [63–66,68].

3.2. Surface treatments of nanostructures

A photoanode of $\text{FeOOH}/\text{NiOOH}/\text{BiVO}_4$ (Fig. 5c) shows a sub-micrometer particulate morphology. The photoanode was treated with a mild thermal process to introduce oxygen vacancies and improve the transparency. Oxygen vacancies function as charge donors, thus promoting charge separation. Wang et al. [70] reported a remarkably high PCD of 5.87 mA cm^{-2} at $1.23 V_{\text{RHE}}$ and almost 6.5% STH efficiency for unbiased water splitting with the treated composite photoanode. The dual photoelectrode delivered an incident photon-to-current conversion efficiency (IPCE) of 90% at a wavelength of 450 nm. The sample demonstrates excellent PEC performance in part because of its good electronic conductivity. The morphology is more straightforward than the nanostructures discussed in section 3.1. $\text{FeOOH}/\text{NiOOH}/\text{BiVO}_4$ includes two oxygen evolution co-catalysts that allow it to deliver a higher PCD, as well as stability up to 100 h. The presence of FeOOH and NiOOH as co-catalysts enhances the charge separation efficiency by rapidly consuming holes via reaction. The strategy of surface modification with co-catalysts provides a new route for obtaining excellent PEC performance from photoanodes. The improvement in the PCD arises from the enhanced interfacial hole extraction kinetics and the re-

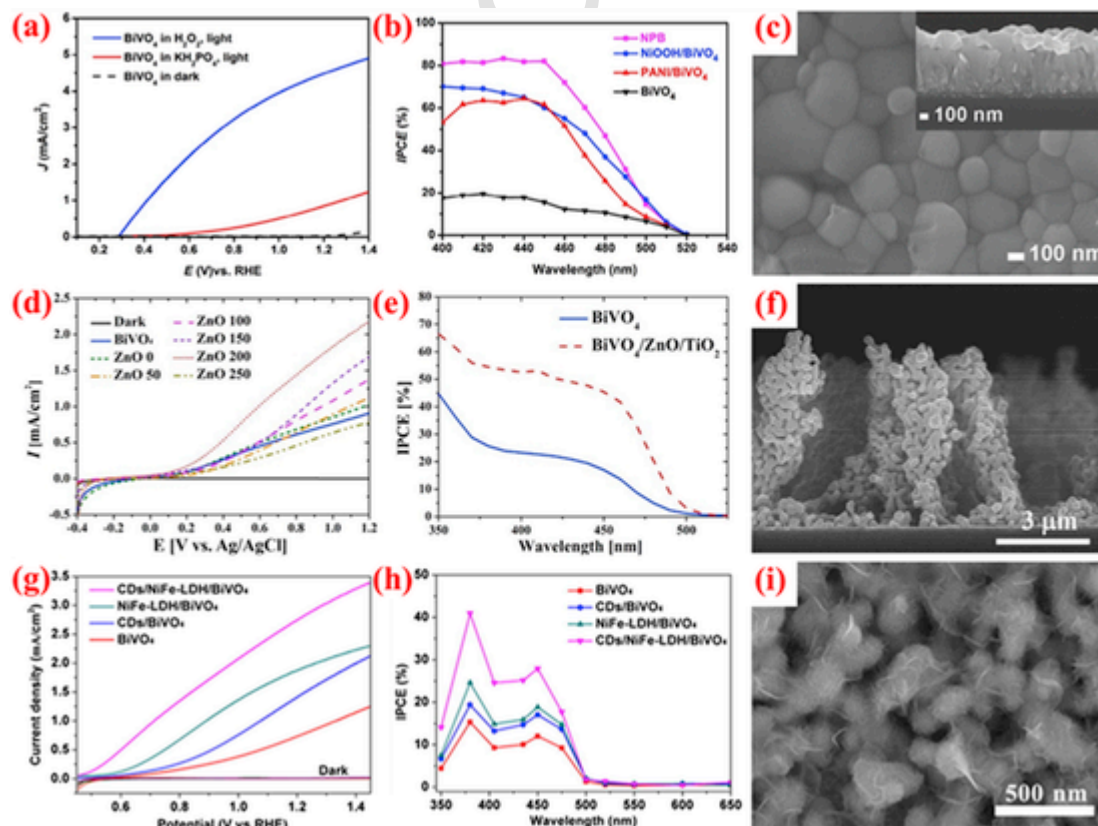


Fig. 5. PCD, incident photon-to-charge-carrier conversion efficiency (IPCE), and SEM images of (a–c) $\text{FeOOH}/\text{NiOOH}/\text{BiVO}_4$ [70], (d–f) $\text{BiVO}_4/\text{ZnO}/\text{TiO}_2$ [71], and (g–i) $\text{CDs}/\text{NiFe-LDH}/\text{BiVO}_4$ [72].

duced overpotential required for water oxidation. However, the presence of co-catalysts also has limitations, such as shielding the active material from incident light and possibly increasing charge recombination [73,74]. The electro spray deposition technique used by Kim et al. has been used for nanopillar structures of BiVO_4 - and Bi_2WO_6 -based PEC photoelectrodes [71,75]. BiVO_4 nanopillars have been passivated with two oxides (ZnO and TiO_2) to improve their PEC performance. Such passivated nanopillars of BiVO_4 reduce hole accumulation at the electrode–electrolyte interface via their multiple interface junctions and quickly transfer electrons to ITO to provide an enhanced PCD of 2.5 mA cm^{-2} at $1.2 \text{ V}_{\text{Ag}/\text{AgCl}}$. The atomic layer deposition (ALD) of ZnO and TiO_2 yields ultra-thin conformal passivation layers that en-

hance the IPCE by almost 20% at the optimal thickness compared to that of bare BiVO_4 . The high-dielectric-constant TiO_2 as a passivation layer on nanostructure-based photoelectrodes can reduce the charge density at the photoelectrode–electrolyte interface [71,76].

3.3. Nanoflowers and nanotube arrays

TiO_2 is inexpensive and easy to synthesize; it demonstrates a high photocurrent and excellent stability, as reported Dong et al. [77]. However, it has a wide bandgap and therefore only absorbs at ultraviolet wavelengths. Morphology engineering of TiO_2 (Fig. 6a and b) and creation of new oxygen vacancies reduces its bandgap energy, thus ex-

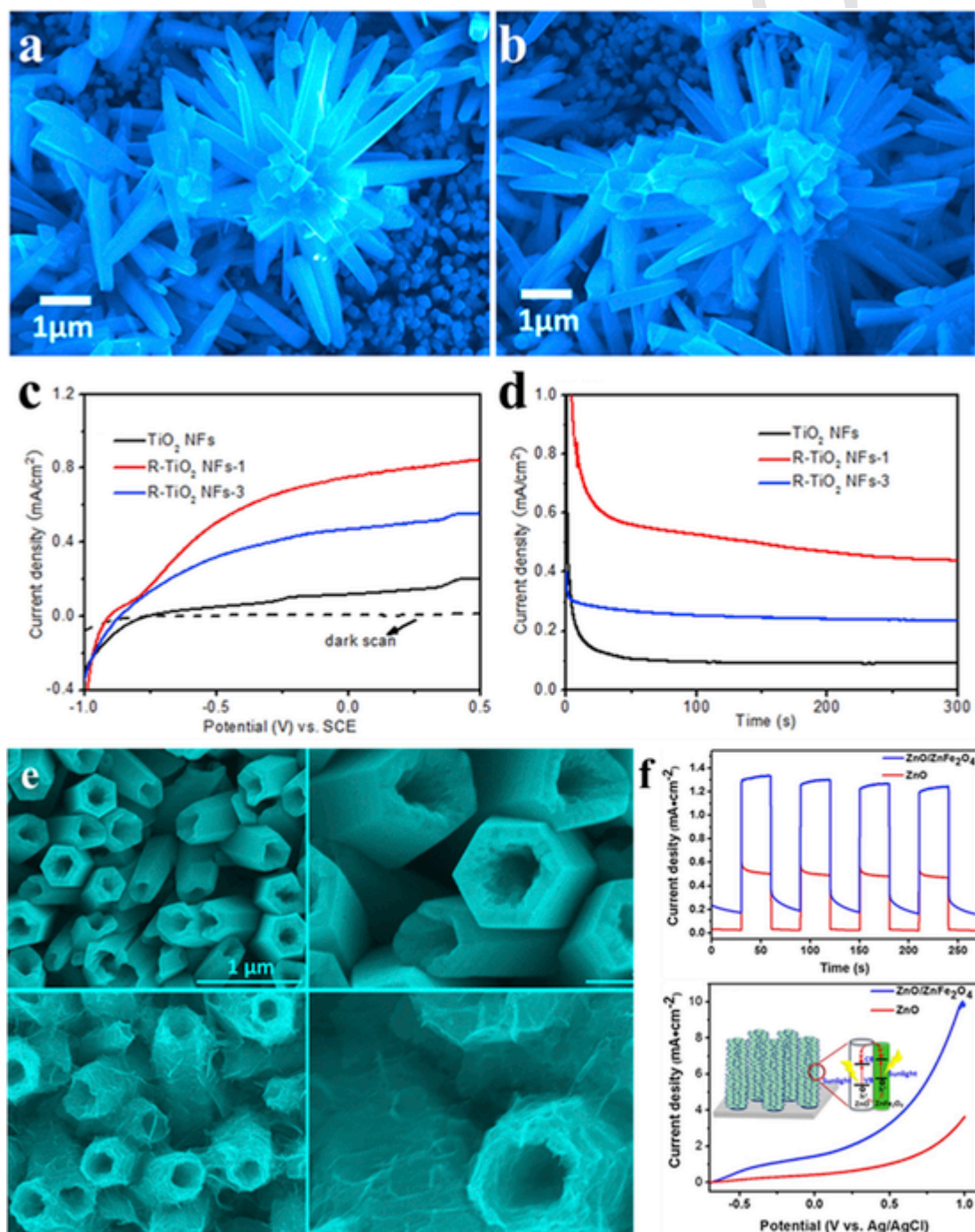


Fig. 6. SEM images of (a) TiO_2 and (b) R-TiO_2 nanoflowers. (c) Photocurrent response of photoanodes and (d) $J-t$ curves at 0 V relative to a saturated calomel electrode (SCE) [77]. (e) SEM images of pristine ZnO nanotube array and hierarchical $\text{ZnO}/\text{ZnFe}_2\text{O}_4$ nanotube array and (f) PCDs [78].

tending the photoresponse spectrum into the visible range. Reduced TiO_2 (R- TiO_2) shows clear improvements in PEC performance and photostability, as demonstrated by the current (J) vs. time (t) curves presented in Fig. 6c and d. Thus, surface modification with co-catalysts such as FeOOH paired with the creation of oxygen vacancies using NaBH_4 could produce an enhanced photocurrent and a chemically stable surface [77]. Following the reports by Li et al. [73] and Zhang et al. [59] in which a surface co-catalyst coating improved PEC performance, Dong et al.⁷² achieved PCD improvements simply by dipping the photoelectrode in NaBH_4 for two days. In both cases, the photoelectrode forms no hierarchical architecture or new surfaces. Hierarchical $\text{ZnO}/\text{ZnFe}_2\text{O}_4$ nanotube arrays (Fig. 6e) have also been reported by Long et al. [78] They observed a 2.2-fold enhancement of PCD and 3.6-fold increase of hydrogen production for $\text{ZnO}/\text{ZnFe}_2\text{O}_4$ compared to those of pristine ZnO samples. Without directly comparing these two approaches (Dong et al. [77] and Long et al. [78]) because of the different active materials used, we can nonetheless conclude that the reduced surface (TiO_2) enhances the PCD by almost $6 \times$, but the photocurrent remains lower than that in hierarchical $\text{ZnO}/\text{ZnFe}_2\text{O}_4$ nanotube arrays (PCD of 1.3 mA cm^{-2}). It is important to note here that the presence of Fe may contribute to the visible-light trapping ability of the photoelectrode and thereby improve the performance. Thus, we inferred from these three approaches that the photoelectrode surface should have oxygen vacancies, co-catalysts, and hierarchical layer formation to maximize the harvesting of solar light. Finally, the elemental composition or composite structure should improve the photoelectrode conductivity.

3.4. Flexible photoelectrodes

Very recently, researchers have expanded water-splitting electrode materials to incorporate novel transparent and soft technology in the photoelectrode [79–82]. (R1-2) As reported by Tyagi et al. [82] III-nitride nanostructures such as GaN nanorods grown on bulk substrates enable production of high performance devices, such as LEDs. However, additional process steps that can disrupt the alignment of nanorods are required to transfer them onto flexible substrates. Thus, growth of such nanostructures directly onto flexible metal foils has become an attractive alternative. In addition to flexibility, advantages of metal foils include their high thermal and electrical conductivity, cost effectiveness and scalability. Also, use of such flexible metal foils can simplify device fabrication processes for industrial production. GaN nanorods on flexible metal substrates demonstrated a photocurrent of $20 \mu\text{A cm}^{-2}$ at 0.4 V as shown in Fig. 7a and b; however real bending tests were not reported. Singh et al. [79] prepared flexible photoelectrodes of PVDF/Cu/PVDF- NaNbO_3 for PEC. Further, the incorporation of NaNbO_3 , with ferroelectric properties, enhanced the efficiency of the PEC water splitting by electrically polarizing the photoelectrodes. When an external electric field is applied to ferroelectric materials, they become polarized to produce a built-in potential that rapidly separates photogenerated charge carriers. As a result, the positively poled photoanode exhibited a higher photocurrent of $\sim 1.37 \text{ mA cm}^{-2}$ (Fig. 7c and d) than that of the as-prepared (non-polarized) photoanode ($\sim 0.72 \text{ mA cm}^{-2}$). However, the soft devices require flexible photoelectrodes, which should be demonstrated with bendability and retention tests as demonstrated by Quynh et al. [83] and Jo et al. [46] Both research teams have demonstrated excellent bendability and retention of performance after several hundred bending cycles for their respective photoelectrodes. Thus, with advances in water splitting, PEC cells can be achieved that show flexibility, portability, light weight, and human-friendliness. Quynh et al. selected transparent and highly pliable muscovite mica as a substrate for the deposition of ZnO by pulsed laser deposition (PLD) [83]. Compressive and tensile bending to radii of 3.5–20 mm were performed for 3000 cycles; the ZnO -mica electrode demonstrated almost 100% retention of PCD, as shown in Fig. 7e.

A $\text{Fe}_2\text{O}_3/\text{ZnO}$ heterostructure reported by Quynh et al. delivered a PCD of $98 \mu\text{A cm}^{-2}$ at 1 $V_{\text{Ag}/\text{AgCl}}$.

In another report, Jo et al. developed a flexible conducting substrate of electrospun polyacrylonitrile fiber that was electroplated with Ni. They optimized the electrospinning, electroplating, and ZnO NW growth times to achieve the optimal PCD. ZnO NWs grown over flexible Ni fibers showed an impressive PCD of 1.14 mA cm^{-2} at 0.4 $V_{\text{Ag}/\text{AgCl}}$. Furthermore, Jo et al. tested the PCD over 1000 bending cycles; the photoelectrode exhibited almost 100% retention (see Fig. 7f) [46]. Such work supports the development of substrate-free and flexible photoelectrodes, promoting PEC water-splitting performance toward the capture and storage of clean energy.

4. Multilayered heterostructures

Multilayered semiconductor heterostructures provide control of current flow and charge separation through the formation of heterojunctions [84]. Some material combinations involved in the creation of multilayered structures include $\text{TiO}_2/\text{BiVO}_4$, $\text{TiO}_2/\text{Fe}_2\text{O}_3$, $\text{BiVO}_4/\text{FeOOH}/\text{NiOOH}$, $\text{Ni}(\text{OH})_x/\text{MoO}_3$, and $\text{Ni}(\text{OH})_x/\text{ferrihydrite}$. These semiconductors with bandgaps of 2.1–3.2 eV can absorb incident rays in the visible to ultraviolet region of the solar spectrum to yield photocurrents via photogenerated electron–hole pairs. The separation of electron–hole pairs generates a built-in electric field by forming a depletion region, or Schottky contact, that drives the photogenerated charge carriers in opposite directions, separating them effectively. However, carrier immobilization in trap states, sluggish OER or HER kinetics at the electrode–electrolyte interface, and photocorrosion have been severe issues for these structures. Thus, along with multilayered structure formation, the deposition of oxygen or hydrogen evolution catalysts (OEC or HEC, respectively) onto the surface of the photoelectrode often improves the device performance. Such multilayer structures are categorized as: i) type-II heterostructures, especially bilayers; ii) Z-scheme structures in both bi- and multilayers; iii) co-catalyst and plasmonic coatings; and iv) surface passivation layers.

4.1. Type-II heterostructures

As discussed earlier, performance of a single photocatalytic electrode can be hindered by the fast recombination of photogenerated charge carriers. The formation of nanostructures can reduce the distance that charge carriers must diffuse to reach a reaction site, but nanostructuring alone is generally insufficient to suppress electron–hole recombination. The formation of bilayers or multilayers using materials with both wide and narrow bandgaps provides a means of directing charge transport. These bilayers are aligned such that electrons and holes can be transferred from one layer to another in a typical type-II heterostructure. The efficiency of electron and hole injection depends on the positioning of the CB and VB of each semiconductor layer. In a bilayer structure, a wide bandgap has a strong redox capacity while narrow-bandgap materials have higher light absorption abilities. As discussed by Choudhary et al. [19] in detail, n - n , p - p , p - n , and n - p semiconductor combinations can all form efficient type-II heterostructures. When a bilayer heterostructure is illuminated with light of the appropriate energy, electron–hole separation occurs in one or both layers, depending on their bandgaps. If the heterostructured film is the photoanode, the electrons in photosystem layer 1 (PS-1) with the higher-energy CB migrate to the lower-energy CB of PS-2. At the same time, holes in the VB of PS-2 migrate to that of PS-1. This transfer of electrons and holes allows efficient charge separation and suppresses recombination. Holes accumulate in PS-1 which is in contact with the electrolyte, and drive water oxidation; the electrons in PS-2 are transported to the photocathode for water reduction at the counterelectrode. The mechanism is reversed if the bilayer electrode is the photocathode, i.e., electrons are pushed towards the electrolyte for water reduction while holes are transported to the external circuit.

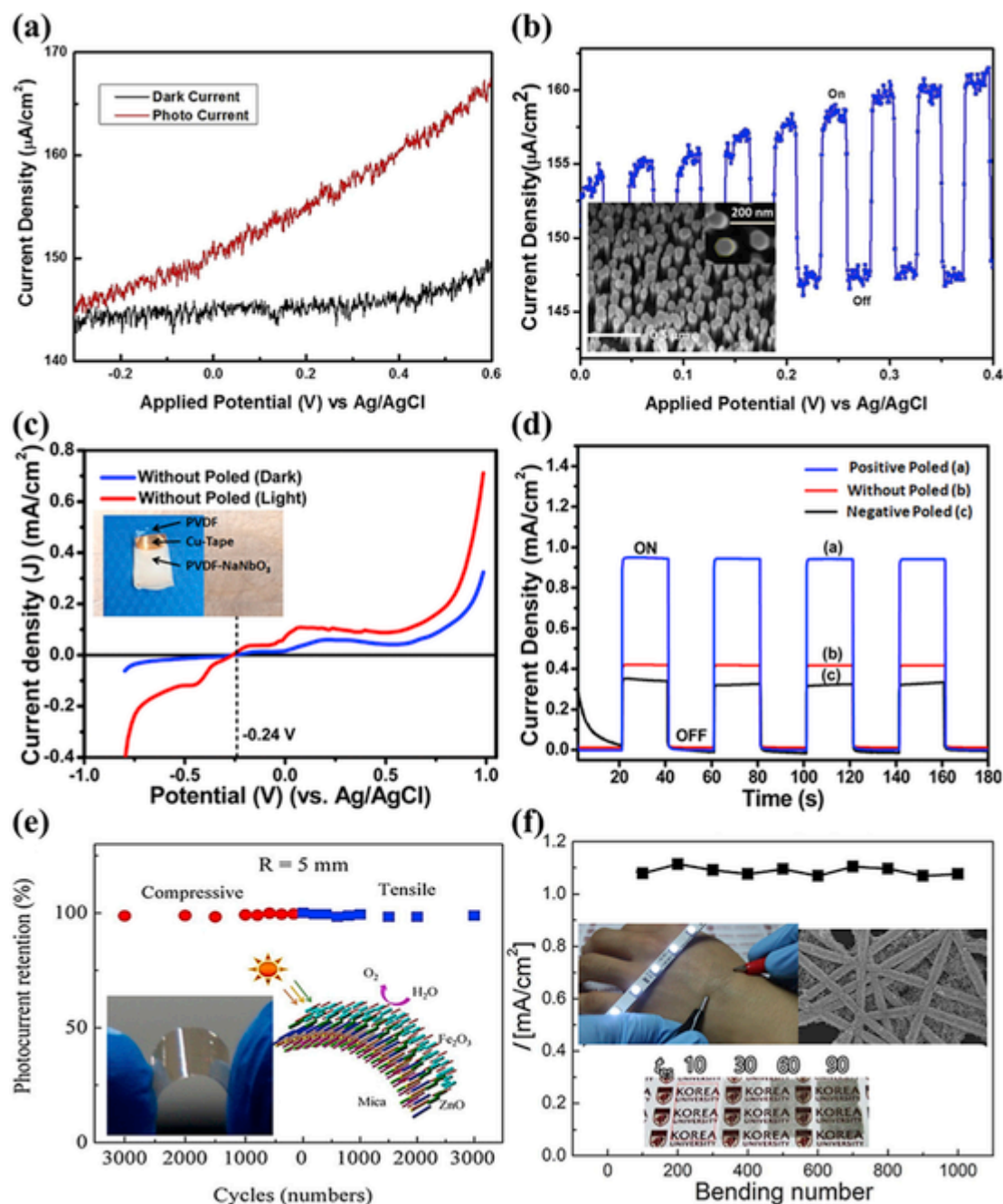


Fig. 7. PCD of (a, b) GaN nanorods grown over flexible Ta metal [82], (c, d) flexible ferroelectric PVDF/Cu/PVDF-NaNbO₃ photoanode [79]. Bending test of (e) Fe₂O₃/ZnO [83] and (f) NiF/ZnO NW [46], under 1 sun illumination.

Numerous bilayer structures have been reported; recent type-II heterostructures comprising WO₃, TiO₂, BiVO₄, Fe₂O₃, and Cu₂O, among others, are listed in Table 3. For an efficient type-II bilayer structure, the thickness of both layers should be optimized to maintain the built-in electric field effect while also achieving sufficient light absorption and carrier transport out of the layers. With a very thick electrode, the built-in field is reduced, which allows recombination. Mali et al. reported a layer-thickness optimization in which they obtained an enhanced photocurrent of 3.3 mA cm⁻² @ 0.7 V_{Ag/AgCl} for a bilayer film of 20-min electrospayed WO₃ on a 40-min electrospayed BiVO₄ pillar structure under a Na₂SO₃ electrolyte. Na₂SO₃ is a hole scavenger that induces faster charge carrier generation and separation [89]. Xu et al. reported a core-shell heterostructure of WO₃/BiVO₄ formed via an electrospinning and immersion processes. The nanofiber morphology

of the WO₃/BiVO₄ type-II heterostructure showed a high photocurrent that suggested rapid redox reactions at the electrode-electrolyte interface [90]. Zhang et al. [85] reported the hydrothermal preparation of a WO₃ nanoplate array on which a conformal BiVO₄ layer was deposited by spin-coating. SEM imaging of the optimized BiVO₄/WO₃ samples (Fig. 8a) shows densely packed nanoplates; the bilayer shows enhanced light absorption and provided a PCD of 1.6 mA cm⁻² at 1.23 V_{RHE}. However, increasing the concentration of BiVO₄ increases the thickness, which in turn increases the diffusion pathway length for charge carriers; charge recombination approaches that of the bulk case with increasing thickness. The formation of the type-II heterostructure improved the charge separation and transport efficiency of the photoanode.

Table 3
Overview of multilayered heterostructures.

Substrate/Materials	Fabrication Technique	Electrolyte	PCD [$\text{mA}\cdot\text{cm}^{-2}$]	V vs. RHE [V]
Type II				
FTO/ $\text{WO}_3/\text{Fe}_2\text{O}_3$ [186]	Electrodeposition/CBD	0.5 M Na_2SO_4	1.25c@0.8V	1.04
FTO/ $\text{WO}_3/\text{Cu}_2\text{O}$ [187]	Hydrothermal/electrodeposition	0.1 M H_2SO_4	1.37^b@0.8V	0.8
FTO/ $\text{WO}_3/\text{CuWO}_4$ [188]	Hydrothermal/dipping	0.2 M Na_2SO_4	1.21a@1.5V	1.7
FTO/ $\text{WO}_3/\text{CdS}/\text{NiOOH}/\text{CoPi}$ [189]	Hydrothermal/SILAR/photoelectrodeposition	0.2 M Na_2SO_3	2.59^b@1.0V	1
FTO/ $\text{CuWO}_4/\text{Mn}_2\text{O}_3$ [138]	Spin coating	0.2 M Phosphate buffer	0.05^b@1.2V	1.2
ITO/ ZnO/MoS_2 [190]	MOCVD	0.1 M Na_2S	0.93d@0.2V	0.14
FTO/ $\text{W}-\text{TiO}_2/\text{BiVO}_4$ [160]	Solid state diffusion/hydrothermal	1.0 M Phosphate buffer	2.5^b@1.23V	1.23
ITO/ $\text{TiO}_2/\text{CeO}_2$ [191]	Sol-gel spin coating	1.0 M NaOH	2.1a@0.95V	1.15
FTO/ $\text{TiO}_2/\text{BiFe}_2\text{O}_3$ [192]	spin coating	1.0 M NaOH	11.25c@1.5V	1.74
FTO/ $\text{TiO}_2/\text{MoS}_2$ [193]	Hydrothermal/dip coating nanoflower/nanosheet	1 M NaOH	0.24c@0V	0.24
ITO/ $\text{Fe}-\text{Zn}_{0.2}\text{Cd}_{0.8}\text{S}/\text{CuSbS}_2/\text{Co-Pi}$ [192]	Hydrothermal/Electrochemical	$\text{Na}_2\text{S} + \text{Na}_2\text{SO}_3$	0.35b@0.9V	0.9
FTO/ $\text{a-Fe}_2\text{O}_3$ NRs/ $\text{Sb}_2\text{S}_3/\text{Co-Pi}$ [102]	Hydrothermal/electrodeposition	1.0 M NaOH	1.14^b@1.23V	1.23
FTO/ $\text{WO}_3/\text{BiVO}_4$ [90]	Electrospinning/immersion	0.5 M Na_2SO_4	2.8^b@1.23V	1.23
ITO/ $\text{WO}_3/\text{BiVO}_4$ [89]	Electrospraying	1.0 M Na_2SO_3	3.31^a@0.7V	0.9
FTO/ $\text{WO}_3/\text{BiVO}_4/\text{Co-Pi}$ [85]	Hydrothermal/spin coating	0.1 M Phosphate buffer	1.8^b@1.23V	1.23
FTO/ $\text{SnO}_2/\text{BiVO}_4/\text{TiO}_2$ [194]	Spin coating	0.5 M Phosphate buffer	2.3^b@1.23V	1.23
Z-scheme				
FTO/ $\text{WO}_3/\text{Sb}_2\text{S}_3$ [158]	Hydrothermal	0.1 M H_2SO_4	1.79^b@0.8V	0.8
ITO/ $\text{In}_2\text{O}_3/\text{Bi}_2\text{WO}_6$ [75]	CBD/Electrospray	1 M KOH	1.03a@0.7V	0.7
Au/ $\text{Ga}_2\text{O}_3/\text{ZnO}$ [195]	Sputtering/Hydrothermal method	1 M KOH	0.6^a@1.5V	1.74
$\text{TiO}_2@\text{CdO}/\text{CdS}$ [93]	Hydrothermal/ionic layer absorption	0.3 M Na_2S and 0.2 M Na_2SO_3	3.2a@1.23V	1.23
$\text{Fe}_2\text{O}_3/\text{WO}_3$ [196]	Hydrothermal/deposition-annealing	0.1 M Na_2SO_4	1a@1.23V	1.23
CdS/CdO [197]	solution-liquid-solid	0.35 M Na_2S and 0.25 M Na_2SO_3	4.35@0V	0.24
$\text{Fe}_2\text{O}_3/\text{Ca}_2\text{Fe}_2\text{O}_5$ [198]	electrodeposition	1.0 M NaOH	0.31@0.5V	0.74
FTO/ $\text{Sb}_2\text{Se}_3/\text{Fe}_2\text{O}_3$ [199]	Thermal evaporation/hydrothermal	1.0 M NaOH	3.079^b@1.23V	1.23
Passivation				
FTO/ $\text{Fe}_2\text{O}_3/\text{TiO}_2$ [200]	Chemical solution deposition	1.0 M NaOH	1.23b@1.2V	1.2
FTO/ $\text{Fe}_2\text{O}_3/\text{TiO}_2$ [114]	Chemical bath deposition	1.0 M KOH	6.0b@1.23V	1.23
FTO/ TiO_2/ZnO [111]	ALD	0.5 M PBS	0.79b@1.23V	1.23
FTO/ $\text{Fe}_2\text{O}_3/\text{TiO}_2$ [201]	PECVD/ALD	1.0 M NaOH	2.0b@1.23V	1.23
ITO/ $\text{BiVO}_4/\text{ZnO}/\text{TiO}_2$ [71]	Electrospray/ALD	0.5 M Na_2SO_4	2.25^a@1.2V	1.4
FTO/ $\text{Fe}_2\text{O}_3/\text{TiO}_2$ [202]	ALD	1.0 M NaOH	1.01b@1.4V	1.4
ITO/ $\text{CuO}/\text{ZnO}/\text{TiO}_2$ [109]	Electrospray/ALD	1.0 M KOH	-4.1^a@-0.6V	0.8
FTO/ $\text{CuO}/\text{ZnO}/\text{TiO}_2/\text{AuPd}$	ALD/Sputtering	0.1 M Na_2SO_4	-5.4b@0V	0
FTO/ $\text{TiO}_2/\text{Fe}_2\text{O}_3$ [203]	Chemical solution deposition/hydrothermal	1.0 M NaOH	0.68^b@1.23V	0.8

PCD value at: $V_{\text{Ag}/\text{AgCl}}$ ^a, V_{RHE} ^b, V_{SCE} ^c, $V_{\text{Hg}/\text{Hg}_2\text{Cl}_2}$ ^d.

A wide- and narrow-bandgap heterostructure of ZnO–CdS nanosheets (Fig. 8c) was reported by Mahala et al. [86] ZnO with a two-dimensional (2D) nanosheet morphology was produced by electrochemical deposition and provided increased surface area for electrolyte contact. Furthermore, the addition of CdS with a bandgap of 2.4 eV by the successive ionic layer adsorption and reaction (SILAR) method provided optical activity under visible light. Nanosheets of ZnO decorated with CdS NPs are evident in the SEM image (Fig. 8c). The optimized ZnO–CdS (20 cycles) show a PCD of 1.15 mA cm^{-2} at 0 $V_{\text{Ag}/\text{AgCl}}$ under illumination. This PCD enhancement arises from the increased light absorption and carrier concentration from CdS. Further, the band edge potentials of ZnO and CdS allow the formation of a type-II heterostructure, which achieves effective charge separation by electron transfer from CdS to ZnO and hole transfer from ZnO to CdS (see inset of Fig. 8d). However, while the photostability of the heterostructure is better than that of pristine CdS, it remains poor compared with metal oxide electrodes.

Similarly, Wang et al. [87] designed a 3D WO_3 nanoplate/ Bi_2S_3 NR heterostructure (Fig. 8e) that combines wide- and narrow-bandgap materials, WO_3 (~2.7 eV) and Bi_2S_3 (~1.3 eV), respectively. In this case, to enhance the interfacial contact between the Bi_2S_3 NRs and WO_3 nanoplates, Bi_2S_3 seeding was performed on the WO_3 nanoplates by SILAR. The achieved heterostructure gave an impressive PCD of 5.95 mA cm^{-2} at 0.9 V_{RHE} . This photoanode provides a type-II heterostructure in which electrons are transferred from the CB of Bi_2S_3

to that of WO_3 whereas holes are transferred from the VB of WO_3 to that of Bi_2S_3 . This transfer of photogenerated charge carriers increases photocurrent by reducing recombination. The study showed that fully coating the area of the bottom layer was essential for the formation of a high quality interface between the two layers. Such an interconnected coating between the two material layers facilitates charge transfer and reduces recombination. A type-II heterostructure can also be formed between two low-bandgap materials, CuInS_2 and SnS_2 , as reported by Zhang et al. [88] Hydrothermally grown CuInS_2 and SnS_2 form hierarchical nanosheets (Fig. 8g) that enhance the electrode–electrolyte interface and provided a PCD of 3.56 mA cm^{-2} at $-0.45 V_{\text{RHE}}$. This enhanced photocurrent arises from the increased light absorption and the type-II structure of the photocathode, which injects electrons from the CuInS_2 CB to that of SnS_2 (see inset of Fig. 8h) to participate in water oxidation. Because metal sulfides suffer from photocorrosion, the photocathodes were covered with C_{60} , which both protects SnS_2 from direct contact with the electrolyte to inhibit photocorrosion and functions as an electron acceptor to promote charge transfer. These studies provide guidelines for the design of high-efficiency bilayer photoelectrodes.

4.2. Z-scheme

To increase photocatalytic activity in the visible region, researchers have attempted to mimic natural photosynthetic systems. In such sys-

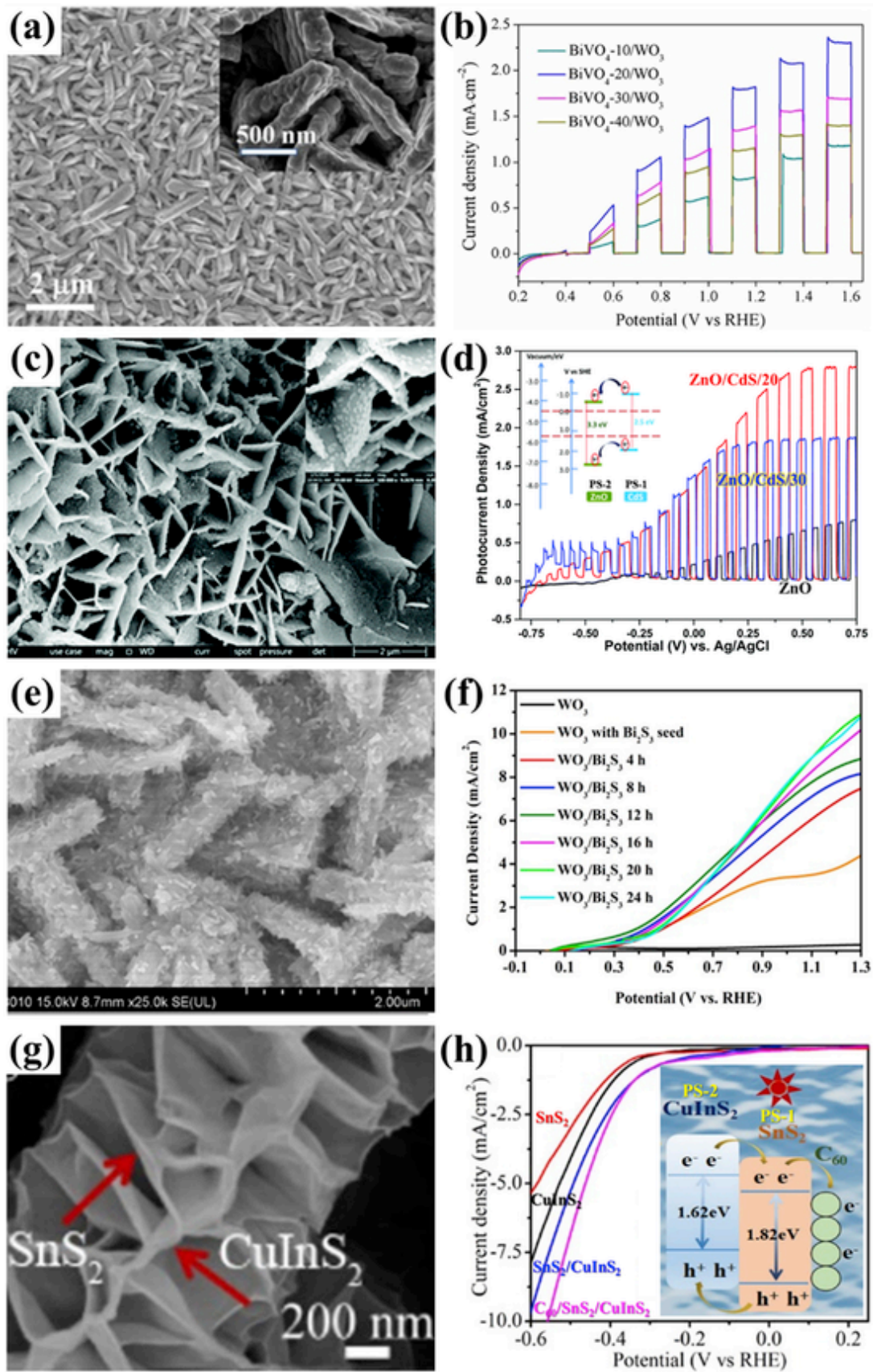


Fig. 8.

Morphology and PCD of (a), (b) BiVO₄/WO₃ [85], (c), (d) ZnO/CdS [86], (e), (f) WO₃/Bi₂S₃ [87], and (g), (h) CuInS₂/SnS₂ [88] (insets show charge transfer mechanisms). Reprinted with permission from Ref. [85–88].

tems, electron transfer occurs by a two-step photoexcitation and separation process via a specific arrangement of energy levels (called the Z-scheme) with separate oxidation and reduction centers. This mechanism allows a significant reduction in charge recombination and ultimately an enhancement in the light-harvesting capability while preserving the redox ability. In a direct Z-scheme system, under illumination, both systems in the photoelectrode absorb light; electrons in the CB of the active oxidizing PS recombine with holes in the strongly reducing PS. The charge transfer occurs by a path following a Z-shape. This combination preserves the electrons in the CB of the strongly reducing PS and holes in the strongly oxidizing PS [91]. In an early solid-state Z-scheme, the two PSs were connected via a plasmonic mediator in a PS-2/mediator/PS-1 system, such as TiO₂/Au/CdS. In this case, however, the Fermi levels become aligned and the band edges of TiO₂ and CdS rise to form a Schottky heterojunction that prevents the transfer of electrons from TiO₂ to CdS via Au, which makes this all-solid-state Z-scheme unfavorable [92]. Considering the limitations of all-solid-state direct Z-schemes in PEC water splitting, some such heterostructures are described in Table 3.

We reported a direct Z-scheme heterostructure utilizing In₂O₃ micro-cubes deposited by chemical bath deposition (CBD) as PS-2 and Bi₂WO₆ nanopillars as PS-1 [75]. The resulting heterojunction bilayer exhibited an enhanced PCD of 1.03 mA cm⁻² at 0.7 V_{Ag/AgCl}, exceeding those of the individual In₂O₃ and Bi₂WO₆ layers. The bandgap of the film was 2.4 eV, allowing more light-harvesting. Furthermore, the determined band-edge potential (Fig. 9a–c) indicates that the CB of In₂O₃ is more negative than that of Bi₂WO₆, whereas the VB of In₂O₃ is close to the CB of Bi₂WO₆; thus, the photogenerated holes in In₂O₃ and electrons in Bi₂WO₆ recombined easily. Correspondingly, all holes in the VB of Bi₂WO₆ are utilized for water oxidation, while the electrons in the CB of In₂O₃ are transferred to the counter electrode. Overall, this Z-scheme bilayer film of In₂O₃/Bi₂WO₆ demonstrates improved electron energetics for water reduction on the counter electrode because of the enhanced electron-hole separation efficiency.

A nanostructured CdS/CdO core-shell NR array reported by Li et al. [93] possesses a Z-scheme band structure (Fig. 9d–f). The heterostructure exhibited a PCD of 2.43 mA cm⁻² at 1.23 V_{RHE}, and the addition of TiO₂ nanocrystals further increased the PCD to 3.2 mA cm⁻² at

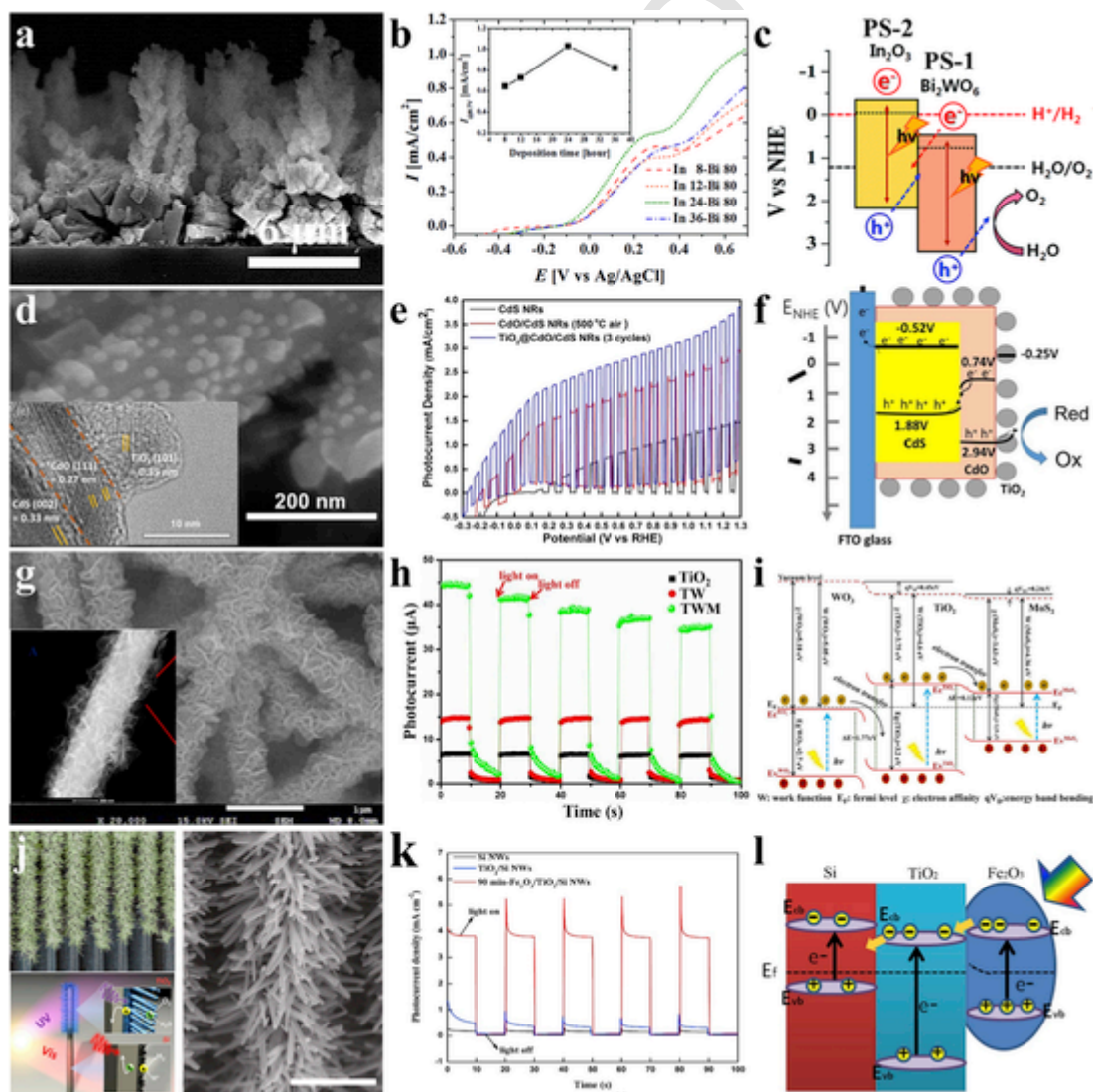


Fig. 9. Morphology, PCD, and mechanism of (a–c) In₂O₃/Bi₂WO₆ [75], (d–f) CdS/CdO/TiO₂ [93], (g–i) WO₃/TiO₂/MoS₂ [94], (j–l) Si/TiO₂/Fe₂O₃ [95,96]. Reprinted with permission from Ref. [75,93–96].

1.23 V_{RHE} . The core-shell CdS/CdO heterostructure showed enhanced interfacial charge transfer, providing effective charge separation and suppressing electron-hole recombination within CdS. The addition of TiO₂ nanocrystals passivated surface defects and trap states of CdO, contributing to the enhancement in PCD.

Zhao et al. [94] reported a multilayered structure in which a Z-scheme is formed between WO₃/TiO₂ and a type-II heterostructure is formed between TiO₂ and MoS₂ nanosheets to enhance H₂ evolution (see Fig. 9g–i). This multilayer structure was prepared by a combination of electrospinning and hydrothermal processing. The transient photocurrents demonstrate an obvious response to light for the different heterostructures; however, the photocurrent value is low. The poor PCD response could arise from the solid-state Z-scheme formation, which could be mitigated by introducing a semiconductor of appropriately matched bandgap, usually on PS-1 of the Z scheme heterostructure. Addition of such a semiconductor over PS-1 forms a type II heterostructure that provides efficient electron hole separation.

An asymmetric nanoscale tree-like heterostructure of Si NWs covered with TiO₂ NWs was reported by Liu et al. [95] It absorbed light in two different wavelength regimes. However, the quality of the interface between the *p*-type Si NWs and *n*-type TiO₂ NWs was poor, yielding low PCD. The interface could potentially be further improved by adding a metallic or silicide contact. Recently, Zhang et al. [96] designed a hierarchically structured photoanode using *n*-type Si NWs covered with spray-coated TiO₂ followed by hydrothermally grown Fe₂O₃ nanothorns. Such 3D structures increase light absorption and the surface area for electrolyte contact, ultimately producing a PCD of 3.5 mA cm⁻² at 1.23 V_{RHE} (Fig. 9j–l). The energy level diagram of such a multilayer structure shows a combination of the Z-scheme formed between the Si NW and TiO₂ and a type-II heterostructure between TiO₂ and Fe₂O₃ that eventually enhances charge separation and thus increases the PCD. Such hierarchical material design with attention to band alignment and interfacial efficiency is needed for efficient PEC water-splitting under practically useful conditions.

4.3. Co-catalyst and plasmon layers

During photoelectrochemical water splitting, the photocatalytic activities may decrease over time because of the reverse reaction to form H₂O. Hence, multilayer photoanodes have been capped with water-permeable layers of materials such as Cr₂O₃ to restrict the interaction of protons with electrons at the interface and thereby alleviate the reverse reaction. Addition of co-catalysts for photocatalytic water-splitting can be important for proton reduction to hydrogen and for water oxidation. The half-reaction for water splitting is as follows [97].

$$h^+ + D \leftrightarrow D^+ + 4h^+ + 2H_2O \leftrightarrow O_2 + H^+ \text{ (water oxidation half-reaction, where D is an electron donor, e.g., OH}^-, S^{2-}\text{)}$$

$$e^- + A \leftrightarrow A^- \text{ or } 2e^- + 2H^+ \leftrightarrow H_2 \text{ (proton reduction half-reaction, where A is an electron acceptor, e.g., H}^+, Ag^+\text{)}$$

A co-catalyst efficiently catalyzes the photocatalytic reaction by providing additional reaction sites and promoting charge separation, driven by the junctions and interfaces formed between the photocatalytic materials and the co-catalyst. Moreover, oxidative co-catalysts also reduce the photocorrosion of materials like CdS, thus improving the photostability of photoanodes. The photostability improvement may arise from the ability of oxidative co-catalysts to remove photogenerated holes from the light-harvesting semiconductors. The efficient overall PEC reaction requires equally suitable reduction and oxidation reactions that can be achieved using an earth abundant co-catalyst for hydrogen and oxygen evolution, as presented in Fig. 10a. The presence of the proper co-catalyst can significantly reduce bulk recombination of electron-hole pairs and enhance charge transfer to the surface for efficient PEC water oxidation and reduction, by ensuring rapid consumption of charge carriers that reach the co-catalyst. Both co-catalyst

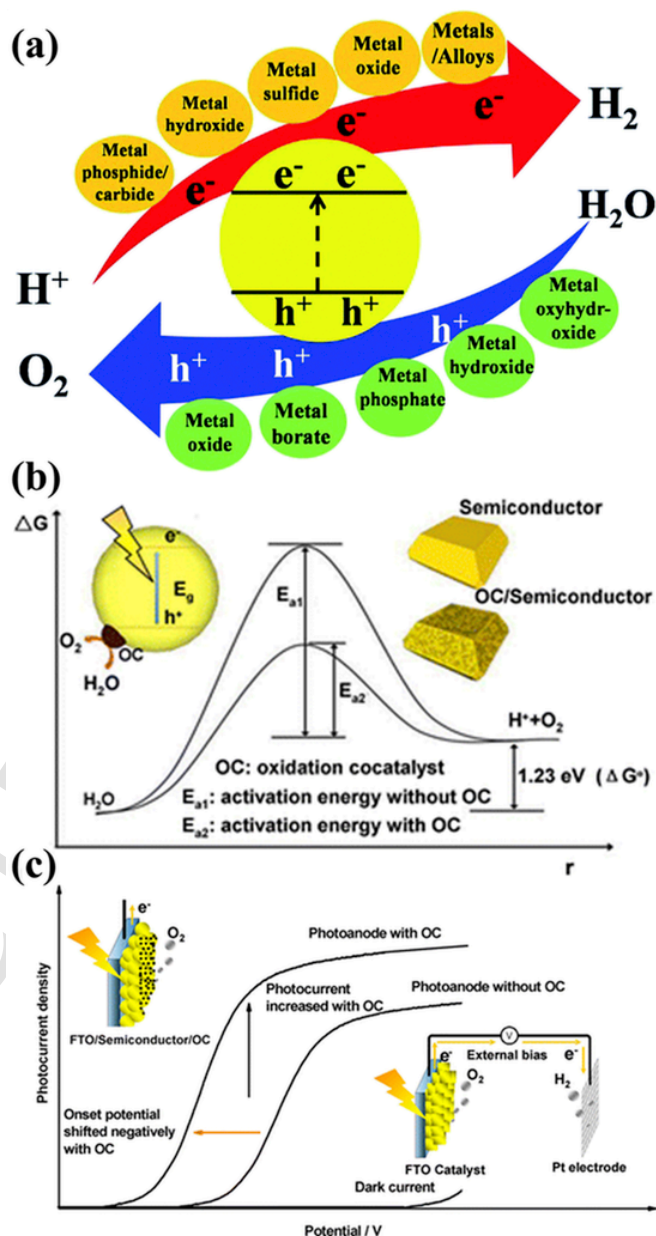


Fig. 10. Schematic of (a) co-catalyst for both OER and HER during PEC water splitting [98]; (b) water oxidation, and (c) PEC water oxidation. Reprinted with permission from Refs. [97].

and morphology engineering strategies must be chosen carefully to minimize surface recombination. Passivation layers will be discussed later in section 4.4.

As described in Section 2 regarding water oxidation and reduction, the minimum potential required for PEC oxidation is 1,23 eV (with associated increase in Gibbs energy of $\Delta G^\circ = 237$ kJ/mol). However, the kinetic barrier to reaction can be much larger. The role of a co-catalyst is to reduce this barrier, providing a lower-energy path from reactant (water) to products, as shown in Fig. 10b. The activation energy for a bare photoelectrode is significantly higher than that of a photoelectrode with an effective oxidative catalyst. Thus, as shown in Fig. 10c, the co-catalyst drastically reduces the overpotential and enhances the PCD of the photoelectrode.

Zhou et al. [9] suggested that 3D photocatalytic materials have excellent performance because they allow faster charge transfer and efficient utilization of incident light compared to one-dimensional

(1D) and 2D structures. Furthermore, ternary oxides contribute both *d*-orbitals and O 2*p* orbitals to the valence maxima, permitting fine-tuning of the bandgap energy. Fig. 11a and c, as reported by Peng et al. [99] and Zhou et al. [9], show PCD values for nanoflakes and nanoflowers of CuWO₄ and their composites, respectively. The nanoflakes [99] of CuWO₄ deliver the PCD of 0.32 mA cm⁻² at 1.23 V_{RHE}, and nanoflowers [9] of CuWO₄ deliver 0.4 mA cm⁻² at 0.8 V_{RHE} (see Fig. 11a and c). The CuWO₄ has an indirect bandgap, which means that a higher thickness is required for absorption of light. The increased thickness generates charge transfer resistance that limits the rate of the OER reaction at the electrode/electrolyte interface. The presence of another semiconductor layer over the photocatalytic CuWO₄, such as BiVO₄ [99] or CdS [9], facilitates directional charge separation at the semiconductor–CuWO₄ interface. The unidirectional flow of major charges enhances the PEC performance, thereby significantly increasing the photocurrent, as demonstrated by Peng et al. [99] and Zhou et al. [9]. Note that the absorbance range is not extended when the bandgap of the two semiconductors is the same, as in the case of CuWO₄ (2.37 eV) and BiVO₄ (2.36 eV). However, the OER on BiVO₄ has a large overpotential. Large reaction barriers arise on many surfaces because the OER involves four protons and four electrons in the PEC process [102]. Therefore, co-catalysts (such as Co-Pi [99] and FeOOH [9]) with the advantages described earlier are added to achieve enhanced PCD and photostability. The CuWO₄/BiVO₄/Co-Pi photoelectrode provided a high PCD of 2.25 mA cm⁻² at 1.23 V_{RHE} because of the synergistic effects of the double-layered oxide structure (CuWO₄/BiVO₄) and the co-catalyst (Co-Pi) located at the surface, as depicted in Fig. 11b. The enhancement in PCD arises from larger numbers of holes reaching the surface and decreased electron–hole recombination in the bulk region of the oxide active materials.

Like co-catalysts, plasmonic metal–semiconductor heterostructures have received considerable attention for PEC water-splitting enhancement. NPs of plasmonic metals like Au and Ag work as photosensitizers with semiconductors, allowing light absorption into the infrared region via their strong light-scattering abilities and local field enhancement associated with localized surface plasmon resonance (LSPR) phenomena [100,103]. The addition of such noble metals can produce additional electrons in the CB of the underlying semiconductor, which decreases charge carrier recombination. These surface plasmon resonance (SPR) NPs are commonly used for H₂ evolution; they can be used for O₂ evolution, but the process is more complicated. In addition, complete contact is required between the metal NPs and the semiconductor to utilize holes for water oxidation. Some well-known metal NPs used with semiconductors include Au, Ag, Pt, Pd, and Ir for H₂ evolution; among these, Pd, Au, Ag, and Ir can also be used for O₂ evolution [104]. Au NPs, which have tunable plasmon resonances in the visible frequency range, were used to achieve SPR with TiO₂ [105], Fe₂O₃ [106], and BiVO₄ [106], among other oxide semiconductors. Recently, Subramanyam et al. [100] designed and synthesized Au NP-supported Bi₂S₃ NRs via hydrothermal and drop-casting methods. The AuNP/Bi₂S₃NR composites exhibited a PCD of 9.61 mA cm⁻² at 1.23 V_{RHE} and a corresponding STH of 5.78%, which is much higher than that of pristine Bi₂S₃. The charge-transfer mechanism of the composite electrode suggests that, under light illumination, Bi₂S₃ generates electron–hole pairs with absorption in the visible region. The energy levels of Bi₂S₃ show that it is an overall water-splitting material with CB and VB positions near the water reduction (−3.77 eV) and oxidation (−5.01 eV) potentials, respectively, at pH 12.4. Furthermore, the Fermi level of Au is below the CB of Bi₂S₃; therefore, photoinduced hot electrons migrate from the AuNP to the CB of the Bi₂S₃ NR and then to the fluorine-doped tin oxide (FTO) substrate. The electrons are then transferred to the Pt counter electrode for H₂ generation. Photogenerated holes in the VB of Bi₂S₃ react with sacrificial ions to reduce the photocorrosion of Bi₂S₃ (Fig. 11d and e).

Dutta et al. [101] reported Au/α-Fe₂O₃ films modified with gold nanostructure as noble-metal SPR materials. These Au NPs reduce electron–hole recombination in α-Fe₂O₃ by providing induced hot electrons and enhanced light absorption. The Au/α-Fe₂O₃ composite film exhibited an increase of photocurrent by two times compared to that of bare α-Fe₂O₃ (see Fig. 11f). The transient photoresponse demonstrated an efficient charge-separation process, where electrons move from the Au NPs toward the counter electrode via the α-Fe₂O₃ film. Consequently, the generated holes move toward the electrolyte for reaction with the electrolyte species. Thus, such noble-metal particles promote superior PEC water-splitting [107] by four main mechanisms: 1) enhanced light absorption; 2) optimal light scattering, particularly with relatively large (~100 nm) particles; 3) hot electron transfer under illumination that induces electron accumulation in the CB of the connected semiconductor; and 4) plasmon-resonant energy transfer, which generates more charge carriers, effectively achieved with smaller particles.

Dutta et al. [101] reported Au/α-Fe₂O₃ films modified with gold nanostructure as noble-metal SPR materials. These Au NPs reduce electron–hole recombination in α-Fe₂O₃ by providing induced hot electrons and enhanced light absorption. The Au/α-Fe₂O₃ composite film exhibited an increase of photocurrent by two times compared to that of bare α-Fe₂O₃ (see Fig. 11f). The transient photoresponse demonstrated an efficient charge-separation process, where electrons move from the Au NPs toward the counter electrode via the α-Fe₂O₃ film. Consequently, the generated holes move toward the electrolyte for reaction with the electrolyte species. Thus, such noble-metal particles promote superior PEC water-splitting [107] by four main mechanisms: 1) enhanced light absorption; 2) optimal light scattering, particularly with relatively large (~100 nm) particles; 3) hot electron transfer under illumination that induces electron accumulation in the CB of the connected semiconductor; and 4) plasmon-resonant energy transfer, which generates more charge carriers, effectively achieved with smaller particles.

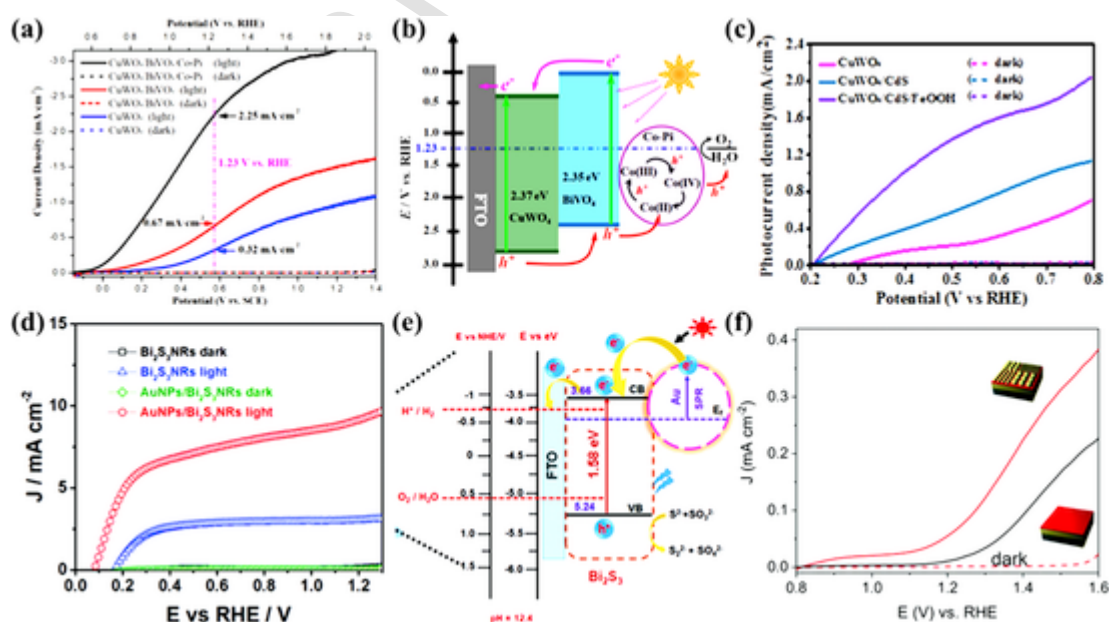


Fig. 11. (a), (c) PCD of CuWO₄-based composites using Co-Pi and FeOOH as OER layers; (b) mechanism with Co-Pi catalyst, (d), (f) PCD of Bi₂S₃ and α-Fe₂O₃ using Au NPs as noble metal catalysts; and (e) mechanism with Au NPs as plasmonic catalysts. Reprinted with permission from Refs. [9,99–101].

4.4. Passivation layers

Along with low STH values, the degradation of active semiconductors during PEC water oxidation is a major challenge to practical implementation of this technology. The deposition of a thin (<100 nm) passivation layer can modify electrode surfaces to prevent their degradation without significantly affecting charge transport. The passivation layer isolates the light-absorbing semiconductor from direct contact with the electrolyte, thus avoiding surface traps and protecting the photoelectrode surface from photocorrosion [108].

Our group reported the passivation of BiVO_4 pillars by thin layers of ALD-coated ZnO/TiO_2 films. This structure provided a high PCD

of 2.5 mA cm^{-2} at $1.2 \text{ V}_{\text{Ag/AgCl}}$ (Fig. 12a). The ALD coating cycles of ZnO and TiO_2 were optimized to enhance passivation and reduce interfacial charge recombination. The mechanism of the heterostructure relies on the thin layers of ZnO and TiO_2 deposited on the BiVO_4 nanopillars forming a heterostructure that efficiently separates electrons and holes and induces electrons to flow toward the ITO substrate. The thin layers of ZnO and TiO_2 allow holes to reach the surface without hampering the water oxidation process. The absorbed photon-to-current efficiency (APCE) curves indicate effective electron-hole separation, confirming enhanced light harvesting by the heterostructure [71].

A similar approach for the passivation of a CuO photocathode was demonstrated by Kim et al. [109], wherein CuO nanofibers are nanotextured to obtain so-called “thorny devil” structures (Fig. 12b). Such nanotextured fibers provide large accessible surface areas for elec-

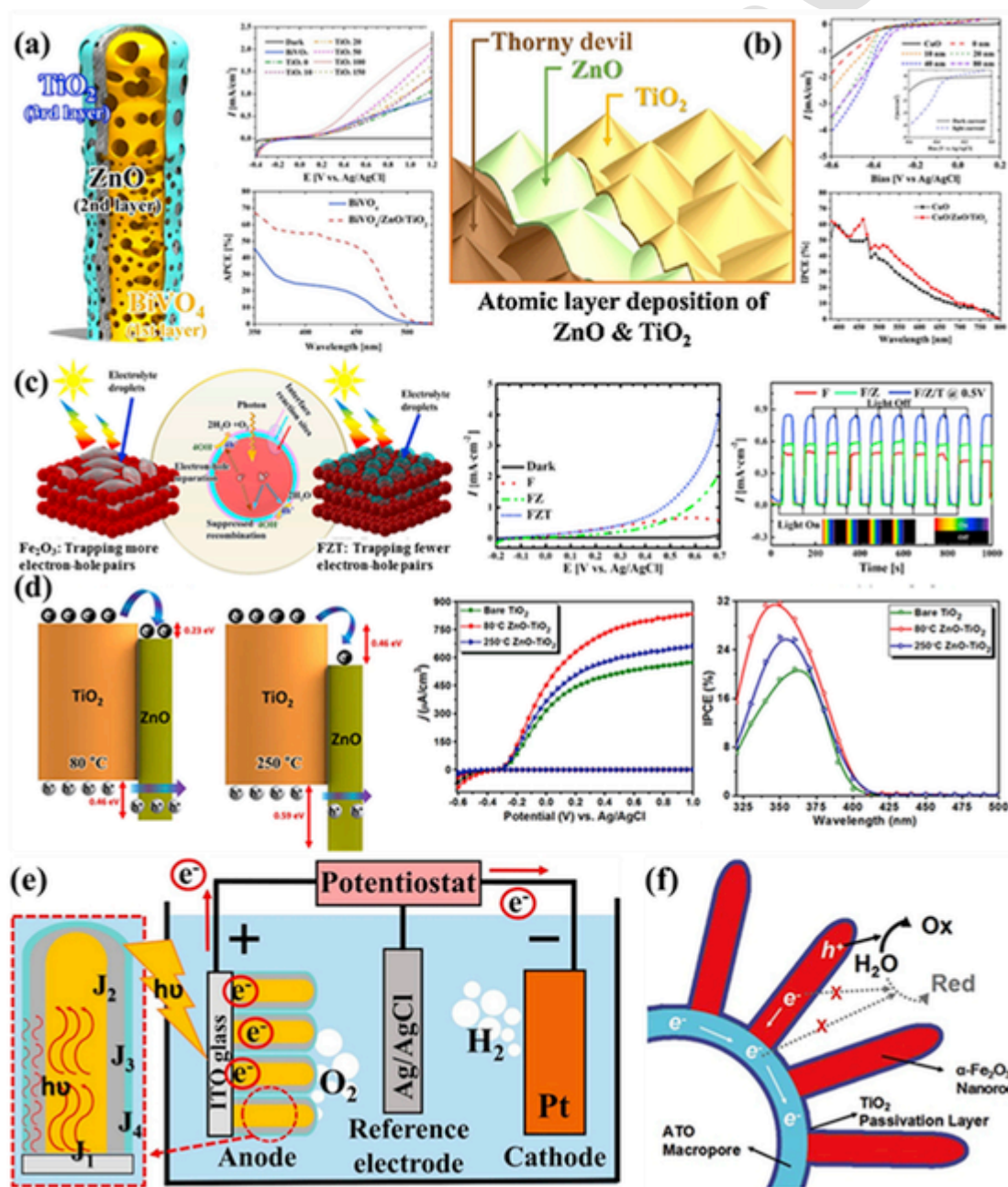


Fig. 12. (a) Passivation of BiVO_4 nanopillar, PCD, and APCE of $\text{BiVO}_4/\text{ZnO}/\text{TiO}_2$; (b) ZnO/TiO_2 thin films over nanotextured CuO , PCD, and IPCE of $\text{CuO}/\text{ZnO}/\text{TiO}_2$; (c) Mechanism of passivation layer effect on Fe_2O_3 , PCD, and transient photoresponse curves of $\text{Fe}_2\text{O}_3/\text{ZnO}/\text{TiO}_2$; (d) ZnO passivation over TiO_2 , PCD, and IPCE of $\sim 1 \text{ \AA}$ -thick ZnO over TiO_2 . (e) Schematic showing the mechanism of photocurrent enhancement by adding a passivation layer and (f) schematic showing the depletion region developed at the interface of the passivation layer and electrolyte, which reduces charge recombination. Reprinted with permission from Ref. [71,109–112].

trolyte interactions. The CuO nanofibers coated with thin layers of ZnO and TiO₂ by ALD cause electrons to migrate from CuO to TiO₂ while protecting the CuO surfaces from corrosion. The prepared CuO/ZnO/TiO₂ heterostructured photocathode exhibited a PCD of -4.1 mA cm^{-2} at $-0.6 \text{ V}_{\text{Ag}/\text{AgCl}}$. The IPCE plot indicated adequate light-harvesting capacity and exciton separation with 63.3% efficiency observed at 465 nm. The fabricated heterostructure absorbs a wide range of the solar spectrum from 380 to 800 nm (Fig. 12b).

In another similar study [110], the passivation of an Fe₂O₃ surface by ZnO/TiO₂ was confirmed by water contact-angle studies that demonstrated the protection of the Fe₂O₃ surface from direct electrolyte contact. The mechanistic schematic in Fig. 12c illustrates how the passivation of Fe₂O₃ reduces electron-hole recombination at the electrode-electrolyte interface to overcome issues of hole accumulation and photocorrosion in Fe₂O₃. While multilayered structures induce built-in electric fields for the effective separation of charge carriers, interfacial traps between layers can function as recombination centers that are detrimental for electron transport. Thus, the thickness of ZnO/TiO₂ was optimized to obtain an interface that provides smooth transport of both electrons and holes without recombination. This multilayered Fe₂O₃ photoanode demonstrated a PCD of 4.25 mA cm^{-2} at $0.7 \text{ V}_{\text{Ag}/\text{AgCl}}$. The transient photoreponse showed rapid increases and decreases in current density with on-off switching of the light source, confirming the fast charge-transfer characteristics and absence of traps. The excellent photoactivity and increased PEC performance of the Fe₂O₃/ZnO/TiO₂ heterojunctions corresponds to improved charge separation during water oxidation [110].

Ghobadi et al. [111] used an ultrathin ALD-coated ZnO layer to passivate hydrothermally grown TiO₂ NWs. This ultrathin ZnO film eliminates TiO₂ surface traps without affecting the carrier transfer dynamics. Further, optimization of the deposition temperature of ZnO revealed that a lower deposition temperature corresponded to a higher PCD of 0.78 mA cm^{-2} at $1 \text{ V}_{\text{Ag}/\text{AgCl}}$ (Fig. 12d). Characterization of band alignment revealed a smaller difference between the CB and VB energies of the TiO₂/ZnO bilayer at a lower ZnO deposition temperature (80 °C), suggesting that the band energies of ZnO become more positive to improve charge transfer. These examples provide insights for the control of processing parameters in the deposition of passivation layers to suppress recombination centers and enhance PEC performance.

The passivation layer can significantly enhance the photoconversion capability of the photoelectrode and protect the semiconductor from severe corrosion [113,114]. The presence of an ultra-thin passivation layer as indicated in Fig. 12e suppresses carrier loss by recombination of photogenerated electron-hole pairs. The designed photoelectrode pillar-like morphology ensures that the photoexcited electrons in the bulk BiVO₄ transfer rapidly to the ITO (current collector). Diffusion of the free electrons to the current collector is possible, as the passivation layers scavenge the holes at the TiO₂/electrolyte interface and consequently the electron lifetime in bulk BiVO₄ increases [71,115]. As illustrated in Fig. 12f the electrons are unable to cross the passivation layer, while the holes tunnel through ultrathin passivation layers. Consequently, the electron concentration is increased in the bulk semiconductor and transferred to the antimony doped tin oxide (ATO) macropore, which produced the improved IPCE and photocurrent observed by Xu et al. [112] Overall, the benefits of passivation layers to remove surface traps, tune band bending, prevent photocorrosion, retard charge recombination, facilitate oxygen escape, and improve surface kinetics are clear.

5. Nanocomposites and nanomaterials

Nanocomposites are formed by combining nanomaterials to obtain synergistic effects such as increased light absorption and tunable electronic properties that improve PEC water-splitting performance [116,117]. Many carbon-based nanomaterials are available and have been incorporated in nanocomposites for PEC water splitting. In this re-

view, carbon nanotubes (CNTs) [118,119], graphene [120,121], and graphitic carbon nitride (g-C₃N₄) [122,123] are considered. These materials have gained attention because they offer high surface areas, chemical and electrochemical stabilities, and electrical conductivities. Thus, nanocomposites based on them show performance improvements, such as efficient charge separation and faster electron transfer, from their enhanced conductivities. The relatively large surface areas of nanocomposites provides more sites for electrolyte interfacial reactions. The fabrication of such nanocomposites is significant because they overcome interfacial trap formation in multilayered heterostructures by providing superior contact formation to suppress electron-hole recombination. The following sections elucidate the characteristics of these individual materials and nanocomposites containing them.

5.1. CNT-semiconductor composites

CNTs have received extensive consideration for nanocomposite formation because they provide fast charge transport and reduced recombination of photogenerated electron-hole pairs in semiconductors, arising from their high electronic conductivities [124]. CNTs are allotropes of carbon that can exist as single-walled carbon nanotube (SWCNT) or multi-walled carbon nanotube (MWCNT). CNTs exhibit fewer dangling bonds and defects compared to carbon black. A single graphene sheet rolled into a closed cylinder is known as a SWCNT, and multiple rolled graphene sheets forming concentric cylinders constitute a MWCNT. The electronic properties of single-walled CNTs can vary from metallic to semiconducting based on the orientations of their graphene framework relative to the tube axis [125]. Semiconducting pristine CNTs alone exhibit negligible PEC activity due to their agglomeration due to van der Waals interactions; therefore, SWCNTs must be combined with other materials or functional dyes that demonstrate higher PCDs [126]. In addition, the modification of CNT surfaces with functional groups or surfactants before combining them with semiconductors can enhance the reactivity and photocatalytic activity of the final composite semiconductor [127]. Recent representative composites of CNTs with semiconducting metal nitrides, oxides, and sulfides, including GaN, TiO₂, Fe₂O₃, WO₃, ZnS, and CdS, for water-splitting applications are summarized in Table 4a.

Multiwalled CNT (MWCNT)-TiO₂ composite fibers on ITO, as reported by Veluru et al. [128], were observed to transition from transparent to gray and black (inset of Fig. 13a) with increasing MWCNT concentration from 2 to 20 wt percent (wt%). The SEM images in Fig. 13a show thread-like nanostructures that confirm the presence of CNTs. The addition of MWCNTs enhances the visible-light absorption capacity and contributes to improved charge separation and transport, yielding a PCD of $5.1 \mu\text{A cm}^{-2}$ at $1 \text{ V}_{\text{Ag}/\text{AgCl}}$ for 20 wt% CNT. This is four times higher than the PCD from TiO₂ fibers alone (see Fig. 13b). Similarly, Choudhari et al. [129] reported a five-fold increase in PCD with the addition of MWCNTs to ZnO. The chemically synthesized ZnO/MWCNT powder was dispersed in isopropanol and sprayed onto ITO before drying. The resulting films showed slightly reduced bandgap energy from 3.26 eV for ZnO to 3.22 eV for ZnO/MWCNT. The SEM image in Fig. 13c depicts spherical ZnO particles that are well mixed with MWCNTs. The PCD (Fig. 13d) of the composite was 1.14 mA cm^{-2} at $1 \text{ V}_{\text{Ag}/\text{AgCl}}$; however, the concentration of MWCNTs for this sample was not mentioned. The PCD enhancement was explained by the mechanisms shown in Fig. 13e and f. The electrons generated from electron-hole pair formation in ZnO under illumination are transferred to the MWCNTs to achieve Fermi-level equilibration. Further, with an external bias, the electrons are transferred to the counter electrode via the coated FTO substrate. Simultaneously, the holes diffuse to the ZnO surface for water oxidation. Thus, MWCNTs support faster electron transfer and thereby suppress the charge carrier recombination that occurs in pristine ZnO or TiO₂. The external bias is mandatory to direct the electrons and avoid electron-hole recombination [119,130].

Table 4a
Overview of CNT-based nanocomposite materials.

Materials	Nanostructures	Functionalization	Reaction solution	PCD [$\text{mA}\cdot\text{cm}^{-2}$]	V vs. RHE [V]	Ref.
Sapphire/GaN/CNT/Co-Pi	MOCVD/Dip/electrochemical	$\text{H}_2\text{SO}_4:\text{HNO}_3$ (3:1) @80 °C for 4Hr	1 M NaOH	2.81 °@0V		[132]
Sapphire/GaN/ZnO/CNT	MOCVD/Hydrothermal/dip	$\text{H}_2\text{SO}_4:\text{HNO}_3$ (3:1) @80 °C for 4Hr	1 M NaOH	3.02 °@0V		[133]
FTO/MWCNT/TiO ₂	Electrospinning	HNO_3 @110 °C for 15Hr	0.5 M Na ₂ SO ₄	5.1a @1V	1.2	[128]
FTO/TiO ₂ /CNT/Ag	Hydrothermal	6 M HCl @80 °C for 24Hr	0.5 M Na ₂ SO ₄	0.7a @1V	1.2	[119]
FTO/VO ₃ /CNT	Spin coating	–	0.5 M Na ₂ SO ₄	0.008a @0.6V	0.8	[124]
ITO/Fe ₂ O ₃ /MWCNT	Sol gel	–	1 M NaOH	2.8c @0.75V	0.99	[118]
ITO/Ti-Fe ₂ O ₃ /Cu ₂ O/CNT	Spray and spin	–	M NaOH	5.17 °@1 V	1.24	[134]
Au/SWCNT/InP/ZnS	Drop casting	–	Phosphate Buffer	0.0007 ° @0V	0.2	[204]
FTO/Cds/CNT	Hydrothermal drop casting	HNO_3 @140 °C	0.5 M Na ₂ SO ₄	0.04 °		[205]
FTO/ZnO/MWCNT	Chemical synthesis/spray	–	0.5 M Na ₂ SO ₄	1.14 ° @1V	1.2	[129]

Like TiO₂ and ZnO, GaN is a wide-bandgap material with the bandgap energy (E_g) of ~ 3.4 eV. Thus, GaN itself has little visible light absorption [131]. Therefore, a GaN/MWCNT photoanode was prepared to utilize MWCNTs as photosensitizers that enhance light absorption and promote electron transfer. Patil et al. [132] first deposited a GaN thin film by metal organic chemical vapor deposition (MOCVD) and later incorporated MWCNT through a dip and dry approach. Such GaN/MWCNT photoanodes showed a $2 \times$ increase in PCD (2.23 mA cm^{-2} at 0 V_{Pt}) compared to a bare GaN photoelectrode. The enhanced PCD could be attributed to the synergistic effect of the composite, with electron-hole pair formation in GaN and faster charge transport via MWCNT. However, increasing the amount of CNTs causes agglomeration due to strong van der Waals interactions over the GaN thin film that reduces the light reaching the GaN and thereby decreases the PCD. Therefore, optimal growth of CNTs is required on a thin film of GaN [132]. However, the earlier work of Patil et al. [133] reported higher PCD of 3.02 mA cm^{-2} at 0 V_{Pt} . Here, ZnO/CNT nanostructures were hydrothermally grown on MOCVD-prepared GaN. To use the MWCNTs, functionalization was performed to generate $-\text{OH}$, $-\text{C}=\text{O}$, and $-\text{C}-\text{O}$ groups on the MWCNTs. The addition of such functionalized MWCNTs during the hydrothermal synthesis of ZnO induced sheet-like growth because of the strong interactions between MWCNT and ZnO, which allow variation in the morphology from the rod-shaped ZnO/GaN. These composite photoanodes were further covered with MWCNT by a dip-dry process. The final GaN/ZnO-CNT/CNT photoanodes show a sheet-like morphology with threads, as demonstrated by the SEM image in Fig. 14a. A transmission electron microscope (TEM) image of a cross-section of the composite photoanode depicts a GaN thin film covered with ZnO sheets and MWCNTs (Fig. 14b). This nanocomposite heterostructure shows an enhanced PCD relative to the GaN/ZnO case, along with >2 h photostability (Fig. 14c). The enhanced PCD can be attributed to the type-II heterostructure formation between GaN and ZnO (Fig. 14d), where MWCNTs act as a scaffold material while ZnO supports faster electron transport and provides improved photosensitivity for harvesting longer-wavelength light [133].

CNTs have also been used with narrow-bandgap semiconductors such as Fe₂O₃ ($E_g \sim 2.1$ eV) [134], in which MWCNTs transported the photogenerated charge carriers from Fe₂O₃ to ITO to reduce charge recombination. Rai et al. [118] reported the optimization of the MWCNT concentration in an Fe₂O₃-based nanocomposite, obtaining a high PCD of 2.8 mA cm^{-2} at $0.75 \text{ V}_{\text{SCE}}$. Higher concentrations of MWCNTs induced agglomeration and reduced the PCD. Bilayer Fe₂O₃/MWCNT photoelectrodes produced a PCD of only 0.45 mA cm^{-2} at $0.75 \text{ V}_{\text{SCE}}$ because the agglomeration of CNTs limited their conducting behavior. Thus, the report suggests that the influence of MWCNTs is dominant when they are mixed with Fe₂O₃, because MWCNTs function as a conducting scaffold, yielding enhanced absorption and faster charge transfer. Like Fe₂O₃, LaTiO₂N ($E_g \sim 2.1$ eV) is also a low-bandgap material with a perovskite structure [135]. A LaTiO₂N/CNT composite material showed enhanced ultraviolet (UV) transmittance and lower transmit-

tance at visible wavelengths, arising from complex interactions between the film thickness and inhomogeneous morphology associated with the porosity of the electrode. The MWCNTs formed a web-like structure around the LaTiO₂N particles that enhanced electronic conductivity and improved the PEC performance.

5.2. Graphene nanocomposites

Graphene, an allotrope of carbon, is a 2D material comprising covalently bonded sp^2 -hybridized carbon atoms arranged in a hexagonal lattice. The characteristics of graphene, such as its excellent conductivity (10^6 S cm^{-1}) from the delocalized π electrons above and below the atomic plane, high surface area, and tailorable properties through chemical modification, endow it with significant potential for use in composites for water splitting [25,136]. However, graphene is mostly hydrophobic and metallic in its pristine form and cannot be used directly in PEC water splitting. Thus, chemical functionalization of graphene is necessary to tune its electronic properties and induce hydrophilicity to allow assimilation in the composite. For example, reduced graphene oxide (rGO) is semiconducting in nature, and oxygen-containing functional groups enhance its dispersibility with other catalytic materials [137]. Recent rGO-based composites are listed in Table 4b; the role of graphene in composites is discussed in the subsequent section.

Incorporating rGO in nanocomposites for PEC water splitting allows better visible-light absorption that increases photogenerated charge carrier formation and facilitates the acceptance and transport of electrons from another semiconductor, thereby efficiently suppressing electron-hole recombination. Hence, rGO has been used with various wide-bandgap materials like TiO₂, ZnO, and GaN and narrow-bandgap materials including BiVO₄, Fe₂O₃, WO₃, and Cu₂O [105,138–144]. The contribution of rGO in the nanocomposite depends on its bonding with the semiconductor. Hamid et al. [145] prepared rGO/ZnO films on ITO by two-step electrochemical deposition. ZnO nanorods grown directly on ITO are vertically aligned with preferential orientation in the [002] plane (Fig. 15a). Ethylenediamine works as a structure-directing agent in ZnO nanorod formation by forming a complex with Zn^{2+} that binds its nonpolar [101,110] planes. The addition of rGO before ZnO deposition yields non-uniform rods through the effects of oxygen moieties on rGO, which act as nucleation and adhesion sites for ZnO nanorod growth, as illustrated by the SEM image in Fig. 15b. Usually, with wide-bandgap metal oxides (M–O), the addition of rGO induces M–O–C bonding that decreases the bandgap energy of the composite [146–148]. However, Hamid et al. observed the bandgap of rGO/ZnO to increase from 3.56 to 3.63 eV due to the Moss-Burstein effect. Further, a linear-sweep voltammogram (LSV) (Fig. 15c) shows an increase in PCD from 1 mA cm^{-2} for ZnO to 1.8 mA cm^{-2} at $1 \text{ V}_{\text{Ag/AgCl}}$ for rGO/ZnO. This enhancement arises from faster charge transfer from the ZnO CB to rGO via π - π interaction, which hinders electron-hole recombination in ZnO. The work function of graphene is matched well with

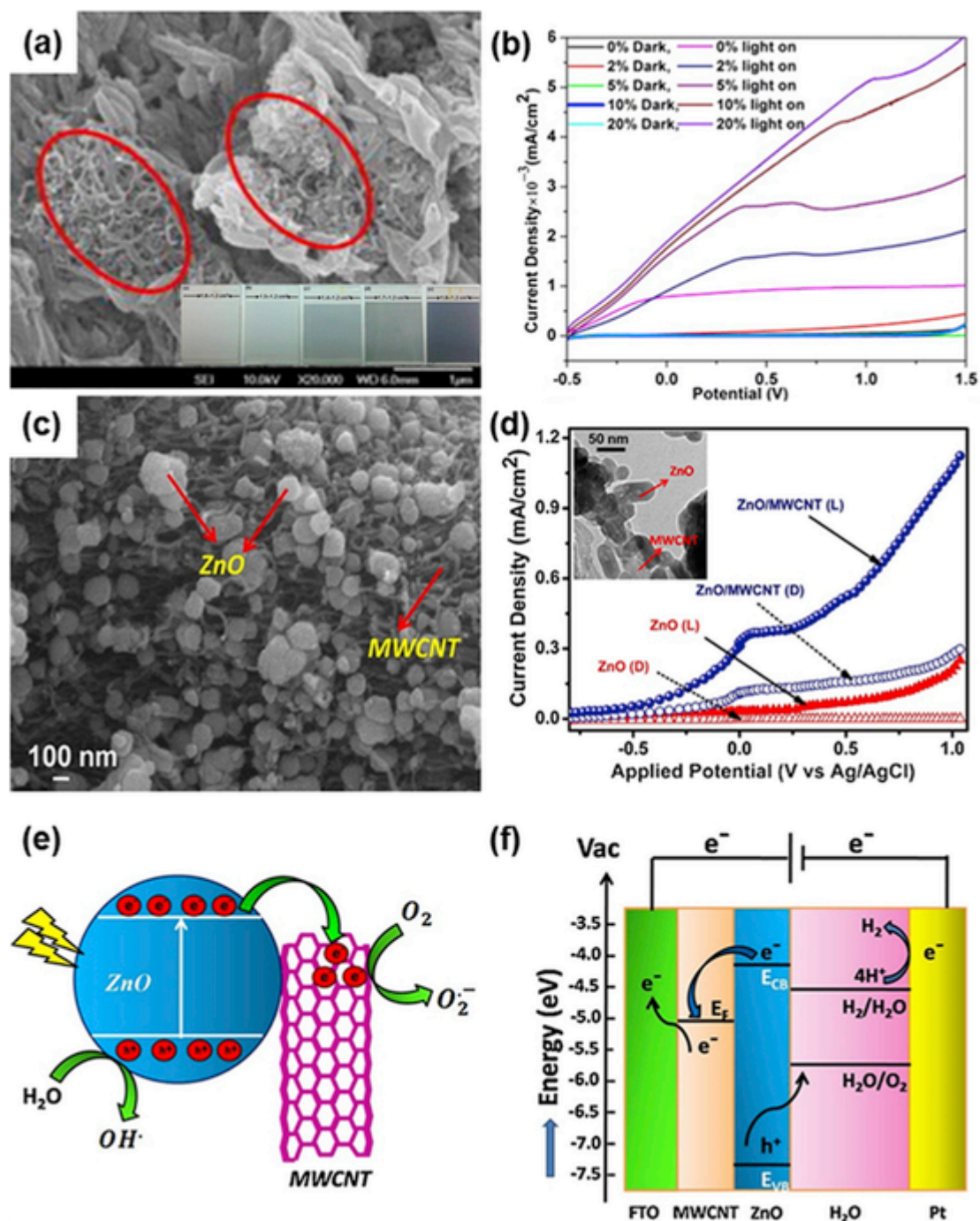


Fig. 13. (a) SEM images of MWCNT-TiO₂ nanocomposite with 20 wt% MWCNT, as highlighted by the red ovals, (b) PCD as a function of applied voltage for all compositions. Reprinted with permission [128]. (c) SEM images of the ZnO/MWCNT nanocomposite, (d) linear-sweep voltammograms for ZnO and ZnO/MWCNTs in the dark (hollow spheres) and under illumination (solid spheres), (e) band diagram schematic showing the electron-hole photogeneration in the ZnO/MWCNT nanocomposite, (f) electron-hole transfer under applied bias for PEC water splitting. Reprinted with permission from Refs. [129].

the CB position of ZnO, facilitating electron transfer from ZnO to rGO [146].

Han et al. [149] deposited pyramidal BiVO₄ by CBD over an FTO substrate, followed by spin-coating of a GO solution. The resulting film was then annealed at 350 °C under Ar for 3 h, reducing GO to rGO and increasing the rGO-BiVO₄ adhesion. The nanopyramidal morphology of BiVO₄ (Fig. 15d) was transformed into a rougher surface in the rGO/BiVO₄ because of the crumpled rGO layer that became intertwined with the tips of BiVO₄, as demonstrated in Fig. 15e. The optimized addition of rGO yielded a PCD of 0.81 mA cm⁻² at 1.23 V_{RHE}, as shown in

Fig. 15f. However, a higher amount of rGO may produce agglomeration and trap light in rGO itself, transmitting very little light to the underlying semiconducting material, which hinders photo induced charge carrier formation, thus reducing the PCD [146]. The photogenerated electrons must diffuse through the film to reach the FTO; the BiVO₄ nanostructure already reduces the pathlength for electron diffusion. Furthermore, the presence of rGO pushes electrons in the CB of BiVO₄, ultimately overcoming the recombination issue. Thus, the higher work function and conductivity of rGO are necessary to overpower the charge recombination for the rGO/BiVO₄ composite. However,

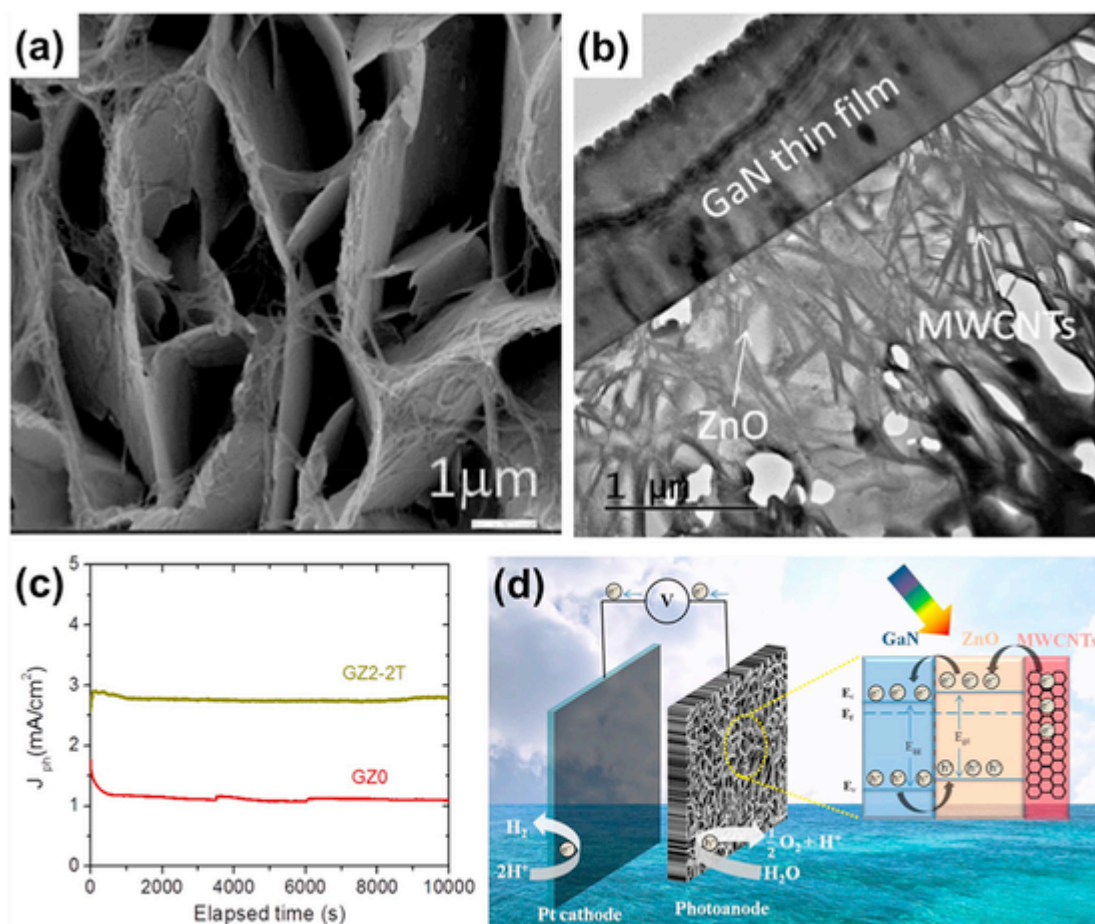


Fig. 14. (a) SEM image, (b) TEM image, (c) chronoamperometric J-T curves, and (d) schematic of PEC water-splitting mechanism of GaN/ZnO-CNT/CNT. Reprinted with permission from Ref. [133].

this mechanism was not distinctly explained by Han et al. when rGO was used as a top layer on BiVO_4 .

Self-assembled rGO quantum dot (rQD)-modified Fe_2O_3 worm-like nanostructures, as shown in Fig. 15g, were reported by Xie et al. [150]. The nanostructured Fe_2O_3 films deposited on ITO by a solution-based method were further immersed in a GO QD aqueous dispersion of pH 7. The isoelectric point of Fe_2O_3 is 9.3, yielding a positively charged surface strongly interacts with COO^- of GO QDs; therefore, spontaneous assembly of GO QDs occurs on the Fe_2O_3 . Thermal annealing in Ar at 450°C for 1 h reduces the GO QDs to rQDs on the Fe_2O_3 nanostructure, as observed by TEM (Fig. 15h), with a layer thickness of 5.1 nm. Even after high-temperature annealing, the bandgap of Fe_2O_3 was unchanged by the addition of rQD. A similar tendency was also observed in BiVO_4/rGO -based composites [151,152]. However, unlike previous reports, the $\text{BiFe}_2\text{O}_3/\text{rGO}$ composite [153] showed a decrease in bandgap energy to 1.85 eV, relative to the 2.25 eV band gap of BiFe_2O_3 . This decrease arises from electronic interactions between rGO and BiFe_2O_3 . The PCD details of this composite are listed in Table 4b. The impact of the rQD amount on Fe_2O_3 is shown in Fig. 15i, indicating that only a certain amount of rQD effectively enhances PCD because it reduces hole accumulation at the electrode-electrolyte interface [150]. As reported by various researchers, BiVO_4 - and BiFe_2O_3 -type materials show poor water oxidation kinetics because of the accumulation of holes at the interface, forming a Helmholtz layer [154] producing capacitance that restricts hole transfer. This issue is effectively solved by using rGO as the surface layer.

An rGO layer can be deposited between the layers of type-II heterostructures such as $\text{TiO}_2/\text{Sb}_2\text{S}_3$ and $\text{WO}_3/\text{Sb}_2\text{S}_3$ to improve the electrical conductivity and increase the efficiency of electron-hole pair sep-

aration. Recently, Sb_2S_3 has gained attention as a photosensitizer because of its low synthesis temperature and bandgap energy of ~ 1.74 eV in crystalline form. Lin et al. [155] and Song et al. [156] used it to form type-II heterostructures with WO_3 and TiO_2 , respectively. Fig. 16a and i demonstrate that rGO does not alter the actual bandgaps of the heterostructures. However, the effect of Sb_2S_3 changes the bandgap of WO_3 (2.8 eV)/ Sb_2S_3 (1.74 eV) to 1.5 eV and that of TiO_2 (3.2 eV)/ Sb_2S_3 (1.74) to 1.68 eV. Similar results are obtained for the $\text{TiO}_2/\text{Sb}_2\text{S}_3$ case (Fig. 16e). The solar-driven water splitting and recombination processes of the electrode can be studied based on the transient current response, i.e., under chopped illumination at a fixed potential (see Fig. 16b, f, and g). Under illumination, the photocurrent increases rapidly; this increase in the presence of rGO suggests that rGO facilitates the efficient transfer of electrons from Sb_2S_3 to WO_3 or TiO_2 , providing the synergistic effect of a type-II heterostructure and composite. However, the stability of the composite is better with TiO_2 than with WO_3 . Enhanced stability is imparted by TiO_2 and WO_3 ; therefore, the decrease in stability arises from the photocorrosive nature of Sb_2S_3 [156,157]. However, as reported by Song et al. [156], rGO improves electrode stability, but ultimately the electrode efficiency depends on the interface that affects the charge-transfer resistance. Zhang et al. [158] also showed enhanced stability without rGO for $\text{WO}_3/\text{Sb}_2\text{S}_3$ with a microcube-type WO_3 structure. This indicated that enhanced interfacial stability of heterostructures is a higher priority; the presence of rGO can further enhance both the PCD and stability.

To understand the charge-transfer mechanisms, Mott-Schottky characteristics are essential because they provide the flat-band potentials (E_{fb}). A Mott-Schottky plot with a positive slope indicates an *n*-type material; the E_{fb} value is generally just below the CB energy. The

Table 4b
Overview of graphene-based nanocomposite materials.

Materials	Nanostructures	Electrolyte	PCD [$\text{mA}\cdot\text{cm}^{-2}$]	V vs. RHE [V]	Ref.
FTO/TiO ₂ /GO	Hydrothermal/dip coating nanoflower/nanosheet	1 M NaOH	0.24 ^c @0V	0.24	[138]
GCE/S-Ti	Hydrothermal	1 M KOH	3.36 ^a @1V	1.2	[120]
O ₂ /S-RGO					
FTO/TiO ₂ /rGO	Spin coating	0.5 M Na ₂ SO ₄	0.75 ^b @1.23V	1.23	[105]
FTO/TiO ₂ /rGO/Sb ₂ S ₃	Hydrothermal/CBD/spin coating	0.5 M Na ₂ SO ₄	0.96 ^b @0.82V	0.82	[155]
Ti/H-TiO ₂ /rGO	Electrochemical/electrophoretic deposition	1 M KOH	0.138 ^b @1.23V	1.23	[206]
ITO/TiO ₂ /rGO	Hydrothermal	0.1 M KH ₂ PO ₄	2.59 ^a @0.6V	0.8	[147]
GCE/TiO ₂ /rGO	Solvothermal	1 M KOH	1.449 ^a @1.0 V	1.2	[207]
FTO/BiVO ₄ /GO	CBD/spin coating	0.5 M Na ₂ SO ₄	0.81 ^b @1.23V	1.23	[149]
FTO/BiVO ₄ /rGO	Chemical precipitation/drop cast	0.1 M Na ₂ SO ₄	0.544 ^a @1.2 V	1.4	[139]
FTO/Zn-BiVO ₄ /GQD	Electrochemical/hydrothermal	0.1 M Phosphate Buffer	4.58 ^b @1.23V	1.23	[152]
FTO/Mo-BiVO ₄ /rGO	Chemical synthesis/doctor blade	0.1 M Na ₂ SO ₄	8.51 ^b @1.23V	1.23	[151]
ITO/BiFe ₂ O ₃ /rGO	Chemical synthesis/drop cast	1 M KOH	10.2 ^a @1 V	1.2	[153]
FTO/Fe ₂ O ₃ /TiO ₂ /rGO	PECVD/CVD	0.1 M NaOH	0.85 ^b @1.23V	1.23	[140]
FTO/Fe ₂ O ₃ /GQD	Chemical synthesis/dip and dry	1 M NaOH	0.88 ^b @1.23V	1.23	[150]
ITO/rGO/Fe ₂ O ₃	Spray pyrolysis	1 M NaOH	4.0 ^b @1.23V	1.23	[141]
FTO/Fe ₂ O ₃ /rGO	Electrodeposition	1 M KOH	0.98 ^a @0.23V	0.43	[142]
FTO/Fe ₂ O ₃ /NiO/rGO	Electrochemical deposition	1 M KOH	2.45 ^a @0.7V	0.9	[143]
SPE/Fe ₂ O ₃ /ZnO/rGO	hydrothermal	0.1 M KOH	0.85 ^b @1.23V	1.23	[144]
GCE/ZnS/rGO	Hydrothermal	0.5 M Na ₂ SO ₄	1.05 ^b @1.23V	1.23	[121]
Cu/ZnO/rGO	Chemical synthesis	1 M NaOH	1.29 ^b @1.23V	1.23	[208]
ITO/rGO/ZnO	electrochemical	1 M KOH	1.8 ^a @0.7V	0.9	[145]
FTO/ZnO/rGO	Hydrothermal/dip	0.5 M Na ₂ SO ₄	2.4 ^a @0.8V	1	[148]
FTO/ZnO/rGO	Solgel	0.5 M Na ₂ SO ₄	1.0 ^a @1.5V	1.23	[146]
FTO/ZnO/Cu ₂ O/rGO	Hydrothermal/electrodeposition/electrochemical	0.5 M Na ₂ SO ₄	10.11 ^b @1.23V	1.23	[209]
FTO/WO ₃ /rGO/Sb ₂ S ₃	CBD/CBD/spin coating	0.5 M Na ₂ SO ₄	1.2 ^b @1.23V	1.23	[155]
Si/GaN/graphene	MBE/CVD	1 M NaOH	0.24 ^a @0V	0.2	[210]

CB edges for WO₃ and Sb₂S₃ are around 0.4 and 0.04 V, respectively (see Fig. 16c). Additionally, the charge carrier concentration determined from the Mott-Schottky plot also demonstrates that rGO increases the charge carrier density, contributing to faster charge transport. For TiO₂/rGO/Sb₂S₃, the E_{fb} value for TiO₂ shown in Fig. 16k is 0.06 V, making the CB of Sb₂S₃ more negative. The photocurrent obtained in the absence of UV light highlights the importance of adding narrow-bandgap Sb₂S₃ to wide-bandgap TiO₂, as observed from Fig. 16g. Further, the mechanisms in Fig. 16d and h, and i show that the CB of Sb₂S₃ is more negative than those of WO₃ and TiO₂. Hence, band bending occurs from Sb₂S₃ to WO₃ or TiO₂; photogenerated electrons injected from the CB of Sb₂S₃ to those of WO₃/TiO₂ move toward the counter electrode under the applied bias. Correspondingly, the VB of WO₃ or TiO₂ is above that of Sb₂S₃, which is also higher than the potential required for the PEC water splitting. Thus, holes from WO₃ or TiO₂ are smoothly transferred to the electrolyte through Sb₂S₃ to oxidize water, enhancing photocurrent. In both the WO₃/rGO/Sb₂S₃ and TiO₂/rGO/Sb₂S₃ composites, rGO works as a conductive layer that contributes to enhanced charge transfer and higher PCD.

5.3. Graphitic carbon nitride nanocomposites

Metal-free graphitic carbon nitride (g-C₃N₄, henceforth g-CN), rediscovered by Wang et al., in 2009 [159], has a layered structure like that of graphene sheets, in which each layer comprises tectonic rings of triazine and heptazine [160]. This material has attracted immense attention because of its electronic properties and bandgap of 2.7 eV, which is appropriate for visible-light absorption. It is suitable for use as a water-splitting photoelectrode material because its VB and CB are positioned at -1.15 eV and 1.55 eV (vs. a normal hydrogen electrode (NHE)), respectively, as calculated by the formula reported by Opoku et al. [161].

The g-CN can be synthesized by the polymerization of low-cost materials such as urea, melamine, and dicyandiamide by high-tempera-

ture heating (~500–550 °C) followed by room-temperature condensation [162–164]. Earlier, g-CN was prepared separately and coated on ITO as a slurry [165,166], but this resulted in poor adhesion. Recently, thin films were directly coated on ITO, as reported by Ye et al. [167], who used a CVD process at 550 °C with a starting reagent of mixed thiourea and melamine to achieve an S-doped g-CN film. Thiourea allows S doping and the film morphology was smooth and thin. S-doping caused a blue shift in the bandgap. The S-doped g-CN film delivered a PCD of 0.022 mA cm⁻² at 0.5 V_{Ag/AgCl}. The open-circuit potential was negative under light illumination, indicating electron transfer to the ITO side and confirming the role of g-CN as an *n*-type semiconductor. A different method of thermal vapor liquid-polymerization is used for g-CN film deposition by Lu et al. [168] The surface and cross-sectional SEM views (Fig. 17a, b) display flakes of g-CN, confirming the sheet-like surface morphology. A bandgap of 2.6 eV was determined from UV-visible absorbance spectra. These films exhibited a PCD of 0.089 mA cm⁻² at 1.1 V_{RHE} (Fig. 17c). However, both reports note that the photocurrent of g-CN is lower because of faster charge recombination and the comparatively lower band positions of VB and CB.

To address this problem, Zhang et al. [168] prepared P-doped g-CN micro-rods by the direct calcination of a reflux-treated ethylene diphosphonic acid/melamine complex. The complex compound annealed at 550 °C yielded a porous P-doped carbon nitride rod (P-CNR) (Fig. 17d). The bandgap energy, as determined from UV-visible absorption, was reduced to 2.29 eV for P-CNR. Thus, the VB edge shifted to 1.51 eV for P-CNR compared to 1.75 eV for g-CN, as shown in the band alignment diagram (Fig. 17e). This shift was attributed to the quantum confinement effect induced by the mesoporous structures of the micro-rods. The transient PCD curves (Fig. 17f) reveal the actual impact of P-doping, which enhances the photocurrent. This increase was attributed to enhanced light-harvesting capacity, increased active sites associated with mesoporosity, and higher mobility of photoexcited charge carriers.

To improve the photocatalytic activity of g-CN, a new 3D structure was proposed by Chen et al. [169] to enhance the surface area

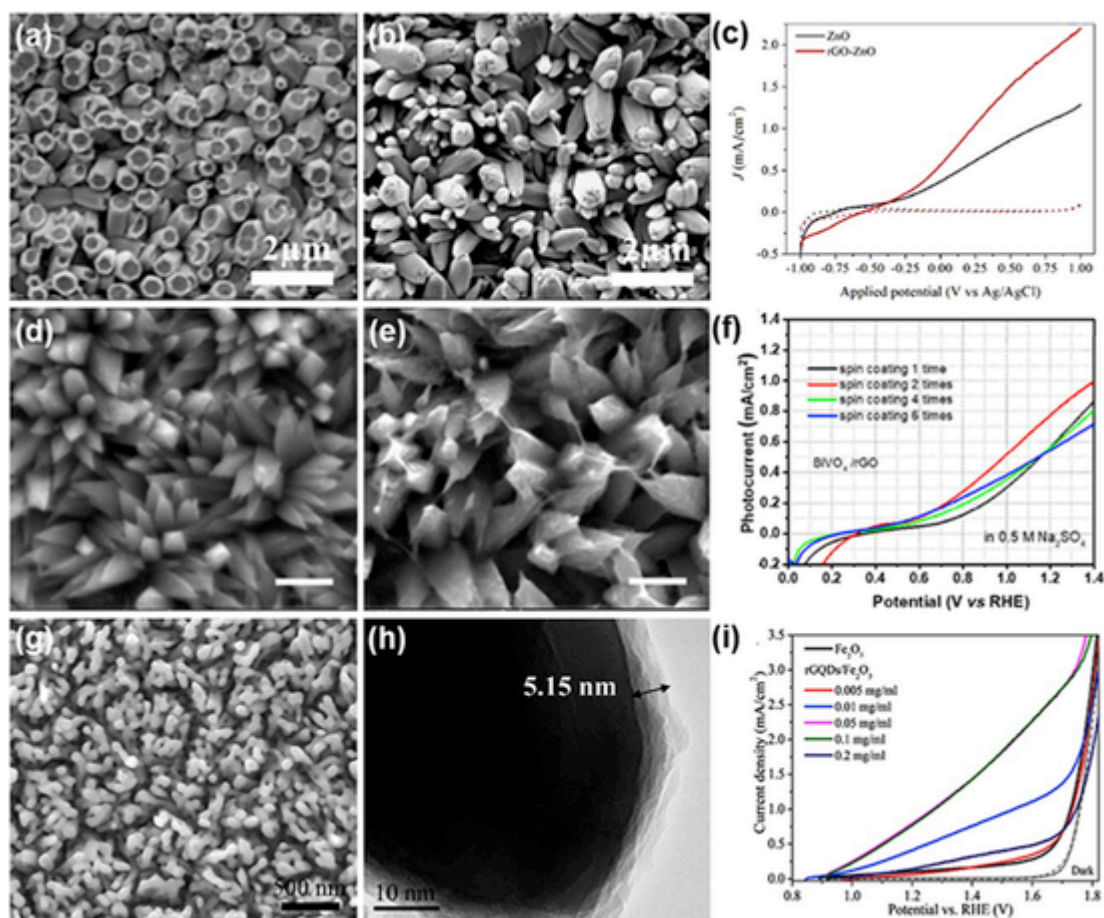


Fig. 15. SEM images of (a) ZnO, and (b) rGO/ZnO, (c) LSV curves of ZnO and rGO/ZnO. Reprinted with permission from Ref. [145]. SEM images of (d) BiVO₄, and (e) BiVO₄/rGO, (f) PCD curves of BiVO₄/rGO with different spin-coating times. Reprinted with permission from Ref. [149]. (g) Top-view SEM image of Fe₂O₃ nanostructured electrode, (h) TEM image of rGQD-modified Fe₂O₃, and (i) LSV curves of rGQDs/Fe₂O₃ electrodes with various amounts of rGQDs and bare Fe₂O₃ electrodes. Reprinted with permission from Ref. [150].

and charge-transfer kinetics. Ultralow density 3D g-CN nanosheets were prepared from a cyanuric acid–melamine supramolecular precursor; the nanosheets can easily stand on green bristle grass (inset of Fig. 17g). The surface area of these structures reached $1300 \text{ m}^2 \text{ g}^{-1}$, suggesting increased active sites available for reactions. Surface area enhancements are observed upon acid treatment of g-CN. However, the in-plane periodicity of aromatic rings is destroyed by acid protonation [170]. Thus, the supramolecular precursor used by Chen et al. including cyanuric acid yields 3D g-CN thin nanosheets with floppy agglomerates (Fig. 17g) and high surface areas. The band alignment diagram (Fig. 17h) shows that the bandgap increased with 3D structuring. The CB potential of 3D g-CN is more negative than the reduction potential of H^+/H_2 , while the VB potential is more positive than the oxidation potential of $\text{O}_2/\text{H}_2\text{O}$, thereby satisfying the thermodynamic requirements for water splitting. The quick rise in the photocurrent of 3D g-CN under illumination (see Fig. 17i) confirms its improved electron transport and extended charge-carrier lifetime. Similar efforts were reported by Mahzoon et al. [171] through the fabrication of a 1D–2D g-CN heterojunction via reacting protonated melamine in ethanol or water to obtain 1D and 2D structures, respectively. SEM imaging (Fig. 17j) revealed 1D fibrous structures coupled with 2D lamellae, thus demonstrating 1D–2D g-CN composition. The flat-band potentials of the 2D and 1D g-CN are -1.47 V and -1.37 V , respectively, vs. Ag/AgCl. Correspondingly, the VB edges for 2D and 1D g-CN are 1.26 and 1.51 eV. Therefore, the composite forms a type-II heterostructure (see Fig. 17k) between the 1D and 2D g-CN regions; electrons flow from the CB of the 2D structure to that of the 1D structure while holes flow from the VB of the 1D structure to that of the 2D g-CN. This heterojunction forma-

tion efficiently separates electrons and holes, yielding a higher photocurrent, as shown in the transient photocurrent curves in Fig. 17l.

The above discussion demonstrates that the bandgap, CB energy, and VB energy of g-CN can be altered by doping or acid treatment to both intensify the visible-light absorption capacity and affect the microstructure to enhance the surface area and reaction sites [160]. However, these efforts still provide lower PCD during PEC water splitting compared to materials discussed in prior sections. Thus, one can reasonably propose that problems like poor electronic conductivity and the rapid recombination of photogenerated carriers could be overcome by forming heterostructures of g-CN with other materials.

Sheets of g-CN have been combined with various semiconductors such as MoS₂ [176], CuO [177], Fe₂O₃ [173], FeVO₄ [172], SnO₂ [123], BiVO₄ [174], TiO₂ [178], and MnO₂ [30] to form heterostructure nanocomposites. The metal-free g-CN is environmentally safe and can be used with earth-abundant materials like FeVO₄, which has a bandgap energy of 2.06 eV [172]. The FeVO₄/g-CN composite film yielded a PCD of 0.5 mA cm^{-2} at $0.8 \text{ V}_{\text{SCE}}$, which is twice that shown by a FeVO₄ film alone (Fig. 18a). Based on the Mott–Schottky curves, the VB edge of g-CN is higher than that of FeVO₄. Thus, under illumination, photoexcited holes from FeVO₄ are transferred rapidly to the VB of g-CN to allow faster charge transfer, ultimately enhancing the PEC performance of FeVO₄. Similar VB positions were determined for the Fe₂O₃/metal-doped tubular C₃N₄ (t-CN) heterostructure nanocomposite reported by Arora et al. [173] The t-CN morphology arose from Co doping at a high annealing temperature of $700 \text{ }^\circ\text{C}$ under ambient N₂. Further, along with Co, Ni was also doped in t-CN and coated over sputter-deposited hematite films by a doctor blade process.

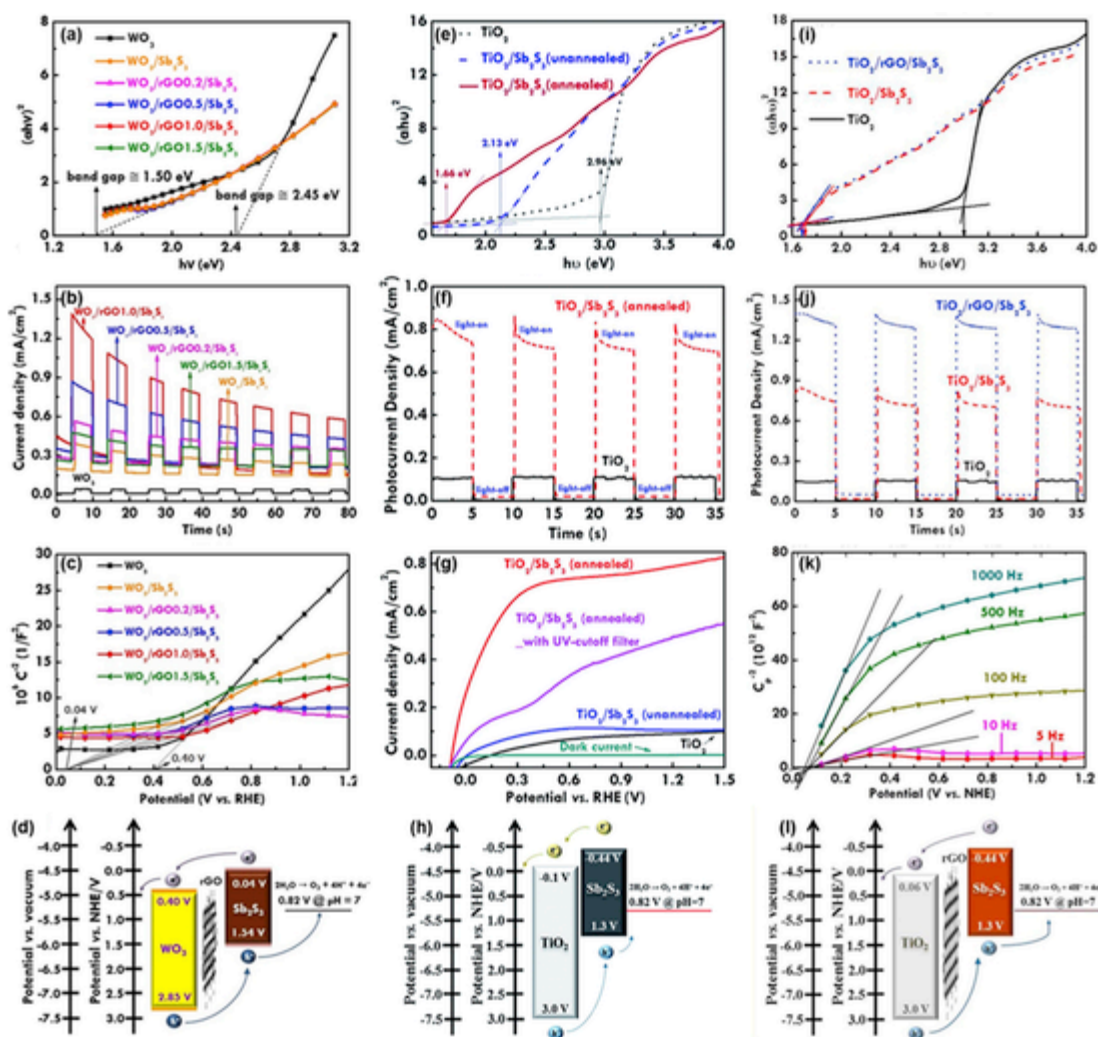


Fig. 16. (a) Tauc plots, (b) transient photocurrent decay, (c) Mott-Schottky plots, and (d) band positions for different WO_3 nanocomposites. Reprinted with permission from Refs. [155]. (e) Tauc plots, (f) transient photoresponse, (g) PCD, and (h) schematic of band energies and charge transfer for $\text{TiO}_2/\text{Sb}_2\text{S}_3$ nanocomposite. Reprinted with permission from Ref. [156]. (i) Tauc plots, (j) transient photocurrent for the $\text{TiO}_2/\text{rGO}/\text{Sb}_2\text{S}_3$ nanocomposite, (k) Mott-Schottky plot for the TiO_2 electrode measured at different frequencies, and (l) band energies and charge transfer for the $\text{TiO}_2/\text{rGO}/\text{Sb}_2\text{S}_3$ electrode under illumination. Reprinted with permission from Ref. [156].

This bimetallic-doped t-CN showed a bandgap of < 2 eV that promoted increased visible-light harvesting and the efficient separation of photogenerated charge carriers from Fe_2O_3 . Ultimately, the Co-Ni-doped t-CN/ Fe_2O_3 photoanode exhibited a PCD of 2.73 mA cm^{-2} at $1.23 V_{\text{RHE}}$ (Fig. 18b).

Ma et al. [173] used ultrathin layered g-CN as a co-catalyst with Bi_2MoO_6 nanosheets. The composite achieved a photocurrent 2.3 times higher than that of pristine Bi_2MoO_6 nanosheets (Fig. 18c). The formation of such a nanocomposite overcomes limitations of low carrier mobility, slow water oxidation kinetics on Bi_2MoO_6 , and recombination of photogenerated charge carriers in g-CN. The ultrathin g-CN layers over Bi_2MoO_6 nanosheets deliver synergetic interfacial contact to ensure smooth hole transfer from the VB of Bi_2MoO_6 to g-CN. The g-CN-based composites shown in Fig. 18a–c include type-II heterostructures between metal oxides and g-CN. Such heterostructures feature built-in electric fields at their interfaces that effectively separate the charges, as discussed in section 4. Conversely, the g-CN/ BiVO_4 nanocomposite reported by Safaei et al. [174] had a Z-scheme heterojunction that boosted the BiVO_4 performance by a factor of four. As noted earlier, the Z-scheme formation occurs when the CB of PS-1 is greater than the water reduction potential and the VB of PS-2 is less than the water oxidation potential. The chopped illumination curves of g-CN/ BiVO_4 are compared with the Z-scheme system of $\text{TiO}_2/\text{BiVO}_4$ (Fig. 18d),

which indicates that higher light absorption corresponds to a greater photocurrent. Similarly, Song et al. prepared a Z-scheme g-CN/ BiVO_4 using Ag NPs as electron shuttles, and Mo et al. observed Z-scheme formation in a $\text{MnO}_2/\text{g-CN}$ monolayer via Mn vacancies [30,179]. Wang et al. [175] fabricated type-II $\text{WO}_3/\text{g-CN}$ (Fig. 18e) and direct Z-scheme g-CN/ WO_3 (Fig. 18f) heterojunctions. Based on the position of the g-CN, the heterojunction scheme can change. However, the type-II heterojunction has a higher PCD (Fig. 18g) because it efficiently suppresses electron-hole recombination in WO_3 and g-CN; this is attributed to the formation of the built-in electric field from the difference in chemical potential, which yields a higher PCD. Meanwhile, when WO_3 is coated on g-CN to create mismatched CB and VB, the Z-scheme structure formation predominates, promoting water reduction and oxidation. The PCD in the Z-scheme heterostructure (Fig. 18h) is comparatively lower than that in the type-II heterostructure because of the slow reaction kinetics, which could be improved by using a passivation layer or a co-catalyst on the WO_3 surface. Another composite of $\text{TiO}_2/\text{g-CN}$ also showed type-II- and Z-scheme-based charge transfer depending on the flow of electrons. Electron flow from the CB of g-CN to that of TiO_2 resulted in the formation of the type-II mechanism [178–181]. The Z-scheme formed when electrons flowed from the CB of TiO_2 to the VB of g-CN [182,183]. With the $\text{SnO}_2/\text{g-CN}$ composite reported by Seza et al. [123], type-II heterostructure formation was observed with elec-

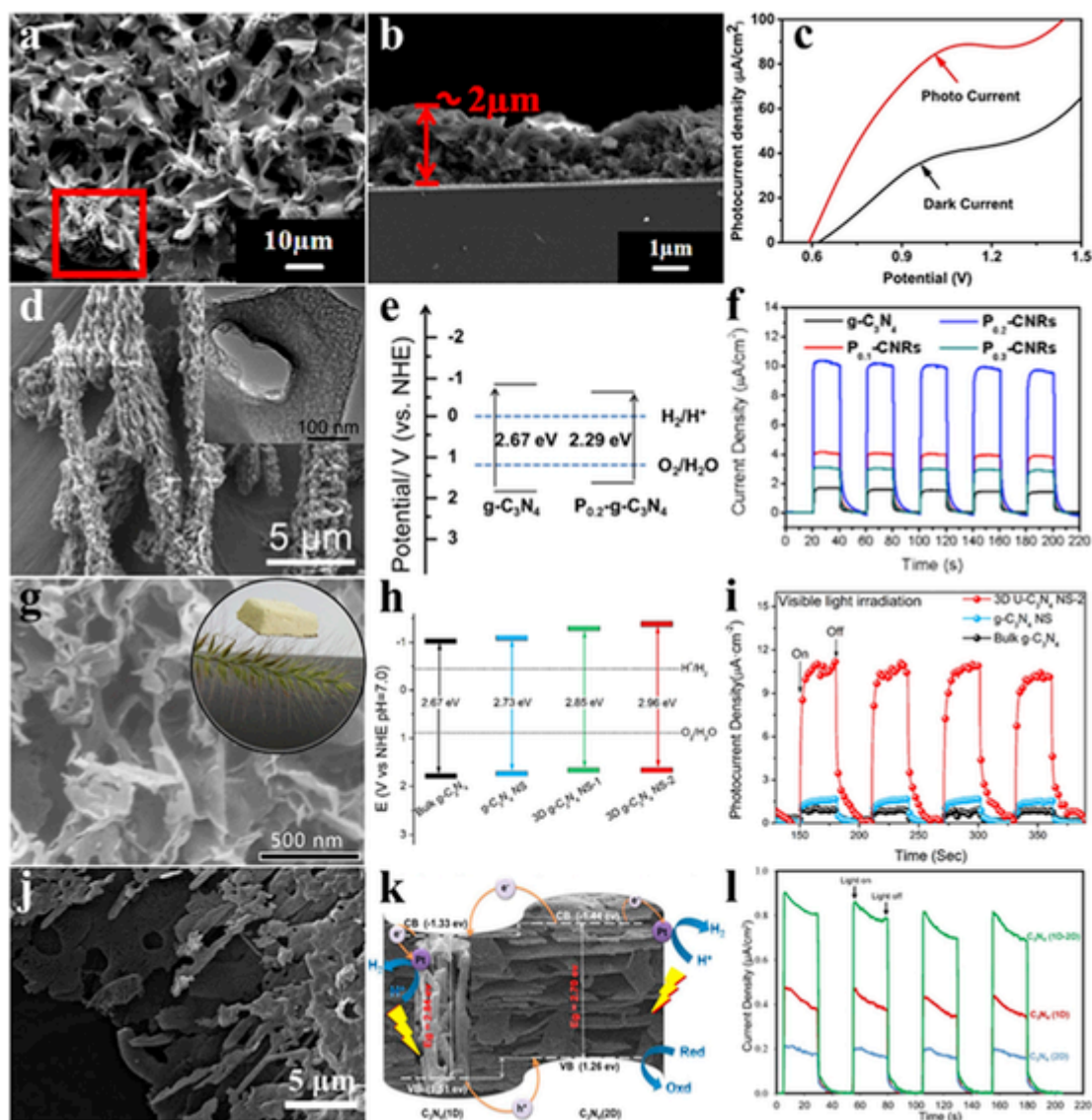


Fig. 17. (a) Top-view SEM image, (b) cross-sectional SEM image, and (c) photo- and dark-current density–potential curves of the framework g-CN film. Reprinted with permission from Ref. [168]. (d) SEM image of P-CNR; inset is a high-magnification TEM image, (e) band structure alignments, and (f) photocurrent responses of g-CN and different P-CNRs under visible-light irradiation. Reprinted with permission from Ref. [168]. (g) SEM image (inset image illustrating low density), (h) band diagram, and (i) transient PCD of 3D g-CN. Reprinted with permission from Ref. [169]. (j) SEM image, (k) schematic showing charge transfer and separation, and (l) transient photocurrent responses of 1D–2D g-CN. Reprinted with permission from Ref. [171].

trons flowing from the CB of g-CN to that of SnO₂, yielding a PCD of 33 μA cm⁻² at 0.5 V_{Ag/AgCl}. On the other hand, the presence of oxygen vacancies in the SnO_x/g-CN composite induced a PCD of 40 μA cm⁻² at 0.5 V_{Ag/AgCl}. Here, the Z-scheme formation occurred by electron flow from the CB of SnO_x to the VB of g-CN [122]. Xiao et al. [183] also demonstrated an enhanced PCD for the oxygen-deficient (OV) composite of 0D/1D g-CN/OV-TiO₂ via the Z-scheme mechanism. Thus, g-CN can show either type-II or Z-scheme heterostructure behavior, making it a highly promising photoelectrode material for PEC water splitting. Photoelectrochemical water splitting properties of several g-CN based composites are compared in Table 4c. All possible values of applied bias with respect to various reference electrodes were converted to reversible hydrogen electrode (RHE) in all tables by using widely available formulae [184,185].

A schematic summary of the roles of CNT, graphene, and g-CN in composites with TiO₂ is given in Fig. 19. Based on the PCD results, one can infer that CNT, graphene, and g-CN significantly enhance the photocurrents of these composite materials. CNT and graphene provide pathways for electron transfer and increase the light absorption capac-

ity of the nanocomposites. Meanwhile, g-CN becomes aligned with metal oxides to form heterostructures, with electron flow relying on the resultant band-bending. Furthermore, the use of nanotube- or nanosheet-like morphology supports the reduction of charge carrier diffusion distances.

6. Conclusions and future perspectives

The Web of Science indicates that 3000 research papers on PEC water-splitting have been published from 2016 to the present, and Google Scholar suggests a total at least 3 times higher. Nonetheless, the numerous materials and combinations thereof that have been studied still provide PCD and/or efficiency well below theoretical limits and practical requirements. However, the number of reports indicates the intense level of interest in the development of new materials, composites, and approaches to photoelectrode design. In part because of the rapid pace of growth of the literature, correlations of existing reports with new experiments are somewhat lacking. In addition, some materials such as WO₃ nanoflowers and WO₃ nanoflakes/CuO obtained hydrothermally have been reported by multiple groups without PCD enhancements. In-

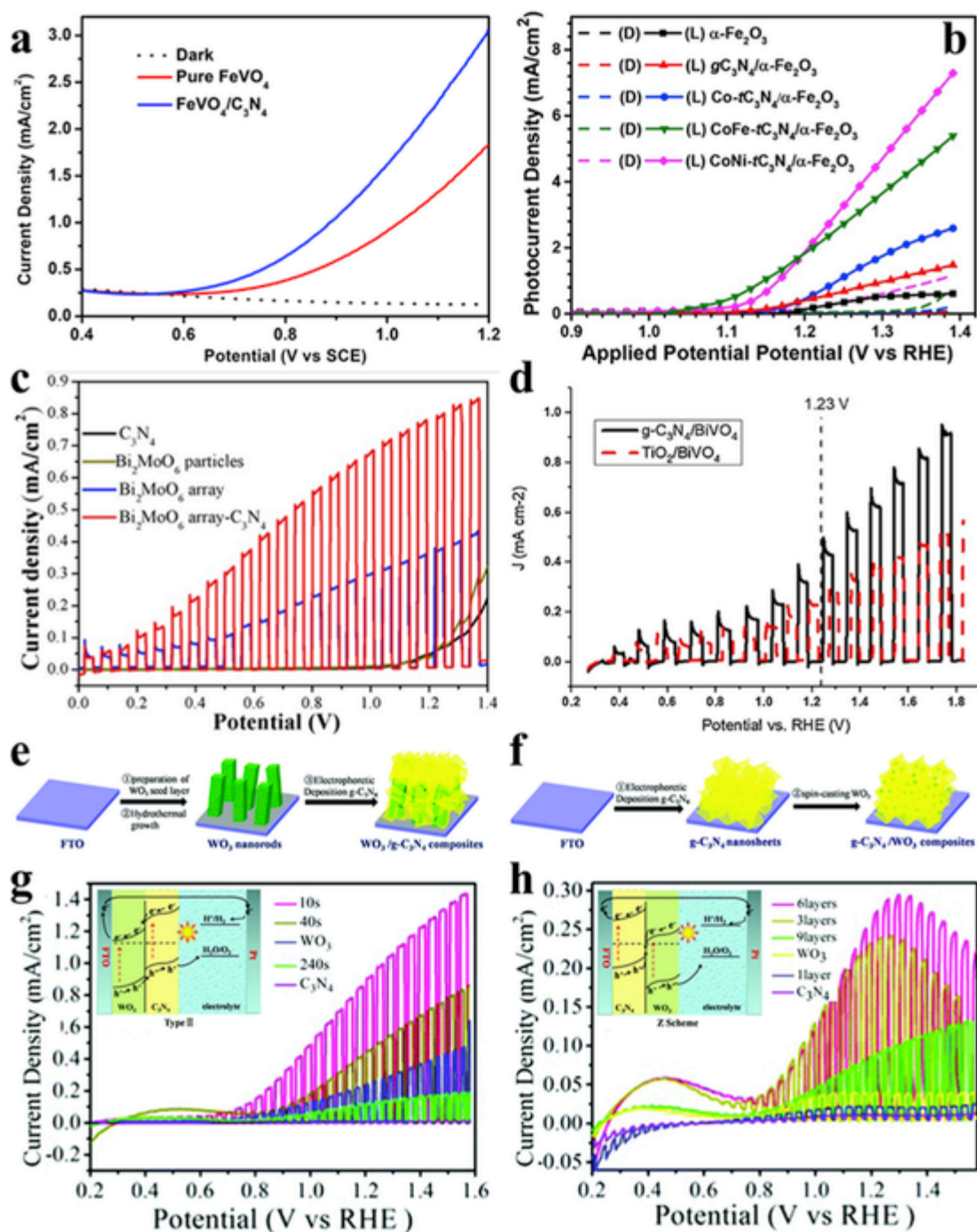


Fig. 18. (a) LSV of FeVO₄ and FeVO₄/g-CN. Reprinted with permission from Ref. [172]. (b) PCD-applied potential (V vs. RHE) curves of pristine α -Fe₂O₃ and layers of g-CN, Co-tubular CN(Co-t-CN), Co-Fe-t-CN, and Co-Ni-t-CN-coated α -Fe₂O₃ thin films. Reprinted with permission from Ref. [173]. (c) Chopped LSV scans of Bi₂MoO₆/g-CN. Reprinted with permission from Ref. [173]. (d) LSV of g-CN/BiVO₄ and TiO₂/BiVO₄ heterojunction photoanodes under chopped illumination. Reprinted with permission from Refs. [174]. (e) Type-II g-CN/WO₃ and (f) Z-scheme WO₃/g-CN nanocomposite fabrication schemes and photocurrent responses (inset: charge separation and transfer) for (g) type-II and (h) Z-scheme composites. Adapted with permission from Ref. [175].

deed, sometimes the PCD values in duplicate reports are much lower than those in earlier research. Therefore, researchers should aim to systematically improve PCD values by the kinds of morphology engineering and surface modification techniques reviewed here. Many studies fail to focus on the parameters necessary for PEC water-splitting. In the exploration of photoelectrode materials, parameters such as the thickness, absorbance, and reflectance of the electrode, open-circuit potential, and transient responses should be reported, along with the PCD, biasing potential, stability, and efficiency.

Considering the available strategies for achieving efficient solar water-splitting, morphology engineering offers reduction of diffusion length, which facilitates photogenerated carrier transport to reactive sites. Nanostructuring also provides greater electrode-electrolyte interfacial area for reaction. However, care should be taken to limit the height and thickness of nanostructures to ensure that carriers can also reach the substrate and the external circuit. Certain nanostructures, such as 3D branched morphology, can achieve higher light-harvesting capabilities than others.

Table 4c
Overview of g-CN-based nanocomposite materials.

Materials	Nanostructures	Electrolyte	PCD [$\text{mA}\cdot\text{cm}^{-2}$]	V vs. RHE [V]	Ref.
ITO/MoS ₂ /S/g-C ₃ N ₄	Chemical synthesis/hydrothermal	0.1 M Na ₂ SO ₄	0.12^a@0.5V	0.7	[176]
ITO/MoS ₂ /g-C ₃ N ₄ /rGO	Chemical synthesis/hydrothermal	0.5 M H ₂ SO ₄	1^b@0.4V	0.4	[211]
FTO/Cu ₂ MoS ₄ /g-C ₃ N ₄	Chemical synthesis/hydrothermal	0.1 M Na ₂ SO ₄	0.0027^a		[212]
FTO/WO ₃ /g-C ₃ N ₄	Hydrothermal/electrophoretic deposition	0.5 M Na ₂ SO ₄	0.82^b@1.23V	1.23	[175]
FTO/Bi ₂ MoO ₆ /g-C ₃ N ₄	Hydrothermal/dip coating	0.1 M Na ₂ SO ₄	0.52^c@0.8V	1.04	[173]
FTO/BiPO ₄ /Bi ₂ O ₃ /g-C ₃ N ₄	Hydrothermal/dropcasting	0.1 M Na ₂ SO ₄	0.095^a@1.25V	1.45	[213]
FTO/BiVO ₄ /g-C ₃ N ₄	Chemical synthesis/electrodeposition	0.5 M Na ₂ SO ₄	0.42^b@1.23V	1.23	[174]
FTO/g-C ₃ N ₄ /Ag/BiVO ₄	Chemical synthesis/spin coating	0.2 M Na ₂ SO ₄	0.0015^a		[179]
FTO/BiVO ₄ /PDA/g-C ₃ N ₄	Chemical synthesis	0.5 M Na ₂ SO ₄	0.003^c		[214]
FTO/SnOx/g-C ₃ N ₄	Chemical synthesis	0.2 M Na ₂ SO ₄	0.048^a@0.6V	0.8	[122]
FTO/g-C ₃ N ₄ /SnO ₂	Chemical synthesis	0.2 M Na ₂ SO ₄	0.033^a@0.5V	0.7	[123]
FTO/FeVO ₄ /g-C ₃ N ₄	Chemical synthesis	0.1 M Na ₂ SO ₄	0.5^c@0.8V	1.04	[172]
FTO/Fe ₂ O ₃ /Co-Ni/g-C ₃ N ₄	Sputtering/dropcasting	1 M NaOH	2.73^b@1.23V	1.23	[173]
FTO/Cu ₂ O/g-C ₃ N ₄	Electrodeposition/Electrophoretic	0.1 M NaNO ₃	-1.38^a@-0.4V	-0.2	[215]
FTO/CuO/g-C ₃ N ₄ /CuI	Chemical synthesis/dropcasting	Phosphate Buffer	-0.35^b@0.4V	0.4	[177]
Ti/OV-TiO ₂ /g-C ₃ N ₄	Anodization/CVD	0.1 M Na ₂ SO ₄	0.72^b@1.23V	1.23	[183]
FTO/TiO ₂ /g-C ₃ N ₄	Chemical synthesis/dropcasting	0.1 M Na ₂ SO ₄	0.040@0.6V	0.84	[179]
Ti/TiO ₂ /g-C ₃ N ₄	Electrochemical/thermal treatment	0.1 M Na ₂ SO ₄	0.82^b@1.23V	1.23	[181]
ITO/C-TiO ₂ /g-C ₃ N ₄	Hydrothermal/thermal polycondensation	0.1 M Na ₂ SO ₄	0.035^c		[180]
FTO/NiTiO ₃ /g-C ₃ N ₄	Sol-gel/thermal polycondensation	0.1 M Na ₂ SO ₄	0.38^a@0.8V	1	[180]
FTO/TiO ₂ /g-CN	Hydrothermal/solvothermal	0.2 M Na ₂ SO ₄	0.089^c@0.6 V	0.84	[178]
ITO/MnO ₂ /g-C ₃ N ₄	Chemical synthesis/drop casting	Phosphate Buffer	0.004^c@- 0.2 V	0.04	[30]

Nanostructured photoelectrodes can still yield poor performance depending on the electrical conductivity of the materials. The performance of such structures can be elevated using conductive carbons like CNT, graphene, or g-CN, which efficiently transfer charge carriers to separate sides of the structure. Thus, nanocomposites with conductive carbons are an alternative strategy for electrode preparation. However, for the effective use of conductive carbons, especially CNT and graphene, the carbons should be used as scaffolds with good dispersion in the photoelectrode, rather than as separate layers. Scaffolding can enhance the light absorption and the effective transfer of photogenerated electrons. With g-CN, its utility in both type-II and Z-scheme heterostructures permits morphological tuning via its nanostructure while maintaining superior PEC performance. The heterostructure formed in this case leads to the development of a built-in electric field that reduces electron-hole recombination. However, the position of g-CN in the heterostructure controls its PEC performance depending on the band bending that occurs upon heterostructure formation. In addition, heterojunctions can be formed with plasmonic noble metals like

Ag, Au, and Pt, co-catalyst layers like Co-Pi, or passivation layers such as TiO₂ and ZnO. Overall, heterojunctions are necessary to drive charge-carrier separation, although limitations related to the interfacial connection between two semiconductors must be overcome.

Declaration of competing interest

The authors declare that they have no known competing financial interests or personal relationships that could have appeared to influence the work reported in this paper.

Acknowledgement

This research was supported by the Technology Development Program to Solve Climate Changes of the National Research Foundation (NRF) funded by the Ministry of Science, ICT & Future Planning (NRF-2016M1A2A2936760) and NRF-2013R1A5A1073861.

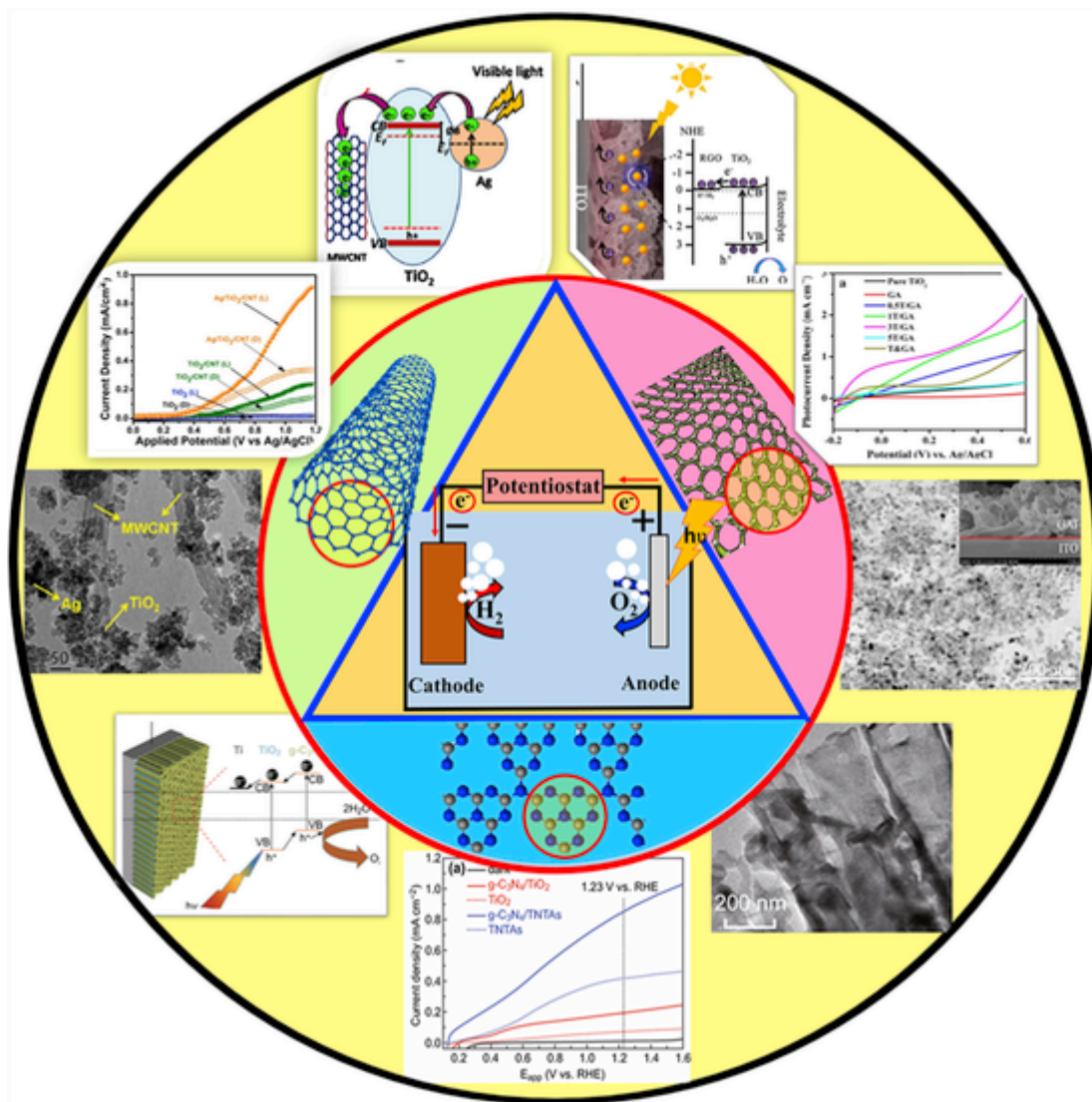


Fig. 19. Comparison of structures, mechanisms, morphologies, and PCD measurements of different TiO_2 nanocomposites using CNT, rGO, and g-CN. Adapted with permission from Refs. [119,147,181].

References

- [1] M. Zhu, Z. Sun, M. Fujitsuka, T. Majima, *Angew. Chem. Int. Ed.* 57 (2018) 2160–2164.
- [2] M. Antuch, P. Millet, A. Iwase, A. Kudo, *Appl. Catal. B Environ.* 237 (2018) 401–408.
- [3] D. Lee, A. Kvit, K.-S. Choi, *Chem. Mater.* 30 (2018) 4704–4712.
- [4] J. Jian, G. Jiang, R. van de Krol, B. Wei, H. Wang, *Nano Energy* 51 (2018) 457–480.
- [5] B. Johnston, M.C. Mayo, A. Khare, *Technovation* 25 (2005) 569–585.
- [6] The Energy and Fuel Data Sheet, 2011, <http://www.claverton-energy.com/wordpress/wp-content/uploads/2012/08/the-energy-and-fuel-data-sheet1.pdf>.
- [7] www.energy.gov/eere/fuelcells/doe-technical-targets-hydrogen-production-photoelectrochemical-water-splitting
- [8] A. Fujishima, K. Honda, *Nature* 238 (1972) 37.
- [9] M. Zhou, Z. Liu, X. Li, Z. Liu, *Ind. Eng. Chem. Res.* 57 (2018) 6210–6217.
- [10] C. Chang, H.-C. Yang, N. Gao, S.-Y. Lü, *J. Alloys Compd.* 738 (2018) 138–144.
- [11] G. Dong, H. Hu, L. Wang, Y. Zhang, Y. Bi, *J. Catal.* 366 (2018) 258–265.
- [12] J. Hu, D. Chen, Z. Mo, N. Li, Q. Xu, H. Li, J. He, H. Xu, J. Lu, *Angew. Chem.* 131 (2019) 2095–2099.
- [13] D. Cardenas-Morcoso, R. Ibraimov, M. García-Tecedor, I. Liberman, S. Gimenez, I. Hod, *J. Mater. Chem. A* 7 (2019) 11143–11149.
- [14] C. Wu, J. Zhong, J. Xie, D. Wang, Y. Shi, Q. Chen, H. Yan, J. Zhu, *Appl. Surf. Sci.* 484 (2019) 112–123.
- [15] W.-H. Cheng, M.H. Richter, M.M. May, J. Ohlmann, D. Lackner, F. Dimroth, T. Hannappel, H.A. Atwater, H.-J. Lewerenz, *ACS Energy Lett.* 3 (2018) 1795–1800.
- [16] C. Hu, X. Chen, Q. Dai, M. Wang, L. Qu, L. Dai, *Nano Energy* 41 (2017) 367–376.
- [17] Y. Wang, Q. Wang, X. Zhan, F. Wang, M. Safdar, J. He, *Nanoscale* 5 (2013) 8326–8339.
- [18] J. Joy, J. Mathew, S.C. George, *Int. J. Hydrogen Energy* 43 (2018) 4804–4817.
- [19] S. Choudhary, S. Upadhyay, P. Kumar, N. Singh, V.R. Satsangi, R. Shrivastav, S. Dass, *Int. J. Hydrogen Energy* 37 (2012) 18713–18730.
- [20] G. Wang, Y. Ling, H. Wang, L. Xihong, Y. Li, *J. Photochem. Photobiol. C Photochem. Rev.* 19 (2014) 35–51.
- [21] J.H. Kim, D. Hansora, P. Sharma, J.-W. Jang, J.S. Lee, *Chem. Soc. Rev.* 48 (2019) 1908–1971.
- [22] S.S. Kalanur, L.T. Duy, H. Seo, *Top. Catal.* 61 (2018) 1043–1076.
- [23] S.K. Saraswat, D.D. Rodene, R.B. Gupta, *Renew. Sustain. Energy Rev.* 89 (2018) 228–248.
- [24] M. Zare, S. Solaymani, A. Shafiekhani, S. Kulesza, Ş. Tãlu, M. Bramowicz, *Sci. Rep.* 8 (2018) 10870.
- [25] L.K. Putri, W.-J. Ong, W.S. Chang, S.-P. Chai, *Appl. Surf. Sci.* 358 (2015) 2–14.
- [26] X. Wang, Y. Zheng, J. Yuan, J. Shen, A. Wang, L. Niu, S. Huang, *Electrochim. Acta* 212 (2016) 890–897.
- [27] R.A.J. Gurudayal, P.P. Boix, C. Yi, C. Shi, M.C. Scott, S.A. Veldhuis, A.M. Minor, S.M. Zakeeruddin, L.H. Wong, M. Grätzel, N. Mathews, *ChemSusChem* 10 (2017) 2449–2456.
- [28] A. Martinez-Garcia, H.B. Russell, W. Paxton, S. Ravipati, S. Calero-Barney, M. Menon, E. Richter, J. Young, T. Deutsch, M.K. Sunkara, *Adv. Energy Mater.* 8 (2018) 1703247.
- [29] Z. Bai, X. Yan, Y. Li, Z. Kang, S. Cao, Y. Zhang, *Adv. Energy Mater.* 6 (2016) 1501459.
- [30] Z. Mo, H. Xu, Z. Chen, X. She, Y. Song, J. Lian, X. Zhu, P. Yan, Y. Lei, S. Yuan, H. Li, *Appl. Catal. B Environ.* 241 (2019) 452–460.
- [31] S. Allami, Z.D. Abid Ali, Y. Li, H. Hamody, B.H. Jawad, L. Liu, T. Li, *Heliyon* 3 (2017) e00423.

- [32] A. Sreedhar, I.N. Reddy, Q.T. Hoai Ta, G. Namgung, E. Cho, J.-S. Noh, *Ceram. Int.* 45 (2019) 6985–6993.
- [33] K. Govatsi, A. Seferlis, S.G. Neophytides, S.N. Yannopoulos, *Int. J. Hydrogen Energy* 43 (2018) 4866–4879.
- [34] C. Zhu, C. Li, M. Zheng, J.-J. Delaunay, *ACS Appl. Mater. Interfaces* 7 (2015) 22355–22363.
- [35] L. Wang, L. Xia, Y. Wu, Y. Tian, *ACS Sustain. Chem. Eng.* 4 (2016) 2606–2614.
- [36] Z. Zhang, B. He, L. Chen, H. Wang, R. Wang, L. Zhao, Y. Gong, *ACS Appl. Mater. Interfaces* 10 (2018) 38032–38041.
- [37] X. Xu, Z. Bao, W. Tang, H. Wu, J. Pan, J. Hu, H. Zeng, *Carbon* 121 (2017) 201–208.
- [38] C.X. Guo, J. Xie, H. Yang, C.M. Li, *Adv. Sci.* 2 (2015) 1500135.
- [39] S. Fu, B. Zhang, H. Hu, Y. Zhang, Y. Bi, *Catal. Sci. Technol.* 8 (2018) 2789–2793.
- [40] B. Jin, D. Wang, C. Feng, Y. Bi, Z. Jiao, *Catal. Lett.* 146 (2016) 1348–1354.
- [41] M. Chandra, K. Bhunia, D. Pradhan, *Inorg. Chem.* 57 (2018) 4524–4533.
- [42] X. Yu, Z. Zhao, N. Ren, J. Liu, D. Sun, L. Ding, H. Liu, *ACS Sustain. Chem. Eng.* 6 (2018) 11775–11782.
- [43] Y.-Q. Rong, X.-F. Yang, W.-D. Zhang, Y.-X. Yu, *Mater. Lett.* 246 (2019) 161–164.
- [44] X. Ren, A. Sangle, S. Zhang, S. Yuan, Y. Zhao, L. Shi, R.L.Z. Hoye, S. Cho, D. Li, J.L. MacManus-Driscoll, *J. Mater. Chem. A* 4 (2016) 10203–10211.
- [45] A. Liao, H. He, L. Tang, Y. Li, J. Zhang, J. Chen, L. Chen, C. Zhang, Y. Zhou, Z. Zou, *ACS Appl. Mater. Interfaces* 10 (2018) 10141–10146.
- [46] H. Seok Jo, E. Samuel, H.-J. Kwon, B. Joshi, M.-W. Kim, T.-G. Kim, M.T. Swihart, S.S. Yoon, *Chem. Eng. J.* 363 (2019) 13–22.
- [47] Y. Gu, W. Zheng, Y. Bu, *J. Electroanal. Chem.* 833 (2019) 54–62.
- [48] C. Wang, J. Tang, X. Zhang, L. Qian, H. Yang, *Prog. Nat. Sci.: Mater. Int.* 28 (2018) 200–204.
- [49] J. Park, P.R. Deshmukh, Y. Sohn, W.G. Shin, *J. Alloys Compd.* 787 (2019) 1310–1319.
- [50] W. Ye, F. Chen, F. Zhao, N. Han, Y. Li, *ACS Appl. Mater. Interfaces* 8 (2016) 9211–9217.
- [51] J. Huang, Y. Zhang, Y. Ding, *ACS Catal.* 7 (2017) 1841–1845.
- [52] J.G. Lee, D.-Y. Kim, J.-H. Lee, M. Kim, S. An, H.S. Jo, C. Nervi, S.S. Al-Deyab, M.T. Swihart, S.S. Yoon, *ACS Appl. Mater. Interfaces* 8 (2016) 15406–15414.
- [53] M. Kim, B. Joshi, H. Yoon, T.Y. Ohm, K. Kim, S.S. Al-Deyab, S.S. Yoon, *J. Alloys Compd.* 708 (2017) 444–450.
- [54] J. Zhou, S. Lin, Y. Chen, A.M. Gaskov, *Appl. Surf. Sci.* 403 (2017) 274–281.
- [55] Y. Fang, W.C. Lee, G.E. Canciani, T.C. Draper, Z.F. Al-Bawi, J.S. Bedi, C.C. Perry, *Q. Chem. Mater. Sci. Eng., B* 202 (2015) 39–45.
- [56] R. Sánchez-Tovar, R.M. Fernández-Domene, D.M. García-García, J. García-Antón, *J. Power Sources* 286 (2015) 224–231.
- [57] J. Li, X. Jin, R. Li, Y. Zhao, X. Wang, X. Liu, H. Jiao, *Appl. Catal. B Environ.* 240 (2019) 1–8.
- [58] M. Meng, X. Wu, X. Zhu, X. Zhu, P.K. Chu, *ACS Appl. Mater. Interfaces* 6 (2014) 4081–4088.
- [59] A. Cao, L. Zhang, Y. Wang, H. Zhao, H. Deng, X. Liu, Z. Lin, X. Su, F. Yue, *ACS Sustain. Chem. Eng.* 7 (2019) 2492–2499.
- [60] J. Yang, C. Li, P. Diao, *Electrochim. Acta* 308 (2019) 195–205.
- [61] Z. Lin, C. Du, B. Yan, G. Yang, *J. Catal.* 372 (2019) 299–310.
- [62] A.A.M. Ibrahim, I. Khan, N. Iqbal, A. Qurashi, *Int. J. Hydrogen Energy* 42 (2017) 3423–3430.
- [63] C. Liu, J. Su, J. Zhou, L. Guo, *ACS Sustain. Chem. Eng.* 4 (2016) 4492–4497.
- [64] P. Chakthranont, T.R. Hellstern, J.M. McEnaney, T.F. Jaramillo, *Adv. Energy Mater.* 7 (2017) 1701515.
- [65] S.S. Patil, M.G. Mali, M.A. Hassan, D.R. Patil, S.S. Kolekar, S.-W. Ryu, *Sci. Rep.* 7 (2017) 8404.
- [66] H. Yoon, M.G. Mali, J.Y. Choi, M. Kim, S.K. Choi, H. Park, S.S. Al-Deyab, M.T. Swihart, A.L. Yarin, S.S. Yoon, *Langmuir* 31 (2015) 3727–3737.
- [67] P.R. Narangari, S.K. Karuturi, M. Lysevych, H. Hoe Tan, C. Jagadish, *Nanotechnology* 28 (2017) 154001.
- [68] M.-W. Kim, E. Samuel, K. Kim, H. Yoon, B. Joshi, M.T. Swihart, S.S. Yoon, *J. Alloys Compd.* 769 (2018) 193–200.
- [69] B. Zhou, X. Kong, S. Vanka, S. Chu, P. Ghamari, Y. Wang, N. Pant, I. Shih, H. Guo, *Z. Mi, Nat. Commun.* 9 (2018) 3856.
- [70] S. Wang, P. Chen, Y. Bai, J.-H. Yun, G. Liu, L. Wang, *Adv. Mater.* 30 (2018) 1800486.
- [71] M.-W. Kim, K. Kim, T.Y. Ohm, H. Yoon, B. Joshi, E. Samuel, M.T. Swihart, S.K. Choi, H. Park, S.S. Yoon, *Chem. Eng. J.* 333 (2018) 721–729.
- [72] X. Lv, X. Xiao, M. Cao, Y. Bu, C. Wang, M. Wang, Y. Shen, *Appl. Surf. Sci.* 439 (2018) 1065–1071.
- [73] L. Li, X. She, J. Yi, L. Pan, K. Xia, W. Wei, X. Zhu, Z. Chen, H. Xu, H. Li, *Appl. Surf. Sci.* 469 (2019) 933–940.
- [74] J. Zhang, G. Zhang, J. Zhang, *Appl. Surf. Sci.* 475 (2019) 256–263.
- [75] B. Joshi, H. Yoon, H. Kim, M. Kim, M.G. Mali, S.S. Al-Deyab, S.S. Yoon, *RSC Adv.* 5 (2015) 85323–85328.
- [76] R.W. Johnson, A. Hultqvist, S.F. Bent, *Mater. Today* 17 (2014) 236–246.
- [77] W. Dong, H. Li, J. Xi, J. Mu, Y. Huang, Z. Ji, X. Wu, *J. Alloys Compd.* 724 (2017) 280–286.
- [78] J. Long, W. Wang, S. Fu, L. Liu, *J. Colloid Interface Sci.* 536 (2019) 408–413.
- [79] S. Singh, N. Khare, *Nano Energy* 42 (2017) 173–180.
- [80] R. Lin, H. Lei, D. Ruan, K. Jiang, X. Yu, Z. Wang, W. Mai, H. Yan, *Nano Energy* 56 (2019) 82–91.
- [81] Q. Wu, J. Guo, R. Sun, J. Guo, S. Jia, Y. Li, J. Wang, J. Min, *Nano Energy* 61 (2019) 559–566.
- [82] P. Tyagi, C. Ramesh, J. Kaswan, S. Dhua, S. John, A.K. Shukla, S.C. Roy, S.S. Kushvaha, S.K. Muthusamy, *J. Alloys Compd.* 805 (2019) 97–103.
- [83] L.T. Quynh, C.N. Van, W.Y. Tzeng, C.-W. Huang, Y.-H. Lai, J.-W. Chen, K.-A. Tsai, C.L. Wu, W.-W. Wu, C.W. Luo, Y.-J. Hsu, Y.-H. Chu, *ACS Appl. Energy Mater.* 1 (2018) 3900–3907.
- [84] K.T. VanSant, J. Simon, J.F. Geisz, E.L. Warren, K.L. Schulte, A.J. Ptak, M.S. Young, M. Rienäcker, H. Schulte-Huxel, R. Peibst, A.C. Tamboli, *ACS Appl. Energy Mater.* 2 (2019) 2375–2380.
- [85] X. Zhang, X. Wang, D. Wang, J. Ye, *ACS Appl. Mater. Interfaces* 11 (2019) 5623–5631.
- [86] C. Mahala, M.D. Sharma, M. Basu, *New J. Chem.* 43 (2019) 7001–7010.
- [87] Y. Wang, W. Tian, L. Chen, F. Cao, J. Guo, L. Li, *ACS Appl. Mater. Interfaces* 9 (2017) 40235–40243.
- [88] F. Zhang, Y. Chen, W. Zhou, C. Ren, H. Gao, G. Tian, *ACS Appl. Mater. Interfaces* 11 (2019) 9093–9101.
- [89] M.G. Mali, H. Yoon, M. Kim, M.T. Swihart, S.S. Al-Deyab, S.S. Yoon, *Appl. Phys. Lett.* 106 (2015) 151603.
- [90] S. Xu, D. Fu, K. Song, L. Wang, Z. Yang, W. Yang, H. Hou, *Chem. Eng. J.* 349 (2018) 368–375.
- [91] X. Xia, M. Song, H. Wang, X. Zhang, N. Sui, Q. Zhang, V.L. Colvin, W.W. Yu, *Nanoscale* (2019).
- [92] T. Di, Q. Xu, W. Ho, H. Tang, Q. Xiang, J. Yu, *ChemCatChem* 11 (2019) 1394–1411.
- [93] C.-H. Li, C.-W. Hsu, S.-Y. Lu, *J. Colloid Interface Sci.* 521 (2018) 216–225.
- [94] J. Zhao, P. Zhang, J. Fan, J. Hu, G. Shao, *Appl. Surf. Sci.* 430 (2018) 466–474.
- [95] C. Liu, J. Tang, H.M. Chen, B. Liu, P. Yang, *Nano Lett.* 13 (2013) 2989–2992.
- [96] W. Zhang, H. Chen, L. Zhang, P. Zhang, E. Dong, J. Ma, G. Wang, *J. Alloys Compd.* 773 (2019) 597–604.
- [97] J. Yang, D. Wang, H. Han, C. Li, *Acc. Chem. Res.* 46 (2013) 1900–1909.
- [98] X. Li, J. Yu, J. Low, Y. Fang, J. Xiao, X. Chen, *J. Mater. Chem. A* 3 (2015) 2485–2534.
- [99] B. Peng, M. Xia, C. Li, C. Yue, P. Diao, *Catalysts* 8 (2018).
- [100] P. Subramanyam, T. Vinodkumar, M. Deepa, C. Subramanyam, *J. Mater. Chem. C* 7 (2019) 6398–6405.
- [101] A. Dutta, A. Naldoni, F. Malara, A.O. Govorov, V.M. Shalaev, A. Boltasheva, *Faraaday Discuss* 214 (2019) 283–295.
- [102] Y. Hu, Y. Wu, J. Feng, H. Huang, C. Zhang, Q. Qian, T. Fang, J. Xu, P. Wang, Z. Li, Z. Zou, *J. Mater. Chem. A* 6 (2018) 2568–2576.
- [103] J. Li, S.K. Cushing, P. Zheng, F. Meng, D. Chu, N. Wu, *Nat. Commun.* 4 (2013) 2651.
- [104] Z. Zheng, W. Xie, B. Huang, Y. Dai, *Chem. Eur. J.* 24 (2018) 18322–18333.
- [105] R. Boppella, S.T. Kochuveedu, H. Kim, M.J. Jeong, F. Marques Mota, J.H. Park, D.H. Kim, *ACS Appl. Mater. Interfaces* 9 (2017) 7075–7083.
- [106] Z. Xu, Z. Fan, Z. Shi, M. Li, J. Feng, L. Pei, C. Zhou, J. Zhou, L. Yang, W. Li, G. Xu, S. Yan, Z. Zou, *ChemSusChem* 11 (2018) 237–244.
- [107] A. Verma, A. Srivastav, S.A. Khan, V. Rani Satsangi, R. Shrivastav, D. Kumar Avasthi, S. Dass, *Phys. Chem. Chem. Phys.* 19 (2017) 15039–15049.
- [108] H. Kaneko, T. Minegishi, K. Domen, *Chem. Eur. J.* 24 (2018) 5697–5706.
- [109] M. Kim, H. Yoon, T.Y. Ohm, H.S. Jo, S. An, S.K. Choi, H. Park, S.S. Al-Deyab, B.K. Min, M.T. Swihart, S.S. Yoon, *Appl. Catal. B Environ.* 201 (2017) 479–485.
- [110] T.-G. Kim, B. Joshi, C.-W. Park, E. Samuel, M.-W. Kim, M.T. Swihart, S.S. Yoon, *J. Alloys Compd.* 798 (2019) 35–44.
- [111] A. Ghobadi, T.G.U. Ghobadi, F. Karadas, E. Ozbay, *Sci. Rep.* 8 (2018) 16322.
- [112] Y.-F. Xu, H.-S. Rao, B.-X. Chen, Y. Lin, H.-Y. Chen, D.-B. Kuang, C.-Y. Su, *Adv. Sci.* 2 (2015) 1500049.
- [113] J.S. Kim, S.K. Baek, Y.B. Kim, H.W. Do, Y.H. Kwon, S.W. Cho, Y.D. Yun, J.H. Yoon, H.-B.-R. Lee, S.-W. Kim, H.K. Cho, *Nano Energy* 46 (2018) 1–10.
- [114] T.H. Jeon, G. Moon, H. Park, W. Choi, *Nano Energy* 39 (2017) 211–218.
- [115] Z. Zhang, C. Gao, Z. Wu, W. Han, Y. Wang, W. Fu, X. Li, E. Xie, *Nano Energy* 19 (2016) 318–327.
- [116] S. Kumar, B. Kumar, T. Surendar, V. Shanker, *Mater. Res. Bull.* 49 (2014) 310–318.
- [117] K. Dai, T. Peng, D. Ke, B. Wei, *Nanotechnology* 20 (2009) 125603.
- [118] S. Rai, A. Ikram, S. Sahai, S. Dass, R. Shrivastav, V.R. Satsangi, *Renew. Energy* 83 (2015) 447–454.
- [119] D. Chaudhary, S. Singh, V. Vankar, N. Khare, *Int. J. Hydrogen Energy* 42 (2017) 7826–7835.
- [120] M.H. Elbakkay, W.M. El Roubay, S. El-Dek, A.A. Farghali, *Appl. Surf. Sci.* 439 (2018) 1088–1102.
- [121] T. Mahvelati-Shamsabadi, E.K. Goharshadi, *Sol. Energy* 161 (2018) 226–234.
- [122] K. Li, X. Zeng, S. Gao, L. Ma, Q. Wang, H. Xu, Z. Wang, B. Huang, Y. Dai, J. Lu, *Nano Res.* 9 (2016) 1969–1982.
- [123] A. Seza, F. Soleimani, N. Naseri, M. Soltaninejad, S. Montazeri, S. Sadmezhaad, M. Mohammadi, H.A. Moghadam, M. Forouzandeh, M. Amin, *Appl. Surf. Sci.* 440 (2018) 153–161.
- [124] A. Gomis-Berenguer, V. Celorrio, J. Iniesta, D.J. Fermin, C.O. Ania, *Carbon* 108 (2016) 471–479.
- [125] A. Aqel, K.M.A. El-Nour, R.A. Ammar, A. Al-Warthan, *Arabian J. Chem.* 5 (2012) 1–23.
- [126] Y. Cheng, A. Memar, M. Saunders, J. Pan, C. Liu, J.D. Gale, R. Demichelis, P.K. Shen, S.P. Jiang, *J. Mater. Chem. A* 4 (2016) 2473–2483.
- [127] S. Rai, A. Ikram, S. Sahai, S. Dass, R. Shrivastav, V.R. Satsangi, *Int. J. Hydrogen Energy* 42 (2017) 3994–4006.
- [128] J.B. Veluru, K.K. Manippady, M. Rajendiren, K.M. Mya, P.R. Rayavarapu, S.N. Appukuttan, R. Seeram, *Int. J. Hydrogen Energy* 38 (2013) 4324–4333.
- [129] D. Chaudhary, S. Singh, V. Vankar, N. Khare, *J. Photochem. Photobiol. Chem.* 351 (2018) 154–161.

- [130] P.E.S. Rodriguez, F. Olivares, S. Gómez-Ruiz, G. Cabrera, R. Villalonga, R.S. del Río, *Thin Solid Films* 656 (2018) 30–36.
- [131] Y.J. Kim, G.J. Lee, S. Kim, J.-W. Min, S.Y. Jeong, Y.J. Yoo, S. Lee, Y.M. Song, *ACS Appl. Mater. Interfaces* 10 (2018) 28672–28678.
- [132] S.S. Patil, M.A. Johar, M.A. Hassan, D.R. Patil, S.-W. Ryu, *Sol. Energy* 178 (2019) 125–132.
- [133] S.S. Patil, M.A. Johar, M.A. Hassan, D.R. Patil, S.-W. Ryu, *Appl. Catal. B Environ.* 237 (2018) 791–801.
- [134] A. Verma, A. Srivastav, S. Sharma, P. Badami, V.R. Satsangi, R. Shrivastav, A.M. Kannan, D.K. Avasthi, S. Dass, *Int. J. Hydrogen Energy* 43 (2018) 6049–6059.
- [135] S. Dilger, S. Landsmann, M. Trottmann, S. Pokrant, *J. Mater. Chem. A* 4 (2016) 17087–17095.
- [136] Z. Zhu, L. Garcia-Gancedo, A.J. Flewitt, H. Xie, F. Moussy, W.I. Milne, *Sensors* 12 (2012) 5996–6022.
- [137] G. Xie, K. Zhang, B. Guo, Q. Liu, L. Fang, J.R. Gong, *Adv. Mater.* 25 (2013) 3820–3839.
- [138] K. Li, C. Zhang, X. Li, Y. Du, P. Yang, M. Zhu, *Catal. Today* (2018).
- [139] T. Soltani, A. Tayyebi, B.-K. Lee, *Solar Energy Materials and Solar Cells*, 185, 2018, pp. 325–332.
- [140] A. Kaoutk, T.P. Ruoko, Y. Gönüllü, K. Kaunisto, A. Mettenböcker, E. Gurevich, H. Lemmetyinen, A. Ostendorf, S. Mathur, *RSC Adv.* 5 (2015) 101401–101407.
- [141] N. Alam, A. Ullah, Y. Khan, W.C. Oh, K. Ullah, *J. Mater. Sci. Mater. Electron.* 29 (2018) 17786–17794.
- [142] M. Nasiri, P. Sangpour, S. Yousefzadeh, M. Bagheri, *J. Environ. Chem. Eng.* 7 (2019) 102999.
- [143] Y.W. Phuan, M.N. Chong, J.D. Ocon, E.S. Chan, *Solar Energy Materials and Solar Cells*, 169, 2017, pp. 236–244.
- [144] X. Sun, G. Ma, X. Lv, M. Sui, H. Li, F. Wu, J. Wang, *Materials* 11 (2018) 780.
- [145] S.B.A. Hamid, S.J. Teh, C.W. Lai, S. Perathoner, G. Centi, *J. Energy Chem.* 26 (2017) 302–308.
- [146] M. Ghorbani, H. Abdzadeh, M. Taheri, M.R. Golobostanfard, *Int. J. Hydrogen Energy* 43 (2018) 7754–7763.
- [147] X. Xu, B. Feng, G. Zhou, Z. Bao, J. Hu, *Mater. Des.* 101 (2016) 95–101.
- [148] I. Khan, A.A. Ibrahim, M. Sohail, A. Qurashi, *Ultrason. Sonochem.* 37 (2017) 669–675.
- [149] X. Han, Y. Wei, J. Su, Y. Zhao, *ACS Sustain. Chem. Eng.* 6 (2018) 14695–14703.
- [150] J. Xie, J. Chen, C.M. Li, *Int. J. Hydrogen Energy* 42 (2017) 7158–7165.
- [151] P. Subramanyam, T. Vinodkumar, D. Nepak, M. Deepa, C. Subrahmanyam, *Catal. Today* 325 (2019) 73–80.
- [152] Q. Pan, K. Yang, G. Wang, D. Li, J. Sun, B. Yang, Z. Zou, W. Hu, K. Wen, H. Yang, *Chem. Eng. J.* (2019).
- [153] A. Mukherjee, S. Chakrabarty, N. Kumari, W.-N. Su, S. Basu, *ACS Omega* 3 (2018) 5946–5957.
- [154] H.-S. Jo, M.-W. Kim, B. Joshi, E. Samuel, H. Yoon, M.T. Swihart, S.S. Yoon, *Nanoscale* 10 (2018) 9720–9728.
- [155] H.-S. Lin, L.-Y. Lin, *Electrochim. Acta* 252 (2017) 235–244.
- [156] Y.-T. Song, L.-Y. Lin, Y.-S. Chen, H.-Q. Chen, Z.-D. Ni, C.-C. Tu, S.-S. Yang, *RSC Adv.* 6 (2016) 49130–49137.
- [157] D. Chen, Z. Liu, M. Zhou, P. Wu, J. Wei, *J. Alloys Compd.* 742 (2018) 918–927.
- [158] J. Zhang, Z. Liu, Z. Liu, *ACS Appl. Mater. Interfaces* 8 (2016) 9684–9691.
- [159] X. Wang, K. Maeda, A. Thomas, K. Takanabe, G. Xin, J.M. Carlsson, K. Domen, M. Antonietti, *Nat. Mater.* 8 (2008) 76.
- [160] L. Wang, Y. Tong, J. Feng, J. Hou, J. Li, X. Hou, J. Liang, *Sustain. Mater. Technol.* 19 (2019) e00089.
- [161] F. Opoku, K.K. Govender, C.G.C.E. Sittert, P.P. Govender, *Appl. Surf. Sci.* 427 (2018) 487–498.
- [162] F. Dong, L. Wu, Y. Sun, M. Fu, Z. Wu, S.C. Lee, *J. Mater. Chem.* 21 (2011) 15171–15174.
- [163] G. Dong, Z. Ai, L. Zhang, *RSC Adv.* 4 (2014) 5553–5560.
- [164] D.J. Martin, K. Qiu, S.A. Shevlin, A.D. Handoko, X. Chen, Z. Guo, J. Tang, *Angew. Chem. Int. Ed.* 53 (2014) 9240–9245.
- [165] X. Bai, L. Wang, R. Zong, Y. Zhu, *J. Phys. Chem. C* 117 (2013) 9952–9961.
- [166] J. Bian, Q. Li, C. Huang, J. Li, Y. Guo, M. Zaw, R.-Q. Zhang, *Nano Energy* 15 (2015) 353–361.
- [167] L. Ye, S. Chen, *Appl. Surf. Sci.* 389 (2016) 1076–1083.
- [168] X. Lu, Z. Liu, J. Li, J. Zhang, Z. Guo, *Appl. Catal. B Environ.* 209 (2017) 657–662.
- [169] X. Chen, R. Shi, Q. Chen, Z. Zhang, W. Jiang, Y. Zhu, T. Zhang, *Nano Energy* 59 (2019) 644–650.
- [170] H. Miao, G. Zhang, X. Hu, J. Mu, T. Han, J. Fan, C. Zhu, L. Song, J. Bai, X. Hou, *J. Alloys Compd.* 690 (2017) 669–676.
- [171] S. Mahzoon, S.M. Nowee, M. Haghighi, *Renew. Energy* 127 (2018) 433–443.
- [172] Y. Li, G. Liu, D. Jia, C. Li, L. Wang, J. Zheng, X. Liu, Z. Jiao, *Catal. Lett.* 149 (2019) 19–24.
- [173] P. Arora, A.P. Singh, B.R. Mehta, S. Basu, *Vacuum* 146 (2017) 570–577.
- [174] J. Safaei, H. Ullah, N.A. Mohamed, M.F. Mohamad Noh, M.F. Soh, A.A. Tahir, N. Ahmad Ludin, M.A. Ibrahim, W.N.R. Wan Isahak, M.A. Mat Teridi, *Appl. Catal. B Environ.* 234 (2018) 296–310.
- [175] C.-H. Wang, D.-D. Qin, D.-L. Shan, J. Gu, Y. Yan, J. Chen, Q.-H. Wang, C.-H. He, Y. Li, J.-J. Quan, X.-Q. Lu, *Phys. Chem. Phys.* 19 (2017) 4507–4515.
- [176] L. Ye, D. Wang, S. Chen, *ACS Appl. Mater. Interfaces* 8 (2016) 5280–5289.
- [177] S. Wojtyła, K. Szmít, T. Baran, *J. Inorg. Organomet. Polym. Mater.* 28 (2018) 492–499.
- [178] X. Fan, T. Wang, B. Gao, H. Gong, H. Xue, H. Guo, L. Song, W. Xia, X. Huang, *J. He, Langmuir* 32 (2016) 13322–13332.
- [179] M. Song, Y. Wu, X. Wang, M. Liu, Y. Su, *J. Colloid Interface Sci.* 529 (2018) 375–384.
- [180] Z. Lu, L. Zeng, W. Song, Z. Qin, D. Zeng, C. Xie, *Appl. Catal. B Environ.* 202 (2017) 489–499.
- [181] C. Liu, F. Wang, J. Zhang, K. Wang, Y. Qiu, Q. Liang, Z. Chen, *Nano-Micro Lett.* 10 (2018) 37.
- [182] Z. Huang, X. Zeng, K. Li, S. Gao, Q. Wang, J. Lu, *ACS Appl. Mater. Interfaces* 9 (2017) 41120–41125.
- [183] L. Xiao, T. Liu, M. Zhang, Q. Li, J. Yang, *ACS Sustain. Chem. Eng.* 7 (2019) 2483–2491.
- [184] Silver electrode potentials, www.edaq.com/wiki/Reference_Electrode_Potentials#The_Silver.2FSilver_Chloride_.28AgCl.29_Electrode.
- [185] Standard mercury electrode potentials, <http://www.consultsr.net/resources/ref/refpots.htm#ssce>.
- [186] L. Jing, W.-J. Ong, R. Zhang, E. Pickwell-MacPherson, J.C. Yu, *Catal. Today* 315 (2018) 103–109.
- [187] J. Zhang, H. Ma, Z. Liu, *Appl. Catal. B Environ.* 201 (2017) 84–91.
- [188] F. Zhan, J. Li, W. Li, Y. Liu, R. Xie, Y. Yang, Y. Li, Q. Chen, *Int. J. Hydrogen Energy* 40 (2015) 6512–6520.
- [189] Y. Li, Z. Liu, J. Zhang, Z. Guo, Y. Xin, L. Zhao, *J. Alloys Compd.* 790 (2019) 493–501.
- [190] T.N. Trung, D.-B. Seo, N.D. Quang, D. Kim, E.-T. Kim, *Electrochim. Acta* 260 (2018) 150–156.
- [191] D. Sharma, B.R. Mehta, *J. Alloys Compd.* 749 (2018) 329–335.
- [192] P. Wu, Z. Liu, M. Ruan, Z. Guo, L. Zhao, *Appl. Surf. Sci.* 476 (2019) 716–723.
- [193] H. Li, W. Dong, J. Xi, G. Du, Z. Ji, *J. Mater. Sci.* 53 (2018) 7609–7620.
- [194] S.W. Hwang, J.U. Kim, J.H. Baek, S.S. Kalanur, H.S. Jung, H. Seo, I.S. Cho, *J. Alloys Compd.* 785 (2019) 1245–1252.
- [195] A. Abdalla, I. Khan, M. Sohail, A. Qurashi, *Sol. Energy* 181 (2019) 333–338.
- [196] Y. Li, J. Feng, H. Li, X. Wei, R. Wang, A. Zhou, *Int. J. Hydrogen Energy* 41 (2016) 4096–4105.
- [197] K.-H. Cho, Y.-M. Sung, *Nano Energy* 36 (2017) 176–185.
- [198] A. Šutka, M. Vanags, U. Joost, K. Šmits, J. Ruža, J. Ločs, J. Kleperis, T. Juhna, *J. Environ. Chem. Eng.* 6 (2018) 2606–2615.
- [199] A. Liao, Y. Zhou, L. Xiao, C. Zhang, C. Wu, A.M. Asiri, M. Xiao, Z. Zou, *Nanoscale* 11 (2019) 109–114.
- [200] M.G. Ahmed, I.E. Kretschmer, T.A. Kandiel, A.Y. Ahmed, F.A. Rashwan, D.W. Bahnemann, *ACS Appl. Mater. Interfaces* 7 (2015) 24053–24062.
- [201] B. Davide, C. Giorgio, G. Alberto, M. Chiara, W.M.E.A. K. Kimmo, S. Cinzia, T. Stuart, G. Yakup, R. Tero-Petri, B. Laura, B. Elza, V.T. Gustaaf, L. Helge, M. Sanjay, *Adv. Mater. Interface* 2 (2015) 1500313.
- [202] X. Yang, R. Liu, C. Du, P. Dai, Z. Zheng, D. Wang, *ACS Appl. Mater. Interfaces* 6 (2014) 12005–12011.
- [203] C. Zhang, Q. Wu, X. Ke, J. Wang, X. Jin, S. Xue, *Int. J. Hydrogen Energy* 39 (2014) 14604–14612.
- [204] T.J. Macdonald, D.D. Tune, M.R. Dewi, J.C. Bear, P.D. McNaughton, A.G. Mayes, W.M. Skinner, I.P. Parkin, J.G. Shapter, T. Nann, *J. Mater. Chem. C* 4 (2016) 3379–3384.
- [205] A. Ye, W. Fan, Q. Zhang, W. Deng, Y. Wang, *Catal. Sci. Technol.* 2 (2012) 969–978.
- [206] J. Luo, D. Li, Y. Yang, H. Liu, J. Chen, H. Wang, *J. Alloys Compd.* 661 (2016) 380–388.
- [207] N. Ahmed, A.A. Farghali, W.M.A. El Roubi, N.K. Allam, *Int. J. Hydrogen Energy* 42 (2017) 29131–29139.
- [208] S. Chandrasekaran, J.S. Chung, E.J. Kim, S.H. Hur, *Chem. Eng. J.* 290 (2016) 465–476.
- [209] T.-F. Hou, A. Shanmugasundaram, M.A. Hassan, M.A. Johar, S.-W. Ryu, D.-W. Lee, *Int. J. Hydrogen Energy* (2018).
- [210] H. Bae, H. Rho, J.-W. Min, Y.-T. Lee, S.H. Lee, K. Fujii, H.-J. Lee, J.-S. Ha, *Appl. Surf. Sci.* 422 (2017) 354–358.
- [211] M. Wang, P. Ju, J. Li, Y. Zhao, X. Han, Z. Hao, *ACS Sustain. Chem. Eng.* 5 (2017) 7878–7886.
- [212] Y. Zou, J.-W. Shi, D. Ma, Z. Fan, C. He, L. Cheng, D. Sun, J. Li, Z. Wang, C. Niu, *Catalysis Science & Technology* 8 (2018) 3883–3893.
- [213] J. Li, H. Yuan, Z. Zhu, *Appl. Surf. Sci.* 385 (2016) 34–41.
- [214] R. Huo, X.-L. Yang, J.-Y. Yang, S.-Y. Yang, Y.-H. Xu, *Mater. Res. Bull.* 98 (2018) 225–230.
- [215] S. Zhang, J. Yan, S. Yang, Y. Xu, X. Cai, X. Li, X. Zhang, F. Peng, Y. Fang, *Chin. J. Catal.* 38 (2017) 365–371.

Biography



Dr. Edmund P. Samuel is a Research Professor at Korea University, Seoul, South Korea since 2016. He completed his Masters and Ph.D. in Electronics in 2003 and 2008, respectively from North Maharashtra University, Jalgaon, India. He has also worked as a post-doctoral fellow (2011–2014) at Toyota Technological Institute, Nagoya, Japan. His field of research interest includes laser diodes, optoelectronics, solar cell thin films, solar water splitting, lithium ion batteries, and supercapacitors.



Dr. Bhavana Nandkumar Joshi is now a lecturer at NES Science College, Nanded. She completed her masters in Physics in 2004 and Doctorate in Electronics in 2011. She worked as a Research Professor at the School of Mechanical Engineering, Korea University, Seoul. She was recipient of a Fellowship for Foreign Researchers funded by NRF, South Korea. Her research work includes low dielectric constant thin film synthesis for inter-metal insulation in VLSI, deposition of various semiconducting thin films, and nanofibers for energy generation and storage devices.



Dr. Min-Woo Kim received a B.S. degree from Hanyang University in 2014, and his M.S. and Ph.D. at Korea University in 2016 and 2020, respectively. The main field of his research interest is the fabrication of functional films for energy and environmental applications using electro-spray, electrospinning, and supersonic cold spraying.



Mark T. Swihart is UB Distinguished Professor and Department Chair of Chemical and Biological Engineering, and Empire Innovation Professor in the RENEW Institute at the University at Buffalo (SUNY), Buffalo, New York, USA. He earned a B.S. in Chemical Engineering from Rice University and a Ph.D. in Chemical Engineering from the University of Minnesota. His research focuses on colloidal and aerosol synthesis of nanomaterials for diverse applications.



Sam S. Yoon has been a Professor in the School of Mechanical Engineering at Korea University since 2005. He received a B.S. degree from Colorado School of Mines in 1997, and his M.S. and Ph.D. degrees in Aeronautics and Astronautics from Purdue University in 1999 and 2002, respectively. His fields of expertise are spray coating, aerosol science, and nanotechnology.